ulm university universität
uulm

Fakultät für
Naturwissenschaften
Institut für Elektrochemie

Estimating State of Charge and State of Health of Lithium-Ion Batteries in Low Earth Orbit Satellites

Dissertation zur Erlangung des Doktorgrades Dr. rer. nat. der Fakultät für Naturwissenschaften
der Universität Ulm

Vorgelegt von:
Linda Juliane Bolay
aus Filderstadt, 2024

Dekan:
Prof. Dr. Kay-Eberhard Gottschalk

Gutachter:
Prof. Dr. Arnulf Latz
Prof. Dr.-Ing. Michael Danzer

Betreuer:
Prof. Dr. Birger Horstmann

Tag der Promotion:
05. Februar 2024

Fassung February 13, 2024

Satz: PDF-LaTeX 2_ε

Zusammenfassung

Lithium-Ionen-Batterien werden heutzutage vielfach in diversen alltäglichen Geräten verwendet wie Smartphones, Laptops und elektrischen Fahrzeugen. Aber auch in der Luft- und Raumfahrt spielen sie eine wichtige Rolle. Wegen ihrer hohen spezifischen Energie eignen sie sich besonders gut für den Einsatz in Raumfahrtmissionen, bei denen unter anderem das Gewicht der verbauten Geräte entscheidend ist. Außerdem sind sie sicher und zuverlässig; zwei unbedingt notwendige Faktoren in der Raumfahrt. Die Verwendung in Satelliten, die um die Erde kreisen, bietet sich hier besonders an, da die Batterien so unbegrenzt über Solarzellen von der Sonne geladen werden können.

Die besonders hohen Anforderungen an Sicherheit und Zuverlässigkeit in Raumfahrt-Anwendungen stellt besondere Herausforderungen an den Betrieb der Batterien. Die Dauer der Mission hängt unter anderem von der Lebensdauer der Batterien ab. Deshalb muss ihr Betrieb so gestaltet sein, dass es zu keinen Unfällen kommt, die Lebensdauer möglichst lang ist und die Alterung der Batterien möglichst genau vorhergesagt werden kann.

Um das zu garantieren, ist es notwendig, die Prozesse in Li-Ionen-Batterien zu verstehen. Sowohl während der Lagerung als auch während der Zyklisierung finden verschiedene Prozesse in den Batterien statt, die diese altern lassen. Einer der Hauptmechanismen ist das Wachstum der sogenannten Solid-Electrolyte Interphase (SEI). Dies ist eine passivierende Schicht, die sich auf der Oberfläche der Anoden-Partikel bildet und dadurch kontinuierlich Li-Ionen konsumiert, was zu einem unumkehrbaren Kapazitätsverlust führt. Für die Prozesse in der Batterie während der Zyklisierung und für die Alterung gibt es Modelle, die diese akkurat beschreiben.

Die vorliegende Arbeit untersucht, mit Hilfe dieser Modelle, den Betrieb und die Alterung von Li-Ionen-Batterien in Satelliten-Anwendungen und schätzt die inneren Zustände der Batterien, die nicht gemessen werden können. Hierzu werden Daten des kleinen japanischen Satelliten REIMEI verwendet, die von der Japanischen Raumfahrtbehörde JAXA zur Verfügung gestellt wurden.

Basierend auf terrestrischen Experimenten, die die REIMEI-Mission begleiteten, werden die Modelle parametrisiert, sodass damit die typische Zyklisierung von Satelliten-Batterien simuliert und die Alterung unter diesen speziellen Einsatzbedingungen untersucht werden kann. Die Parametrisierung erfolgt mit direkten Verfahren, bei denen Parameter zum Beispiel in Mikro-CT Aufnahmen gemessen

werden und mit indirekten Verfahren, bei denen Zyklisierungsmessungen mit den Simulationen verglichen und Parameter so bestimmt werden, dass eine möglichst große Übereinstimmung erreicht wird. Die Simulationen werden mit verschiedenen Auflösungen durchgeführt. Dreidimensionale mikrostruktur-aufgelöste Simulationen erlauben dabei einen besonders realistischen Einblick in die Alterungsprozesse in der Batterie.

Die parametrisierten Modelle werden anschließend verwendet, um die Zustände in der Batterie in Betrieb zu schätzen. Innere Zustände, wie der Ladezustand und der Gesundheitszustand der Batterie, können nicht direkt gemessen werden. Deshalb werden Filtermethoden verwendet, um die Batterie-Modelle mit den messbaren Größen wie Strom und Spannung zu kombinieren und damit akkuratere Schätzungen der Zustände zu erhalten. Filter wie das Kalman-Filter bieten sich besonders an für komplexe Systeme, bei denen sowohl die Messgrößen als auch die Modelle fehlerbehaftet sind. Um der unterschiedlichen Zeitentwicklung der Zustände gerecht zu werden, wird ein Algorithmus entwickelt, der zwei Filter koppelt und damit die Zustände simultan schätzt. Der Algorithmus wird weiter dazu verwendet, die Güte der verwendeten Modelle zu bewerten und das Alterungsverhalten zu prognostizieren.

Die hier beschriebenen Methoden sind eine wertvolle Ergänzung, um einen sicheren und zuverlässigen Betrieb von Li-Ionen-Batterien in Raumfahrt-Anwendungen zu gewährleisten und die Vorbereitung zukünftiger Missionen zu unterstützen.

Abstract

Lithium-ion batteries are widely used today in various devices of everyday use, such as smartphones, laptops, and electric vehicles. But they also play an important role in the aerospace industry. Due to their high specific energy, they are particularly suitable for application in space missions where, among other things, the weight of the installed devices is crucial. They are also safe and reliable, two essential factors in aerospace applications. Their use in satellites orbiting the earth is particularly beneficial here, as the batteries can be charged infinitely via solar cells by the sun.

The very high safety and reliability requirements in space applications pose special challenges for battery operation. The duration of the mission depends, among other things, on the service life of the batteries. Their operation must therefore be designed in such a way that no accidents occur, the service life is as long as possible, and the aging of the batteries can be predicted as accurately as possible. To guarantee this, it is necessary to understand the processes in Li-ion batteries. During both storage and cycling, various processes take place in the batteries that cause them to degrade. One of the main mechanisms is the growth of the so-called solid-electrolyte interphase (SEI). This is a passivating layer that forms on the surface of the anode particles and thus continuously consumes Li-ions, leading to an irreversible loss of capacity. There are models that accurately describe the processes in the battery during cycling and aging.

This thesis uses these models to investigate the operation and aging of Li-ion batteries in satellite applications and estimates the internal states of the batteries, which cannot be measured. For this purpose, data from the small Japanese satellite REIMEI provided by the Japan Aerospace Exploration Agency (JAXA) are used.

Based on terrestrial experiments that accompanied the REIMEI mission, the models are parameterized so that the typical cycling of satellite batteries can be simulated and the aging under these special operating conditions can be investigated. The parameterization is carried out using direct methods, in which parameters are measured, for example in micro-CT images, and indirect methods, in which cycling measurements are compared with simulations and the model parameters are determined in such a way that the best possible agreement is achieved. The simulations are carried out with different resolutions. Three-dimensional microstructure-resolved simulations provide a particularly realistic insight into the aging processes

in the battery.
The parameterized models are subsequently used to estimate the states in the battery in operation. Internal states, such as the state of charge and the state of health of the battery, cannot be measured directly. Therefore, filtering methods are used to combine the battery models with the measurable quantities such as current and voltage to obtain more accurate estimates of the states. Filters such as the Kalman filter are particularly suitable for complex systems in which both the measured variables and the models are subject to errors. In order to account for the different time evolution of the states, an algorithm is developed that couples two filters and in this way estimates the states simultaneously. The algorithm is also used to evaluate the accuracy of the models used and to predict the aging behavior.
The methods described here are a valuable addition to ensure safe and reliable operation of Li-ion batteries in space applications and to support the preparation of future missions.

Contents

Abbreviations

CC - Constant current
COTS - Commercial off-the-shelf
CV - Constant voltage
DAE - Differential algebraic equation
DFN - Doyle-Fuller-Newman (model)
DOD - Depth of discharge
ECM - Equivalent circuit model
EKF - Extended Kalman filter
EoC - End of charge
EoD - End of discharge
EoDV - End of discharge voltage
GITT - Galvanostatic intermittent titration technique
LEO - Low earth orbit
MTS - Multi-timescale
OCV - Open circuit voltage
P2D - Pseudo-two-dimensional
SEI - Solid-electrolyte interphase
SOC - State of charge
SOH - State of health

1 Introduction

Lithium-ion (Li-ion) batteries are used in various applications. Among the best-known are electric vehicles, smartphones, laptops, and other portable devices. In space, batteries have generally been used for a long time. However, although the first commercial Li-ion battery was produced in 1991, it took some time before space agencies started using Li-ion batteries for space applications as well. Nowadays, they are popular in all kinds of aerospace applications, among other things because of their light weight.

Satellites orbiting the Earth differ in several categories, such as height above the Earth, size or weight, and the type of mission they perform. Typically, satellites are on a geostationary orbit (GEO) with a fixed position relative to Earth or on a low Earth orbit (LEO), which is the area of space below 2,000 km. In addition, they are distinguished by weight, with small satellites, for example, weighing less than 500 kg. The orbit of the satellite and its weight depend on its mission. These can be scientific, commercial, or military and include tasks such as navigation, communication, and Earth or weather observation [34, 8, 87].

One critical aspect of space missions is their cost. These depend, among other things, on the weight, size and price of the components. One way to reduce the effort and cost of missions is to use commercial off-the-shelf (COTS) components [8, 7].

Requirements of Satellite Batteries

Batteries for space applications must meet special requirements that differ from those for applications on Earth, such as electric vehicles. Already during launch, the batteries have to withstand harsh conditions such as shocks, vibrations, and acceleration [34]. In space, the satellite is exposed to special conditions such as extreme temperatures. Therefore, the batteries must be heated and cooled to keep them at a moderate temperature of about 20°C [98]. In addition, the batteries must operate in a hard vacuum, which places special demands on battery chemistry such as the electrolyte [108]. It might be assumed that radiation in space would also be a challenge for batteries. However, it turns out that radiation does not affect the behavior of the batteries [96]. The REIMEI mission also studied the effect of microgravity and vacuum on battery operation in space [98].

Another important requirement is the cycle life capability. Batteries are usually required to operate reliably for five years [34]. As described below, the usual cycling protocol results in approximately 5,000 charge and discharge cycles per year. This means that the batteries must deliver the required capacity and voltage range specified by the payloads and satellite systems for at least 25,000 cycles.

To meet all of these requirements, the batteries must be tested prior to mission launch. Especially for cycling tests, which usually take a long time, the testing effort can be reduced by virtual support such as models that predict the degradation and end of life of the batteries.

History of Batteries in Satellites

Batteries have long been an important source of energy in aerospace. The first battery used in a satellite was a silver-zinc primary battery. It was used in the Russian spacecraft Sputnik in 1957 for operations and communications. Due to the lack of solar cells, the battery could not be recharged and was exhausted after three weeks [34, 8]. With the use of solar panels in satellites, secondary cells became employed. The first secondary battery was a nickel-cadmium (Ni-Cd) battery. One of the first spacecrafts to use this type of battery was the TIROS I, a weather satellite launched by NASA in 1960. To ensure a long battery life, the depth of discharge was only 3 %. The necessary capacity was achieved by large size and cost of the battery. The next common battery type was nickel-hydrogen (Ni-H2) batteries. These were first used by the U.S. Navy in 1966 in a spacecraft as a backup for a Ni-Cd battery. Later, in 1983, nickel-hydrogen batteries were used in an Intelsat V satellite for a GEO mission [34].

With the endeavor to reduce battery size and increase energy density, Li-ion batteries became attractive for space applications. The first use of a Li-ion battery in a satellite was in 2004, when Eutelsat's telecommunications satellite using SAFT batteries was placed in geostationary orbit [62]. Satellite REIMEI, launched in 2005, is another example of one of the first satellites to be equipped with a Li-ion battery. This type of battery was one of the technologies to be tested during the mission [86].

The advantages of Li-ion batteries compared to Ni-Cd and Ni-H2 batteries are shown in Table 1.1.

Table 1.1: Comparison of different battery types used in satellites as of 2014. Excerpt from the table of Mattesco et al. and Malet et al. [62, 59].

	NiCd	NiH2	Li-ion	System impact
Energy density (Wh/kg)	30	60	153	Dry mass saving
Energy efficiency (%)	72	70	96	Reduction of charge power: solar panel mass and dimension.
Thermal power (scale 1-10)	8	10	1	Reduction of radiators, heat pipes sizes
Self discharge (% per day)	1	10	0.3	Simple management at launch pad and more margin during transfer
Temperature range (°C)	0,40	-20,30	10,30	Management at ambient
Memory effect	yes	yes	no	No reconditioning management
Energy gauge	no	pressure	voltage	Easier state of charge assessment

Cycling Protocols of LEO Satellite Batteries

Most satellites are located in LEO, which is the area of space below 2,000 km. Satellites in LEO have a typical orbital period of about 100 minutes. Fig. 1.1 shows the typical satellite orbit where the satellite is exposed to the sun for about 65 minutes and is in the earth's shadow for 35 minutes. This directly affects the cycling of the batteries. While the satellite is in the sun, the batteries are charged by the solar cells. In the shadow, the satellite loads are powered, which discharges the batteries. The LEO cycling protocol results in about 14 cycles per day and about 5,000 cycles per year [34, 18].

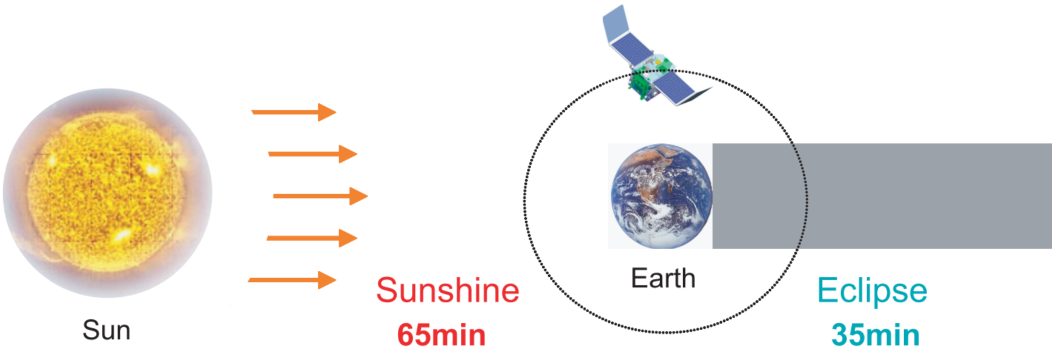

Figure 1.1: Typical orbit of LEO satellite. The batteries of the satellite get charged while it is in the sun and discharged during the eclipse. From PhD thesis of Shelley Brown [18].

The battery data measured in orbit are shown in Fig. 1.2 for several cycles. The data consist of voltage, current, and temperature of the individual batteries. The data shown here as an example are from the satellite REIMEI and were published in Ref. [97] by Sone et al.

Operation of Batteries in Satellites

The structure of a satellite usually consists of the satellite bus, which is the infrastructure of the satellite components, and the payloads. The bus consists of several subsystems that maintain the satellite's operation. This includes the housing that protects the components from space conditions, such as extreme temperatures, and from vibrations to which they are subjected during launch. The power subsystem controls the power supply to the loads from solar panels and the power storage in batteries. Measurement data of the loads are sent to Earth control stations and operation commands are received. Furthermore, there are subsystems that regulate the temperature of the satellite components and its altitude [87, 7].

The energy supply via the power subsystem in the satellite is controlled by several components. These include energy generation, conversion to electrical energy, energy storage, and energy distribution. Solar cells are usually used for power generation, especially for satellites in Earth orbit. For spacecrafts too far from the sun to draw sufficient power from it, nuclear generators are often used [28]. The generated power is either used for the payloads and satellite bus systems or stored in secondary batteries [87, 7].

The batteries usually consist of several cells, which are connected in series or

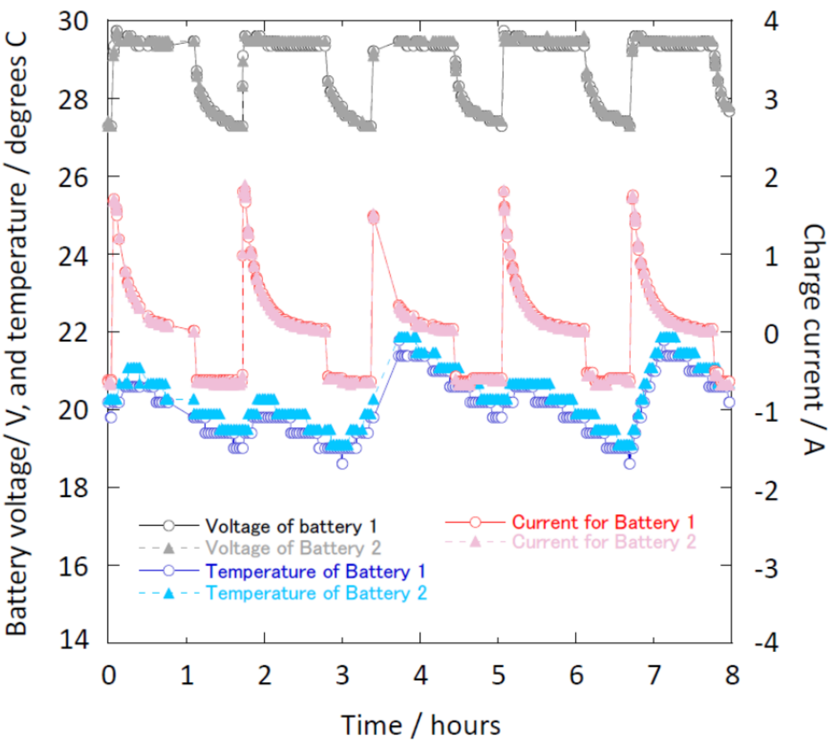

Figure 1.2: Battery data of in-orbit satellite REIMEI. The data consist of voltage, current and temperature of the two Li-ion batteries in the satellite. From Sone et al. [97].

parallel depending on the requirements of the loads. Since Li-ion cells have a specific safe operating window in terms of voltage, current, and temperature, they must be regulated. This is done by the battery management system (BMS). The BMS controls the charging and discharging of the batteries or individual cells depending on the commands it receives from the satellite's power control unit. It monitors the temperature of the battery or cells and keeps them within a safe range by heating and cooling them. Another important function of the BMS is battery balancing, which involves monitoring and distributing the total charge of the cells to prevent overcharging of individual cells [4].

The application of batteries in space imposes special requirements on battery control that differ from terrestrial applications. Maintaining the batteries in a safe operating window ensures a minimum number of cycles before the capacity or end-of-discharge voltage (EoDV) falls below a certain value, which is given by the requirements of the satellite loads. Since the number of cycles on space missions is relatively high and there is no possibility to maintain or replace the cells, they are usually charged to only 4.1 V instead of the typical maximum voltage of 4.2 V. The depth of discharge is also usually kept around 20 %. These precautions extend the cycle life of the cells [105, 19, 4].

Another important factor in battery control is the estimation of state of charge (SOC) and state of health (SOH). These states are necessary to operate the cells optimally and to predict the remaining useful life. Different from typical terrestrial applications, it is not usual that the SOH or even SOC are determined in the BMS of a small satellite. Since weight and size of the components are of great importance in space applications, also the BMS must be small. However, since the use of batteries in satellites is very different from terrestrial applications such as electric vehicles, it is not essential to implement these estimators into the BMS on board the satellite. One of the main differences is the cycling of the cells. For electric vehicles, the cycle is very dynamic with current peaks during high energy demand. In contrast, the cycle of LEO satellite batteries usually follows a specific protocol, with charging every 100 minutes at a constant current. Another major difference is that the satellite is not completely autonomous, but is controlled by the ground station, to which it sends in-orbit data daily. This telemetry data can then be used to determine the states of the satellite and the batteries, which leads to new commands that are in turn sent to the satellite [25, 6, 59].

Japanese Satellite REIMEI

Here, we focus on small satellites on a LEO. Especially, on the small scientific satellite REIMEI, developed by the Japan Aerospace Exploration Agency (JAXA). The satellite was launched in 2005 on the Dnepr rocket as piggy-bag. It uses COTS Li-ion batteries [86, 87, 105]. The mission was accompanied by terrestrial experiments [105]. These investigated the degradation of Li-ion batteries cycled with a typical LEO satellite protocol. Also Brown et al. investigated the degradation behavior of satellite REIMEI's batteries in cycling experiments [19, 18].

This work is based on a collaboration with JAXA, who provided measurement data of the on-board batteries of satellite REIMEI, which span several years of in-flight cycling. These in-flight data are a unique basis to investigate long-term degradation and to develop and validate methods that predict the battery lifetime.

Battery Modeling and State Estimation in Satellites

It is important to understand the processes taking place in the batteries during operation, to be able to operate them safely and to reliably predict their performance during the mission. To this aim, it is helpful to use battery models and state estimation techniques to get a deeper insight, which goes beyond the observation of the measurable quantities.

For common applications like electric vehicles, there are many publications that investigate the simulation and state estimation of Li-ion batteries under terrestrial conditions [35]. However, the methods are not always transferable to space applications. One of the special challenges is, for example, the determination of the battery capacity, since fully discharging the cells to measure the capacity is not possible in space applications. Chapel et al. give an overview of how degradation estimation methods can be used in space applications [22].

Especially, research using physics-based models in combination with Li-ion batteries in space applications is sparse [22]. Some use entirely data-based methods [69, 112]. Song et al. propose an approach, with which it is possible to combine a data-driven method with a model-based one using a filter. With this approach they aim to estimate the SOH of satellite batteries [99]. The SOC and SOH of satellite batteries under LEO cycling conditions are estimated in Refs. [80, 45, 6]. While Rahimian et al. use physics-based models combined with synthetic data, Jun et al. use empirical models in combination with terrestrial experiments. Aung et al. also use empirical models as basis for the estimation method and test it with in-flight data.

To the best of our knowledge, there are no publications that cover SOC and SOH estimation with physics-based models in satellite applications, which are validated with on-orbit field data, especially covering operation of several years.

To fill this gap, we develop methods to simulate long-term cycling of Li-ion batteries in satellites with physics-based models and to estimate the SOC and SOH of the batteries in operation based on the in-flight data of satellite REIMEI.

This work is structured as follows. In chapter 2, we give an overview of the physics-based models, which describe the performance and degradation of Li-ion batteries. These are the thermodynamic consistent transport theory of Latz et al. [49] and the growth model of the solid-electrolyte interphase, which is the main mechanism for capacity fading, of von Kolzenberg et al. [48].

Next, in chapter 3, the batteries and in-flight data of satellite REIMEI are explained. We summarize related terrestrial experiments by Uno et al. and Brown et al. [105, 19, 20]. These experiments will be used for parameterizing the battery model. Furthermore, we elaborate on the processing and information extraction of the in-flight data, so that these can be used to validate the models.

The parameterization of the models is described in chapter 4. Approaches like direct parameter extraction from experimental data are used as well as sophisticated techniques for determining the parameters in order to achieve an optimal agreement between simulation and experiment. The parameterized models are then used to simulate the degradation in a pseudo-2D and 3D framework in order to gain deeper insight into the processes in the battery during aging.

Finally, in chapter 5, the models and satellite data are used to estimate the state of charge and state of health of REIMEI's batteries. For the state estimation, an algorithm is developed that couples two Kalman filters to simultaneously estimate these two states, which evolve on different timescales. The development of the algorithm is performed using synthetic data and validated with the actual in-flight data. Eventually, the algorithm is used to investigate the accuracy of the models.

Chapter 6 concludes this work and gives an outlook on future applications and potential follow-up investigations.

2 Battery Theory and Methods

Physics-based models are an essential tool to describe the processes in Li-ion batteries. On the one hand, these models can be used to gain a deeper understanding of the processes by reproducing the measurable behavior of the batteries with simulations. On the other hand, models are a necessary basis for battery management systems to estimate and predict the states in the battery and thereby be able to control the batteries according to specific requirements.

Since batteries are complex systems, where diverse interdependent processes take place on different spatial and timescales, it is necessary to model these multi-scale problems as simple as possible and still sufficiently accurate.

There are several kinds of models, which cover different aspects of Li-ion batteries. Physics-based models, which describe the full cell, are for example continuum models or equivalent circuit models [27, 32, 17, 73, 41]. In this work, we use continuum models to simulate performance and aging of Li-ion batteries. Therefore, we first introduce the thermodynamic consistent transport theory of Latz et al. [49] and subsequently describe a model of von Kolzenberg et al. for a degradation process of Li-ion batteries [48]. Further, we explain how to use it in a pseudo-two-dimensional (P2D) or three-dimensional (3D) framework.

We already described the models in Ref. [15]. Here, we outline them and give further detail on the computational methods used for the simulations.

Other theoretical principles used in this work, apart from the theory of batteries, can be found at the beginning of the sections in which they are required.

2.1 Electrochemistry of Li-Ion Batteries and Continuum Models

Newman and his coworkers were one of the first to describe a physics-based model for Li-ion batteries on the cell level. It is sometimes also referred to as Doyle-Fuller-Newman (DFN) model [27, 32]. This model and its variants and simplifications have since been used a lot to simulate battery dynamics [44, 14, 102, 29, 31, 81].

The thermodynamic consistent transport theory for Li-ion batteries of Latz et al. models transport and reactions of Li-ions in electrolyte and electrode particles on the microstructural scale of batteries. A set of differential algebraic equations (DAEs) describe how the inner states are distributed in the cell and how they evolve over time. The equations are derived in such a way that they are thermodynamic consistent and that the entropy production is positive. The states are the Li-ion concentration in electrolyte c_e, the electrochemical potential of electrolyte φ_e, the Li-ion concentration in solid c_s, and the electrical potential Φ_s [49].

We assume isothermal conditions throughout the cell, which simplifies the equations. These are stated in the following.

Transport in Electrolyte

The transport of Li-ions in the electrolyte is described by the continuity equation

$$\frac{\partial c_\mathrm{e}}{\partial t} = \nabla \cdot (D_\mathrm{e} \nabla c_\mathrm{e}) \; - \; \nabla \cdot \left(\frac{t_+}{z_+ F} \cdot j \right) \tag{2.1}$$

with the electrical current

$$j = -\kappa \nabla \phi - \kappa \frac{1 - t_+}{z_+ F} \left(\frac{\partial \mu}{\partial c} \right) \nabla c \tag{2.2}$$

and the equation for charge conservation

$$0 = \nabla \cdot (\kappa \nabla \varphi_\mathrm{e}) \; - \; \nabla \cdot \left(\kappa \, \frac{1 - t_+}{z_+ F} \left(\frac{\partial \mu}{\partial c} \right) \nabla c_\mathrm{e} \right) \tag{2.3}$$

with the Faraday constant F, the temperature T, the ionic conductivity κ, the diffusion coefficient in electrolyte D_e, the transference number t_+, the number of elementary charges per ion z_+, the chemical potential of Li ions μ, and the concentration of Li-ions c.

Transport in Electrodes

The transport equations in the electrodes are

$$\frac{\partial c_\mathrm{s}}{\partial t} = \nabla \cdot (D_\mathrm{s} \nabla c_\mathrm{s}) \tag{2.4}$$

with the diffusion constant in solid D_s and

$$0 = \nabla \cdot (\sigma \nabla \Phi_\mathrm{s}) \tag{2.5}$$

with the electronic conductivity σ.

Interface Reaction Kinetics

The interface conditions for ionic flux and electric current determine how the transport in electrolyte and electrode particles is coupled. The current density j^{Li^+} across the interface of electrode and electrolyte is given by a Butler-Volmer equation:

$$j^{\mathrm{Li}^+} = F \cdot i_0 \left(\exp\left[\frac{\alpha F}{RT}\eta_\mathrm{s}\right] - \exp\left[-\frac{(1-\alpha)F}{RT}\eta_\mathrm{s}\right]\right) \tag{2.6}$$

with the universal gas constant R and the overpotential

$$\eta_\mathrm{s} = \Phi_\mathrm{s} - \varphi_\mathrm{e} - U_0, \tag{2.7}$$

where U_0 is the open circuit voltage (OCV) of the respective electrode. The reaction rate is

$$i_0 = k \cdot c_\mathrm{e}^\alpha c_\mathrm{s}^\alpha (c_{\mathrm{s,max}} - c_\mathrm{s})^{1-\alpha}, \tag{2.8}$$

with the Butler-Volmer rate constant k, the maximum Li concentration inside the electrode $c_{\mathrm{s,max}}$, and the charge transfer coefficient $\alpha \in [0,1]$. Here, we assume $\alpha = 0.5$.

The main difference between the model of Latz et al. and the DFN model is that Latz et al. use the electrochemical potential instead of electrical potential for electrolyte to guarantee positive entropy and to not violate the Onsager relations.

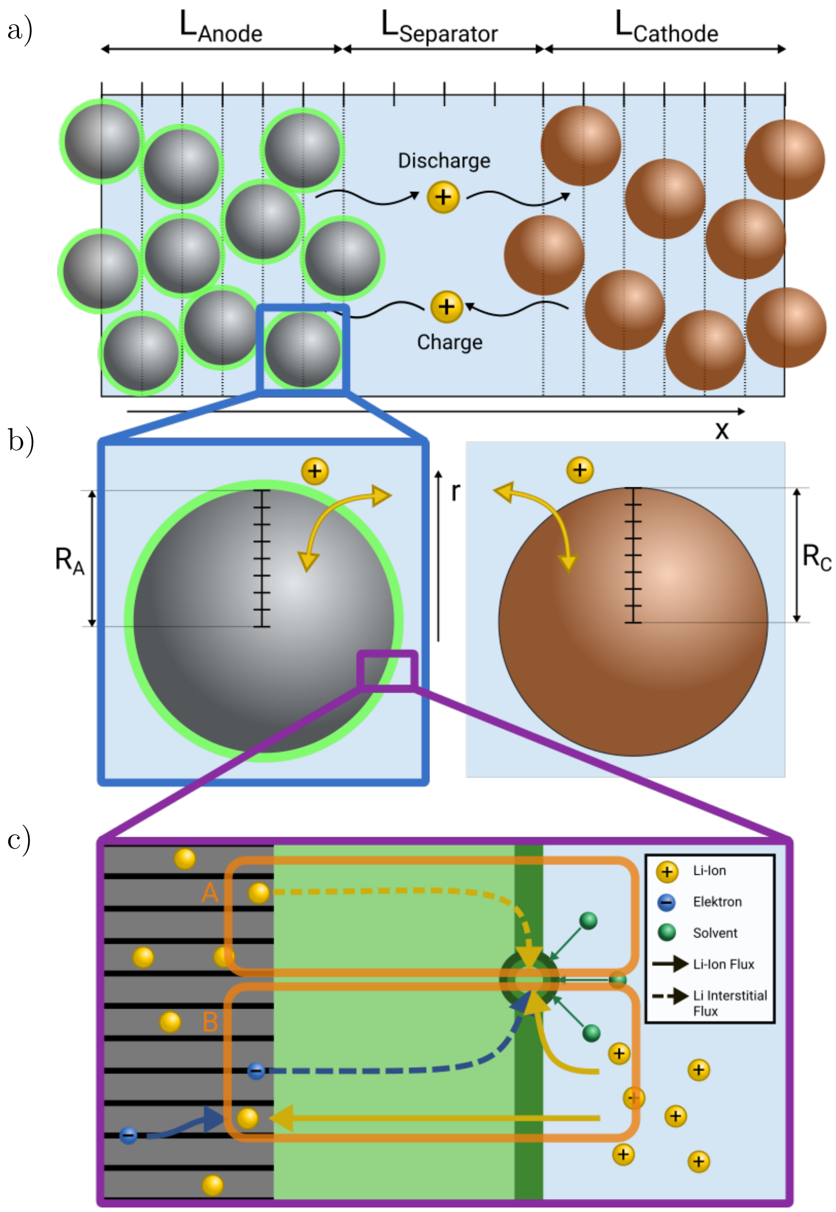

Figure 2.1: Lithium transport on different scales. a) Li-ion transport in electrolyte between electrode particles. b) Li-ion current at electrode interface. c) SEI growth during calendar aging (A) and during cycling (A + B). From Bolay et al. [15].

2.2 Solid-Electrolyte Interphase

In order to understand and simulate the processes taking place in the cell, a physics-based model for the short-term cycling as well as the long-term degradation behavior of the cells is necessary. The long-term degradation of the cell is mainly determined by capacity fading, which is caused by the loss of Li-ion inventory.

The major degradation process taking place in Li-ion batteries is the growth of the solid-electrolyte interphase (SEI). This passivation layer builds on the anode surface during the first cycles of the cell, when solvent molecules from the electrolyte react with Li-ions and electrons. This process prevents the electrolyte from further reaction but does not passivate the reaction completely. The SEI is growing continuously during storage as well as during cycling. Thereby, Li-ions are consumed irreversibly, which causes capacity loss of the cell.

The growth of the SEI is discussed extensively in literature, both in experiment and in theory. Usually, either short-term growth, which considers growth behavior during the first cycle, or long-term growth, which considers continuous growth over months and years, is investigated. In this work, only long-term degradation is discussed.

In experiments, a square-root-of-time ($\sqrt{t}$) behavior is observed for long-term growth [19, 105]. Furthermore, experiments show that SEI growth is accelerated during cycling compared to storage [19]. Attia et al. show that the SEI is especially growing faster during charging of the cell [5]. Another aspect is the inhomogeneous growth of the SEI, which is investigated on nanoscale [16, 42, 79] and on cell level [70].

Short-term SEI growth, i.e. the initial build-up of the SEI during the first cycles, is addressed by atomistic theories like density functional theory and molecular dynamic simulations [107, 10]. The long-term growth behavior of the SEI can be described with empirical models [88, 90]. However, a better understanding of the internal processes is given by physics-based models. For these, several transport mechanisms are considered as the rate-limiting process. The most important are electron conduction [85, 26], electron tunneling [58, 51], reaction kinetics [39, 24], radical diffusion [94, 100], and solvent diffusion [71, 77, 30, 84]. Single et al. compared all of these transport processes to storage experiments and showed that the most probable mechanism for SEI growth during storage is radical diffusion [94]. Das et al. model the asymmetric growth behavior which was shown in Ref. [5] by coupling SEI growth to the Li-ion concentration in the SEI [26]. Von Kolzenberg et al. extended the model of radical diffusion in Ref. [94] by an electron migration effect during cycling, which also reproduces the asymmetric growth. They describe the transitions between transport- and reaction-limited growth and with that give a consistent explanation for the short-term and long-term growth behavior [48]. A comprehensive review of SEI models is given by Horstmann et al. in Ref. [40].

Here, we summarize the SEI model of von Kolzenberg et al. [48] and couple it to the thermodynamic consistent transport theory for Li-ion batteries of Latz et al. [49].

The relation between irreversible capacity loss $Q_{\mathrm{SEI,irr}}$, SEI thickness L_{SEI}, and the growth causing flux N_{SEI} is given as

$$\partial_t Q_{\mathrm{SEI,irr}} = \frac{AFs_{\mathrm{SEI}}}{V_{\mathrm{SEI}}} \cdot \partial_t L_{\mathrm{SEI}} = AF \cdot N_{\mathrm{SEI}}, \tag{2.9}$$

where $N_{\mathrm{SEI}} \geq 0$, A is the surface area of the anode, s_{SEI} is the mean stoichiometric coefficient of Li in the SEI formation reaction, V_{SEI} is the mean partial molar volume of the SEI, and F is the Faraday constant.

Single et al. provided evidence that electron diffusion through the SEI is causing calendaric aging [94]. These electrons diffuse through localized state, e.g., neutral Li-interstitials diffusion [91]. The corresponding flux is deduced from Fick's law and is given as

$$N_{\mathrm{SEI,diff}} = D^{e^-} \cdot \frac{c^{e^-}}{L_{\mathrm{SEI}}}, \tag{2.10}$$

where D^{e^-} is the diffusion coefficient and c^{e^-} is the interstitial concentration at the anode-SEI interface, which is dependent on the electrochemical potential of the anode relative to Li. This process is depicted as process A in Fig. 2.1 c).

The capacity loss increases when the cell is cycled. Attia et al. show that the SEI grows almost exclusively during lithiation of the anode [5]. This phenomenon is also modeled by an electron flux, which is influenced by the Li-ion current through the SEI. This can be seen in Fig. 2.1 c) process B. To take the influence of the Li-ion current into account, an electron migration flux is incorporated and the SEI flux is derived from the Nernst-Planck equation

$$N_{\mathrm{SEI}} = D^{e^-} \cdot \frac{c^{e^-}}{L_{\mathrm{SEI}}} - zF\kappa_{\mathrm{SEI}}^{\mathrm{e}^-} \nabla\Phi, \tag{2.11}$$

with the valence $z = -1$, the conductivity of the localized electrons $\kappa_{\mathrm{SEI}}^{\mathrm{e}^-}$, and the potential gradient $\nabla\Phi$ in the SEI caused by the Li-ion flux. According to [94], the electron concentration in the SEI is approximated by

$$c^{e^-} = c_0^{e^-} \cdot \exp\left(-\frac{F}{RT}\eta_{\mathrm{SEI}}\right), \tag{2.12}$$

with the electron concentration $c_0^{e^-}$ at 0 V anode potential, the universal gas constant R, and the temperature T. Furthermore, the potential gradient is approximated by

$$\nabla\Phi = \frac{-U_{\mathrm{SEI}}}{L_{\mathrm{SEI}}}, \tag{2.13}$$

where the potential drop is defined as

$$U_{\mathrm{SEI}} = \frac{L_{\mathrm{SEI}}}{\kappa_{\mathrm{SEI}}^{\mathrm{Li}^+}} \cdot j^{\mathrm{Li}^+}, \tag{2.14}$$

with the conductivity $\kappa_{\mathrm{SEI}}^{\mathrm{Li}^+}$ of Li-ions in the SEI.

With the help of the Nernst-Einstein equation, the conductivity $\kappa_{\mathrm{SEI}}^{\mathrm{e}^-}$ is approximated by the diffusion coefficient

$$D^{e^-} = RT\kappa_{\mathrm{SEI}}^{\mathrm{e}^-}/c^{e^-} \approx 2RT\kappa_{\mathrm{SEI}}^{\mathrm{e}^-}/c_0^{e^-} \tag{2.15}$$

and eq. (2.11) is rearranged to

$$N_{\mathrm{SEI}} = \frac{D^{e^-} \cdot c_0^{e^-}}{L_{\mathrm{SEI}}} \cdot \exp\left(-\frac{F}{RT}\eta_{\mathrm{SEI}}\right) \cdot \left(1 - \frac{F}{2RT}U_{\mathrm{SEI}}\right). \tag{2.16}$$

The overpotential for the reaction is given as

$$\eta_{\mathrm{SEI}} = \Phi_{\mathrm{s}} - \varphi_{\mathrm{e}} - U_{\mathrm{SEI}}, \tag{2.17}$$

where Φ_{s} is the anode potential and φ_{e} is the electrochemical potential of the electrolyte.

The growth of the SEI not only affects the cell capacity but also its inner resistance. This is taken into account in the Butler-Volmer rate for the intercalation into graphite, where the overpotential from eq. (2.7) is supplemented by the potential drop in the SEI and becomes

$$\tilde{\eta}_{\mathrm{s}} = \eta_{\mathrm{s}} - U_{\mathrm{SEI}}. \tag{2.18}$$

With this, the SEI formation can be included as side reaction in the model of Latz et al. as mentioned in Ref. [49].

2.3 Computational Methods

To solve the set of equations of the continuum models for Li-ion batteries different software tools can be used depending on the resolution of the simulation. These use mathematical methods to solve the DAE system numerically and determine the states of the discretized cell domain at discrete time points.

2.3.1 Microstructure-resolved (3D) Model

For the microstructure-resolved simulations, first, the morphology of the electrodes needs to be reconstructed from tomographic image data or simulated with given morphology characteristics. For example, this is done with stochastic geometry methods by Hein et al. [37]. In our research group, this 3D representation of the Li-ion cell is then used with the software BEST and its successor BESTER to perform spatially resolved electrochemical simulations [43, 50]. The set of equations in Ref. [49] is implemented in this software. The simulations can be used to study and analyze the heterogeneous surface effects as in Ref. [38] by Hein et al.

The microstructure-resolved simulations use a voxel representation of the electrodes. The DAE system is then solved with the finite volume method which is particularly suitable to conserve physical quantities. This conservative discretization method is used in BEST and is described in Refs. [36, 89].

2.3.2 Pseudo-2D Model

The DFN model by Doyle, Fuller and Newman mentioned above is also often called the P2D model since it describes the transport in the electrolyte in one dimension that spans the whole cell between two current collectors via electrodes and separator. The second dimension represents the transport in the particles from center to the surface.

The P2D model is illustrated in Fig. 2.1 a) and b). In Fig. 2.1 a), the volume-averaged transport of Li-ions in the electrolyte between electrodes is shown, which represents the first dimension. The interfacial reaction kinetics between electrolyte and electrode and the transport inside the particles is depicted in Fig. 2.1 b).

Using volume averaging techniques the transport theory by Latz et al. can be transformed into the P2D model. This way, the porous structure of the different layers in the Li-ion cell is not resolved on a microstructural level but represented by a porosity parameter of the material.

The chemical potential can be described with $\mu = 2RT \ln \frac{c}{c_0}$ [65] and we get

$$\frac{\partial \mu}{\partial c} = 2RT \cdot \frac{1}{c}. \tag{2.19}$$

With this, the continuity equation for Li-ion transport in the electrolyte can be transformed to

$$\frac{\partial \varepsilon c_\mathrm{e}}{\partial t} = \nabla \cdot \left(\kappa^\mathrm{eff} \frac{t_+}{F} \nabla \varphi_\mathrm{e} \right) + \nabla \cdot \left(\left(D_\mathrm{e}^\mathrm{eff} - 2\kappa^\mathrm{eff} t_+ (1 - t_+) \frac{RT}{F^2} \frac{1}{c_\mathrm{e}} \right) \nabla c_\mathrm{e} \right) \tag{2.20}$$

with the effective parameters $\kappa^\mathrm{eff} = \frac{\varepsilon}{\tau}\kappa$ and $D_\mathrm{e}^\mathrm{eff} = \frac{\varepsilon}{\tau} D_\mathrm{e}$, the porosity ε, and the tortuosity τ. The equation for charge conservation is transformed to

$$0 = \nabla \cdot \left(\kappa^\mathrm{eff} \nabla \varphi_\mathrm{e} \right) - \nabla \cdot \left(2\kappa^\mathrm{eff} (1 - t_+) \frac{RT}{F} \frac{1}{c_\mathrm{e}} \nabla c_\mathrm{e} \right). \tag{2.21}$$

The equations for transport inside the particles and also those for the interface reaction do not change since they are not affected by the volume averaging.

To simulate the P2D model, the cell level as well as the particle are discretized and the system of nonlinear equations is transformed using the finite difference method. On these discretized domains the DAE system is then solved with a numerical method. The software MATLAB is suitable for this, since there are several algorithms implemented for solving systems of equations efficiently. One of them is the solver `ode15s`, which is applicable to stiff DAEs. With the solver, the variables are determined at discrete time steps. These time steps are adapted by the solver. By interpolating the discrete solutions, a continuous solution is obtained for the simulated time period [61].

The major advantage of simulating the model of Latz et al. in a P2D framework instead of 3D is that the computation is much faster.

3 Satellite Batteries and Battery Data

An important application field of Li-ion batteries is aerospace devices like satellites. At the same time, these applications provide a unique data source to study the long-term degradation behavior of the cells under constant conditions. Battery data from terrestrial experiments and in-flight operations are a valuable basis for the development, calibration, and validation of electrochemical models, which describe the behavior and aging of Li-ion batteries.

This work is based on a collaboration with the Japan Aerospace Exploration Agency (JAXA), which provided battery data of their satellite REIMEI. In this section, we describe the satellite and its batteries, outline the terrestrial experiments that accompanied the satellite mission, and elaborate on the data which are acquired from the on-board batteries.

We already described the satellite, its batteries, and the corresponding experiments in Ref. [15]. Here, we will give more detail and especially explain the processing of the in-flight data.

3.1 Satellite REIMEI

REIMEI is a small scientific satellite developed by JAXA. It was launched at 06:10 on August 24, 2005 (JST) on the Dnepr Rocket from Kazakhstan. It orbits the Earth on a quasi-circular polar low Earth orbit (LEO) with an altitude of 610 - 654 km. It has a size of 60 cm x 60 cm x 70 cm and a mass of 60 kg. Before its launch, it had the code name INDEX. To ensure operability in space it was tested against vacuum, vibration, and radiation prior to the launch. The main control station of REIMEI is in Sagamihara, Japan [96, 97, 87].

The main scientific mission of REIMEI was to observe the aurora and demonstrate advanced satellite technology, one of which is Li-ion batteries that use commercial off-the-shelf pouch cells. In 2013, the aurora observation was terminated. The satellite operation was extended with the main focus shifted to the investigation of performance and aging of the on-board Li-ion batteries [98, 63, 105, 19].

3.2 Satellite Batteries

Satellite REIMEI, which flies on a polar LEO, has an orbital period of 96 minutes. During the sunlight period, the batteries get charged via the solar panels, while they discharge during the eclipse period to power the loads [105]. This results in 15 cycles a day. To ensure a reliable operability of 3 - 5 years, the temperature of the batteries is maintained at $19-22°C$ [87, 98] and the depth of discharge around 20 % [105].

Two identical batteries are connected in parallel on board of the satellite REIMEI, each consisting of seven pouch cells connected in series. The lithium-ion cells are produced by NEC-Tokin Corporation. The positive active material is spinel lithium manganese oxide (LMO) and the negative electrode consists of graphite. The liquid electrolyte is 1 M $LiPF_6$ in EC/DEC (3:7 by wt%) with additives [98, 105]. The cells have a voltage range of 3.0 V - 4.1 V (4.2 V). Their nominal capacity is 3 Ah [19].

The in-flight operation of the cells depends on the loads in use. Given by the on-board devices, the cells reach their end of life when the end-of-discharge voltage (EoDV) falls below 3.75 V [105].

While the satellite is in the sun, the batteries get charged via the solar panels for around 63 minutes. While in the shadow of the earth, they get discharged to power the loads for around 33 minutes by a depth of discharge (DOD) of about 15 %. The discharging takes place with constant currents (CC) depending on the loads in use. The constant current values range between 0.4 A and 1.7 A. The charging profile of the cell is constant current / constant voltage (CC/CV), where a charge current of 1.5 A is applied until 4.1 V is reached. For a few cycles in between and at a later stage of the battery life, the upper cut-off voltage is changed to 4.2 V to prolong the battery life. The temperature of the cells in space is kept around 20 °C [105]. The specifications of the satellite batteries and cells are listed in Tables A.2 and A.1. The cycling protocol can be found in Table 3.1.

Table 3.1: Charge and discharge protocols for terrestrial and in-flight cycling, cf. [19, 105].

	Terrestrial	North Pole	South Pole
Charge (CC/CV)	1.5 A / 4.1 V, 65 min	1.5 A / 4.1 V, 63 min	
Discharge (CC)	1.0 A, 35 min	0.88 A, 15 min 0.74 A, 18 min	0.78 A, 25 min 0.96 A, 5 min 1.6 A, 3 min
DOD	20 %	14 %	16 %
Temperature	25 °C	20 °C	

3.2.1 Terrestrial Electrochemical Measurements

Accompanying the REIMEI mission, Uno et al. and Brown et al. performed terrestrial experiments with the same kind of cells as those of the satellite [105, 19]. They performed cycling experiments with a cycling protocol similar to the one used in the satellite. Table 3.1 compares the cycling protocols.

We use the experimental data to calibrate and validate our simulations. We describe the experiments in the following.

Experiments of Uno et al. in 2011

Uno et al. conducted cycling experiments over a period of about five years [105]. They charged and discharged several cells about 27,000 times. To track the degradation of the cells, they measured the remaining capacity and the EoDV of the cells recurrently.

In the experiments, the cells get discharged with a constant current (CC) of 1 A for 35 minutes, which corresponds to approximately 20 % DOD. Then they get charged for 65 minutes with a constant current / constant voltage (CC/CV) profile. The charging is performed at 1.5 A to the upper voltage limit of 4.1 V. After each discharge, the EoDV is measured. As the cells are degrading, the EoDV falls below 3.75 V after several thousand cycles. At that point, the upper voltage limit for the charging gets changed to 4.2 V to prolong the remaining useful life of the cells. Before and during the cycling, they measure the remaining capacity of the cells several times by discharging it with a CC of 1 A to 3.0 V. We use these electrochemical measurements of Uno et al. in sec. 4.3 to parameterize the P2D model. For the model, we assume constant temperature and constant pressure throughout the cell. This assumption is based on the experiments of Uno et al. and on the in-flight data. In sec. 4.4, the measurements are used to parameterize the degradation.

In Fig. 3.1, the results of the cycling experiments can be seen. In a), we see the voltage curves of the capacity measurements of one of the cells after different numbers of cycles. b) and d) show the capacity and EoDV of all cells for the whole period of the experiments. A zoom-in of the EoDV for the first 250 cycles is shown in c).

The EoDV is compared for the terrestrial and in-flight experiments in Fig. 3.4. It can be seen, that the decrease of the EoDV is faster for the terrestrial experiments which have a higher DOD.

Experiments of Brown et al. in 2008

In 2008, Brown et al. conducted comprehensive terrestrial experiments at JAXA [19, 20]. They investigated the degradation of cycled and calendaric aged cells under various conditions. For the cycling, they use the same cycling protocol as Uno et al. and vary the temperatures and discharge currents respectively the DOD. They examined full and half cells before, during, and after the aging process.

For both electrodes, they measured full charge and discharge at a low current of C/10 respectively 2.08 A m^{-2}. This can be used to determine the OCVs of the electrodes as the mean of the charge and discharge curve. The results can be seen in Fig. 3.2. The OCV curves are determined and used in sec. 4.3 for the P2D model. Furthermore, our cycling protocols in sec. 4.4.2 are based on those of Brown et al.

3.2.2 CT Data

One of the pouch cells of the kind used in the satellite was stored by JAXA. Several years after the start of the mission, CT images of the cell, which was stored at room temperature, were taken in different resolutions. Examples of the CT images can be seen in Fig. 3.3. From the CT images, we extract several parameters of the cell structure, like the thickness of the cell layers or the area of the full cell,

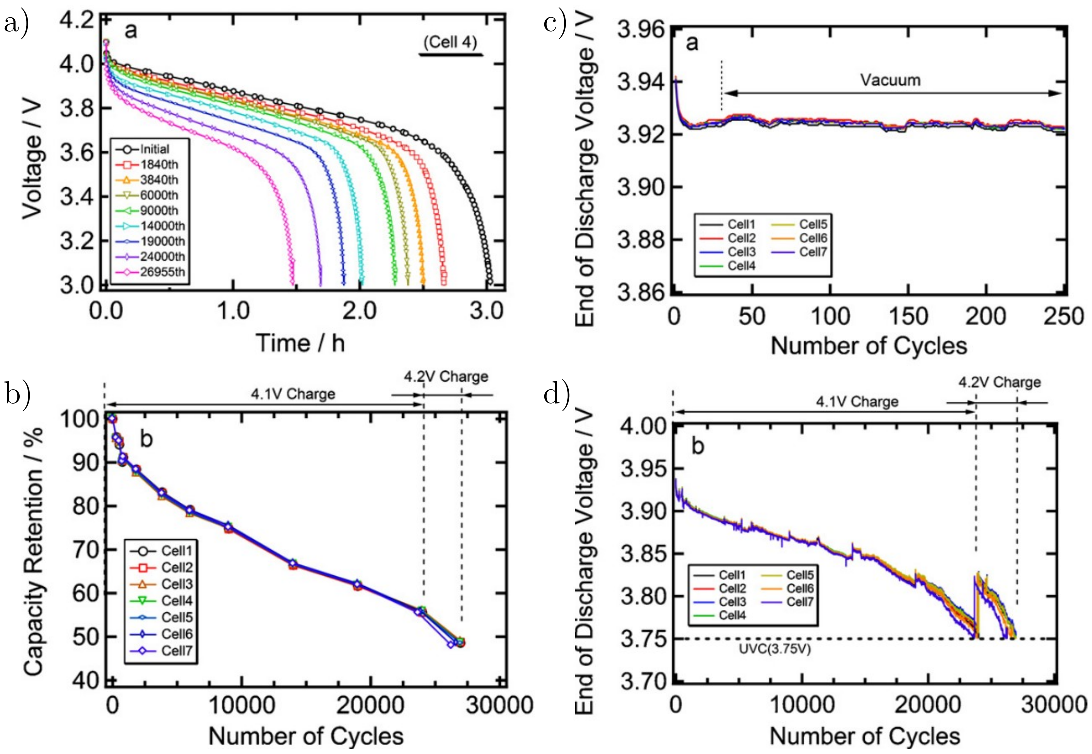

Figure 3.1: Aging experiments with cells of satellite REIMEI. a) Capacity measurements of one cell at several points of time. b) Trend of remaining capacity over about 27,000 cycles of 7 cells. c) Zoom-in of EoDV during initial 250 cycles. d) EoDV of 7 cells during whole period of about 27,000 cycles. From Uno et al. [105].

in sec. 4.3.1. These values are necessary to parameterize the model described in sec. 2.1. The area of the full cell is especially required to relate half cell and full cell experiments of Brown et al. [19, 20].

3.3 In-flight Battery Data

JAXA acquires in-flight data from the satellite batteries throughout the operation of the satellite. As the batteries are no longer available after the launch, they have to be measured on board the satellite and the data is retrieved from the ground station on a daily basis. The data are provided by JAXA to enable us to investigate the degradation of Li-ion cells in a satellite application.

The data consist of a time indicator for the measurements, the current of each of

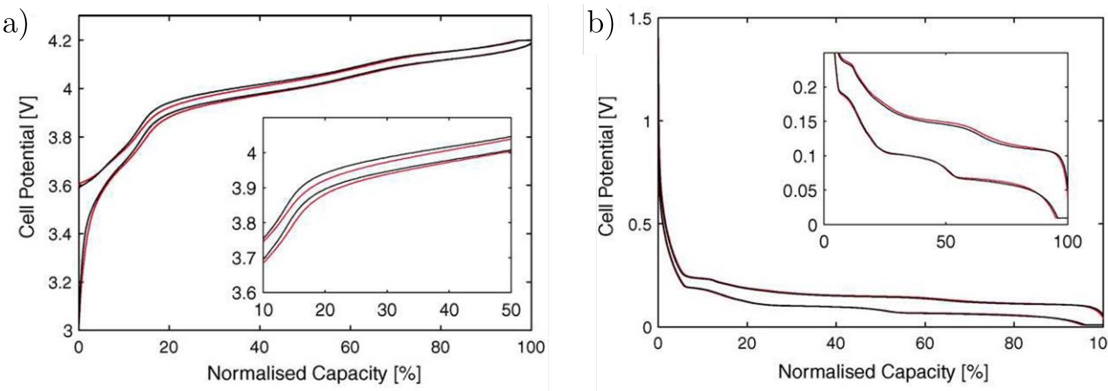

Figure 3.2: Charge and discharge curves of half cells at low current (C/10) for fresh (black) and aged (red) cell. a) Positive electrode cycled between 3 V and 4.2 V. b) Negative electrode cycled between 0.01 V and 1.5 V. From Brown et al. [20].

the two on-board batteries, the battery voltage, and the battery temperature. To obtain the voltage of the cells, the battery voltage is divided by seven. The charge current has a negative sign and the discharge current is positive. We adhere to these signs in our simulation.

The batteries are measured on average every 32 seconds. Some of the measurements are distributed equidistantly, but for the majority of the data, there are repeated groups of four measurements with a distance of 104 seconds, whereby the measurements within the groups are 8 seconds apart.

The on-board operation of the cells depends on the loads in use. So, the discharge current is not only determined by the NP or SP protocol but also depends on the energy needed for the control of the attitude and heater, the acquisition of data, and its transmission to the ground station [98].

In Fig. 3.4, the EoDV of one of the batteries is depicted for a time span of about five years. Additionally, the EoDV of the corresponding terrestrial experiments is shown together with a correction according to the difference between terrestrial and in-flight cycling protocols. Also, the NP and SP phases are marked. It can clearly be seen, how the EoDV depends on the specific cycling protocol. Since the DOD is greater in the terrestrial experiments than in the in-flight cycling, the EoDV reaches the lower limit earlier.

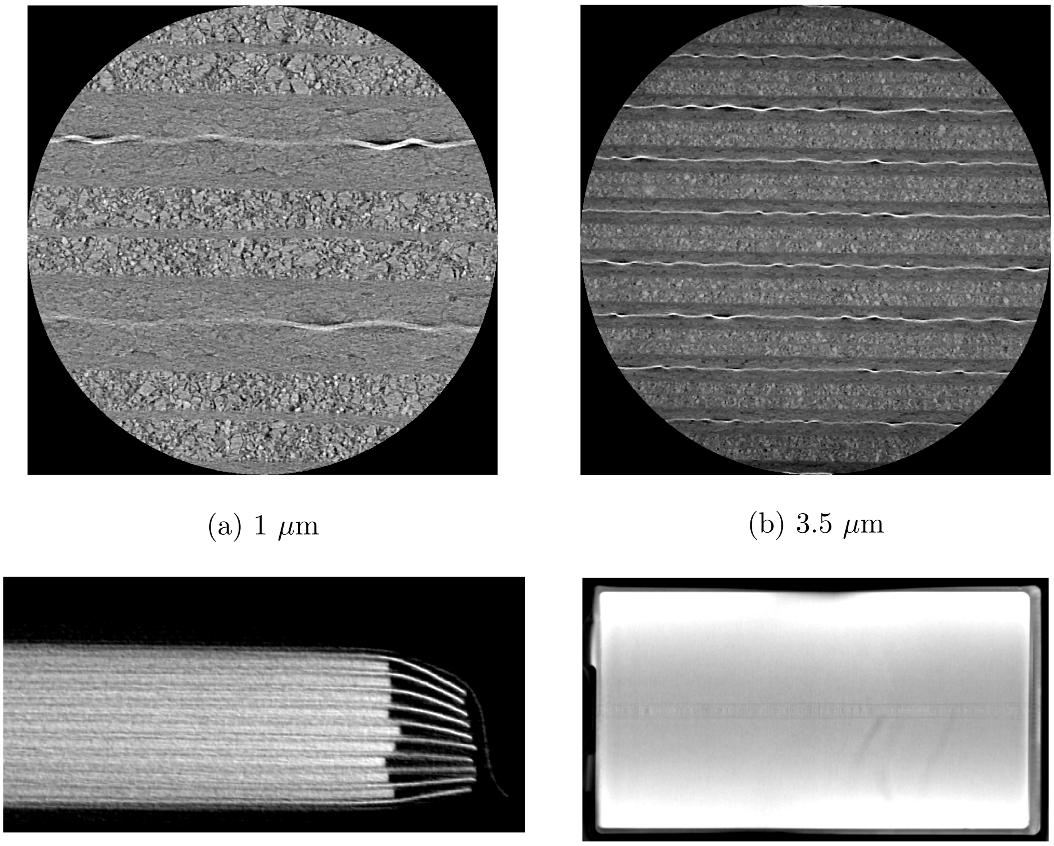

(a) 1 μm

(b) 3.5 μm

(c) 24 μm

(d) 140 μm

Figure 3.3: Micro CT images of satellite REIMEI Li-ion cell with different resolutions. From Bolay et al. [15].

3.3.1 Irregularities in Data

The raw data are acquired over a very long time span and not under laboratory conditions. This leads to several irregularities in the data. The most important, which hamper the use of the data for the simulations, are described here.

Cycle Blocks and Gaps in Data. One challenge is the discontinuity of the data. There are small gaps, where only a few data points are missing, and larger gaps that cover several hours or cycles. Typically, the data appear in blocks of 8 to 23 cycles with gaps in between that also range from about 8 to 23 cycles. For these gaps, we have no information about the batteries.

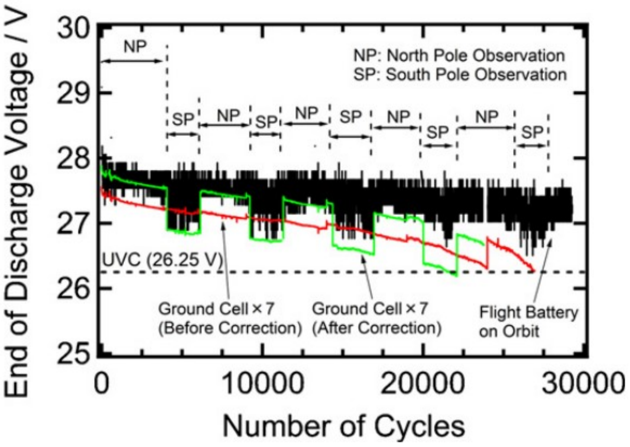

Figure 3.4: EoDV of REIMEI battery in-flight data with highlighted North Pole and South Pole observation periods and actual (red) and corrected (green) terrestrial data. From Uno et al. [105].

Phases in Data. During several years of on-board battery cycling, there are different phases that can be observed in the in-flight data. At the beginning of the measurements in space in 2005, the temperature of the batteries is lower than stated in literature. Also, the cycling is messy at the beginning. Therefore, we dismiss this first part of about ten days and only consider the measurements at normal temperatures for our subsequent work.

Beginning of 2011, the cycling protocol changes in such a way that the CC values are smaller on average during discharge. The cycling behavior from before 2011 is restored in 2012. From mid 2012 to mid 2015 the CV during charge takes on a higher value around 4.2 V.

In early to mid 2013, the data recording ends and remains interrupted for some time. In 2014, there are very sporadic records spread throughout the year. Only in 2015, the records are more complete again, whereby the density of the recorded cycles is significantly lower than in first years and the cycle blocks consist on average of only one to two cycles. This might be due to the severe earthquake and tsunami in 2011 in Japan, which had a massive impact on the whole country. Also, the main part of the mission to observe the aurora ended in 2013 and the main focus of the mission was shifted to the on-board Li-ion cells [97].

In later years, the discharge duration decreases continuously. This is due to the fact that the orbit of the satellite changes and it is in the shadow of the Earth for a shorter and shorter time. This can already be seen in the data in 2015. At the end of 2017, the cycling of the batteries ends completely when the satellite is continuously in the sun.

Solar Eclipse. While the satellite orbits the earth it can occur that it passes the shadow of a solar eclipse. This will stop the charging of the batteries and for a short time they get discharged. An example can be seen in Fig. 3.5 for the solar eclipse on 29 March 2006. In a) the cell current is depicted and in b) the cell voltage. We see that in the charging phase of the fifth cycle, the current changes from negative to positive values during a few minutes. Table A.3 lists the solar eclipses of the period between mid of 2005 and end of 2011.

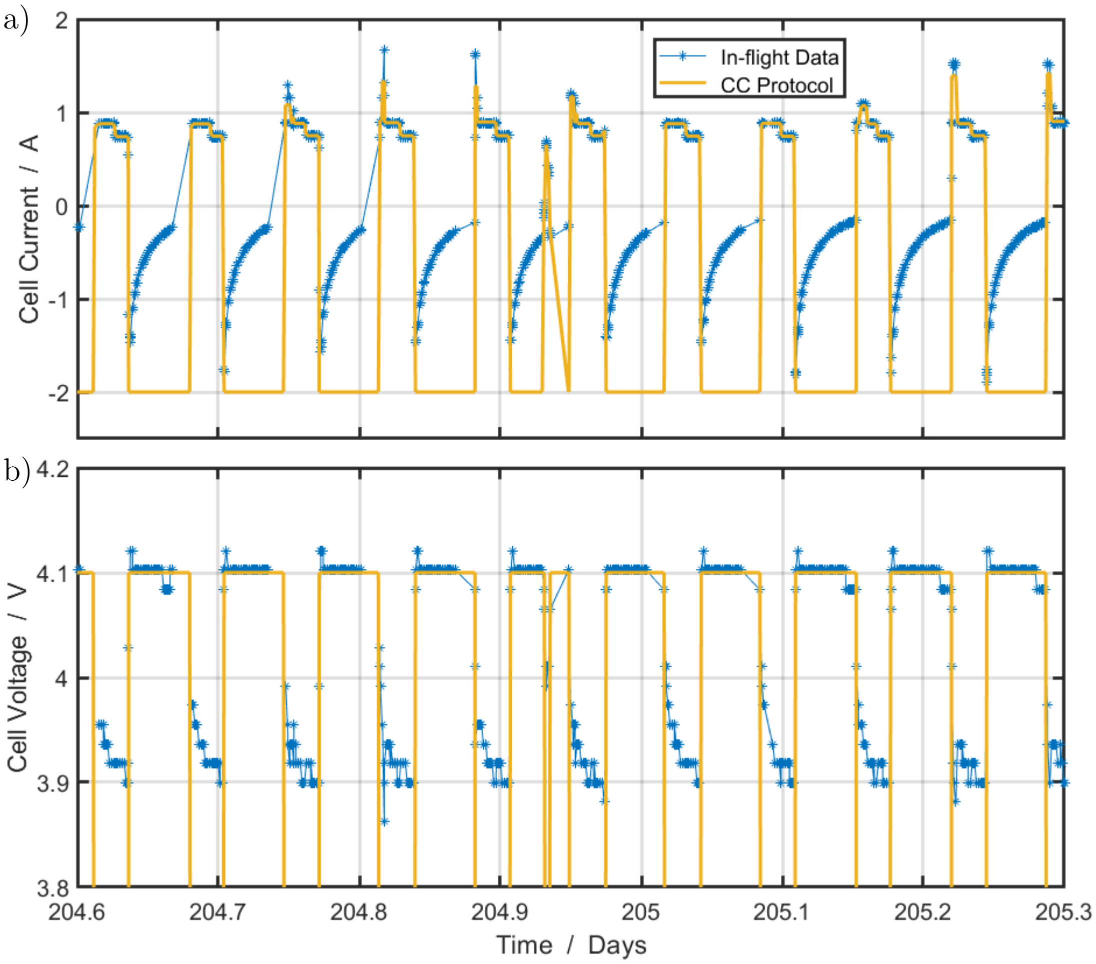

Figure 3.5: Solar eclipse on 29 March 2006. In-flight measurement data and cycling protocol. a) Cell current. b) Cell voltage.

Single Erroneous Measurement Points. Starting in 2006, there are several measurement points that seem to be shifted in time. These are all single points that prolong the typical time for charge or discharge and usually have the same value as the previous measurement point. Also, the beginning of charge or discharge immediately after the respective point seem to be in the middle of the process. An example of such points can be seen in Fig. 3.6. These points are assumed to not represent the true states of the cell and are deleted in the next section 3.4. There are further points during charge and discharge that can be assumed outliers. These are single points that, for example, have a negative current value during discharging or a very low voltage value during charging.

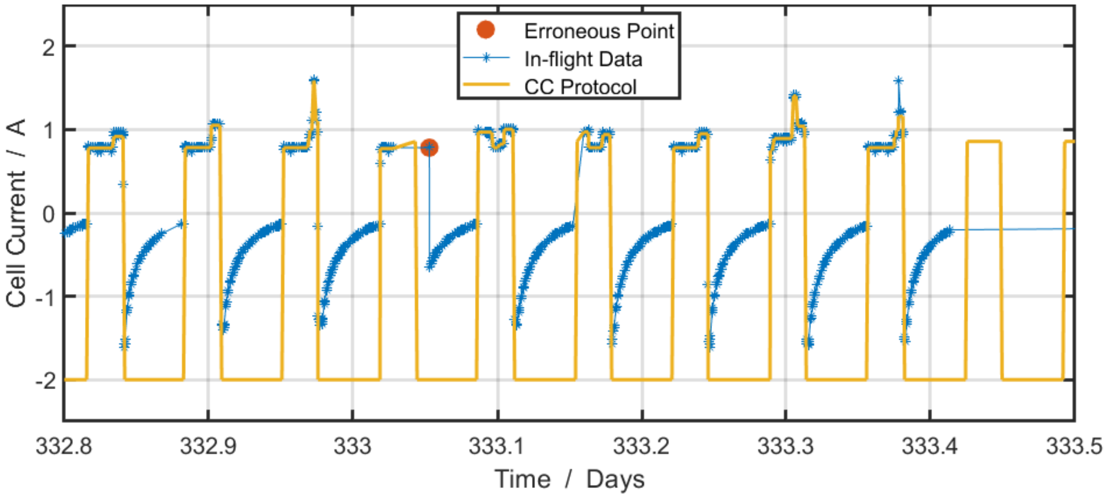

Figure 3.6: Single erroneous measurement point, which prolongs typical discharge time. In-flight measurement data and cycling protocol.

3.4 Processing of In-flight Data

The in-flight data consist of raw data without meta information like cycling protocols or time information about the cycles. The actual values for CC discharge and CV charge deviate from those given in literature, so the metadata have to be extracted from the noisy current and voltage measurements.

There are a number of challenges that need to be addressed in order to use the in-flight data for our simulations. Among these issues is that the length of the cycles varies, so a grid of time points for the beginning of cycles cannot simply be defined. Furthermore, there are short and long gaps in the data for which the input to the simulations and, in some cases, the relevant cycle times must be estimated. Outliers in the voltage and current values further complicate the characterization of the cycling.

Therefore, the data need to be processed before being used for the simulations. We performed this elaborate data processing for the in-flight data of one of the batteries for the years 2005 to 2011.

Examples of the in-flight data can be seen in Figures 3.5, 3.6, or 5.13, where the current and voltage measurement points are depicted together with the constant values of the cycling protocol.

Shift of Data Times. Another challenge is that the time stamps of the raw data are not always continuous. At larger intervals, the time stamps are reset. So these have to be shifted to get a continuous time series. The time stamps of the files, which comprise a few cycles each, help here. However, the entry cannot be assigned clearly to the beginning or end of the stored measurement. The shift is further determined in such a way that the distance between cycles consistently corresponds to the average cycle length.

3.4.1 Generation of Cycling Protocol

We want to perform simulations with the models described in sec. 2 according to the cycling of the on-board batteries, which is recorded in the in-flight data. Therefore, we need metadata that describe the cycling of the cells. These comprise the times when switching between charging and discharging, that is, the end of discharge (EoD) and end of charge (EoC). The switching from CC charge to CV charge does not have to be timed, since it is automatically switched when the upper voltage limit is reached during CC charge. During charging, the CV must be set in the protocol. During discharging, the CC values must be defined for time periods.

Charge Current. The batteries are charged with a CC/CV protocol. In the experiments the charge current is stated to be -1.5 A [19, 105]. In reality the CC part is extremely short, if even existent. Still, there is a spike at the beginning of charge followed by a curve converging to 0 A, as can be seen in Fig. 3.5 or 1.2. The first current value of the spike varies between different cycles. It is often less than -1.5 A but greater than -2 A. So, for our cycling protocol we assume a charge CC of -2 A.

CC Values. We developed an algorithm to extract CC values out of the raw data, which uses basic signal processing and statistical methods. The algorithm can be applied directly to the data and does not need additional meta information. However, this will not produce a final CC-cycling protocol but will provide a good basis for further processing the raw data and extracting metadata from it. In the whole procedure of generating a cycling protocol, the CC-value generator will be applied iteratively, to update the CC protocol after processing the data.

For the transformation of the current from raw data measurements to CC values, first, all current values less than 0.3 A are set to the charge CC. These values are assumed to belong to the charging or the switching between charge and discharge. Next, the discharge current is to be separated into ranges in which the variation of the current value is so small that it can be averaged to a constant value. This is done by identifying major changes in the current curve. This is similar to the procedure for processing the CT data that we describe in sec. 4.3.1. To do so, the vector of current measurements is convoluted with the 1D kernel (1 1 1 -1 -1 -1). This can be interpreted as a numerical first derivative [92]. The resulting signal is corrected by setting very small values to zero. This way very small changes in the current are ignored. Afterwards, the corrected signal is convoluted with a second kernel (1 1 -1 -1). The resulting signal can be interpreted as the second derivative. The zeros of this signal mark the ranges within which constant current can be assumed. The CC values are then obtained by averaging the current values in these ranges.

Cycle Duration (EoC and EoD). With the generated CC value signal, we can separate the whole time frame of the data into charge and discharge segments or, taken together, into single cycles. The first approach is to determine those points, where the sign of the current changes, which are the zeros of the signal. These are the EoD and EoC points. However, the points determined in this way still contain false candidates. These occur, for example, due to single erroneous points or due to the gaps in the data that cause the measurements at the EoD or EoC and thus the time markers to be missing. Therefore, we use our prior knowledge about the typical duration of charge and discharge from literature [19, 105]. We calculate the distances between all points and dismiss those candidates, which produce a strong deviation from the expected duration. With these corrected candidates we can generate a complete grid of EoD and EoC points, which also fills the data gaps.

Deleting Erroneous Points. With the complete grid of EoD and EoC points, we can determine points that are very likely errors in the measurement or the data, as described above. These are identified by searching the current measurements for positive values during charge and negative values during discharge. The same is done with the voltage, where a threshold is set for values during charging and discharging.

CV Values. The determination of CV values is less challenging than for the CC value, since it mostly takes the value 4.1 V. In the discrete CV measurements during charge, we can see a slow decay from the beginning of charge to EoC, cf. Fig 3.5 b). Still, we assume constant voltage. Another irregularity is the occurrence of periods of a few cycles, where the CV is greater than 4.1 V. Therefore, we determine the mean voltage of the charge phase of every cycle and set the CV value to the higher value when a threshold is exceeded.

Protocol in Data Gaps. With the complete grid of EoD and EoC points and the determined CV and CC values in the ranges, where measurements are available, we can now set a cycling protocol in the data gaps. For the charging, the CV in the gaps is set to the value of the last cycle, where the CV is known. During discharge, CC values need to be set. We determine the mean of CC values for each cycle block, that is, contiguous cycles between major data gaps. The CC value of discharges in data gaps is then set to the mean value of the cycle block prior to the gap.

Solar Eclipse. Solar eclipses, which occur during charge and therefore lead to a short period of discharge, are an exception from the erroneous points described above. Using the list of solar eclipses in the relevant period, we searched the data for extraordinary discharge phases. Not every solar eclipse has an effect on the cycling. For those, which did, the CC values for the short discharge period, caused by the eclipse, are manually adjusted. This can also be seen in Fig. 3.5 a), where the charging period of the cycle in the middle is interrupted by a short discharge period with small CC values.

4 Parameterization and Simulation of Battery Models

The long-term behavior of a battery is simulated with a model that adequately describes the processes occurring over the relevant time period. Modeling and simulation can be used to better understand the processes within the battery and to make reliable predictions for battery behavior under given conditions. In aerospace applications, it is important to be able to predict battery behavior and, in particular, the degradation of the cells, since their failure results in the satellite end-of-life.

A continuum cell model in combination with a degradation model is a promising approach to cover the whole lifetime of the battery. There are many degradation processes that occur in a Li-ion battery. Birkl et al. give a comprehensive overview of the different processes [12].

The degradation processes can occur at different times during the life of the battery. Some, such as SEI growth, occur continuously. Others, such as particle cracking, occur at a later time when the cell has already aged. Some processes, like lithium plating, only take place under certain conditions. Another aging process is the delamination of the electrodes and current collectors. This can also be seen on the CT images of the aged REIMEI cells in sec. 3.2.2.

Coupling several degradation processes is very challenging [68]. Therefore, we focus on the process, which is the main reason for capacity fading in Li-ion cells, which is the continual growth of the SEI. We investigate the capability of this process to describe the aging sufficiently.

To gain a full cell model, we combine the models described in sec. 2. We use this model to simulate the battery behavior under satellite cycling conditions, according to the terrestrial and on-board cycling experiments described in sec. 3.

To use the models described in sec. 2, they have to be parameterized with experimental data. Here, we parameterize the models that describe battery perfor-

Table 4.1: Cycling protocols used in experiments and simulations. From Bolay et al. [15].

Protocol	Charge (CC/CV)	Discharge (CC)	Temperature
P1 (in-flight)	1.5 A / 4.1 V 63 min	0.88 A 0.74 A 15 min 19 min	20°C
P2 (P2D)	1.5 A / 4.1 V (4.2 V) 65 min	1.0 A 35 min	25°C
P3 (3D)	1.5 A / 4.1 V 65 min	1.0 A 35 min	25°C
P4 (3D)	1.5 A / 4.1 V 65 min	2.0 A 35 min	25°C
P5 (3D)	3.0 A / 4.1 V 65 min	2.0 A 35 min	25°C

mance and degradation with different parameterization techniques using several experimental data described in sec. 3. We first parameterize the P2D model and subsequently the degradation model, where we use the previously determined parameters of the P2D model. However, since the models are coupled and the parameters of one model affect the behavior of the other, we also consider the parameters of the respective other model in each parameterization step.

Furthermore, we use the parameterized models to simulate the satellite battery with corresponding cycling protocols in a P2D and 3D framework. The simulation in 3D provides further insights into the processes on a microstructural resolution.

We already described this parameterization procedure in Ref. [15]. We will reproduce the content here and explain it in more detail.

The degradation with the P2D model is implemented in MATLAB [61]. The 3D model is implemented with the software BEST [43]. Both kinds of simulations are run on the high performance computer cluster JUSTUS 2, which belongs to the bwHPC.

Table 4.1 presents an overview of the cycling protocols used in the following sections for simulations of satellite cycling.

4.1 Full Cell Model

For the simulation of the battery behavior, we couple the SEI model to the continuum model for Li-ion cells. We describe the full model for the P2D framework.

First, we consider the equation for the SEI flux, cf. eq. (2.16). We adapt this to be able to control the influence of electron migration in the SEI. Therefore, we insert the parameter ω, which serves as a multiplicative factor.

$$N_{\mathrm{SEI}} = \frac{D^{e^-} \cdot c_0^{e^-}}{L_{\mathrm{SEI}}} \cdot \exp\left(-\frac{F}{RT}\eta_{\mathrm{SEI}}\right) \cdot \left(1 - \omega \cdot \frac{F}{RT} U_{\mathrm{SEI}}\right). \tag{4.1}$$

Setting $\omega = 0.5$, we obtain the original equation as derived by von Kolzenberg et al. [48] and described in sec. 2.2. Schmitt also uses the parameter ω in his theory on SEI growth [89].

The consumption of free Li-ions by the SEI growth is considered in the model in the Li-ion flux between electrode and electrolyte, where the amount of Li-ions that reach the electrode is reduced by the SEI flux, see eq. (2.16). The resulting current density is given by $j_{\mathrm{res}}^{\mathrm{Li}^+} = A_{\mathrm{spec}} \cdot (j^{\mathrm{Li}^+} - F \cdot N_{\mathrm{SEI}})$, cf. eq. (2.6).

In the Butler-Volmer equation, the coupling of the models becomes important. The current density j^{Li^+}, which is calculated with the Butler-Volmer equation, cf. eq. (2.6), requires the potential drop U_{SEI} for the determination of the overpotential. In the calculation of U_{SEI} the current density is in turn included, cf. eq. (2.14). This shows that the system of equations can only be solved implicitly and that battery performance and degradation cannot be treated decoupled.

Another effect that influences the battery behavior with progressing degradation by the SEI growth is the increase of the internal resistance. This is considered in the Butler-Volmer equation for the anode, cf. eq. (2.18). The increase in the internal resistance is noticeable in the cell voltage and EoDV, which take on smaller values during discharge.

The cell voltage is obtained from the model with the potentials of cathode and anode via

$$V_{\mathrm{sim}} = \Phi_{\mathrm{cathode}} - \Phi_{\mathrm{anode}}. \tag{4.2}$$

The cell current density is obtained with

$$I_{\mathrm{sim}} = -A_{\mathrm{spec,cathode}} \int_{x_0}^{x_1} j_{\mathrm{cathode}}^{\mathrm{Li}^+} dx, \tag{4.3}$$

which is evaluated numerically between the limits x_0 and x_1, which border the domain of the anode between current collector and separator.

For the numerical simulation of the P2D model with finite difference method, in this chapter, we choose the following discretization. The electrodes are discretized with differences of about 2 μm, which results in 23 nodes for the anode and 37 nodes for the cathode. For the separator, we choose a coarser discretization of 10 nodes. The radii of the electrode particles are discretized with 10 nodes. The nodes are equidistant in each domain.

When switching between constant currents during the cycling simulations, it is necessary to use a smooth current ramp for the numerical solver to be stable. This is also in accordance with the switching in reality. We choose a ramp-time of 5 seconds.

The parameters of the P2D model are listed in Table B.2 and those of the SEI model in Table B.4.

4.2 Parameterization Methods

One important aspect in physics-based modeling is the determination of accurate model parameters. There are several approaches to gain these parameters, depending on the different kinds of parameters like for example transport parameters or morphological parameters, and depending on the experimental data that is available.

4.2.1 Experimental Techniques

The parameters for the P2D model can be determined through different experimental techniques. Chen et al. suggest an approach to identify the parameters of the P2D model experimentally [23]. In Ref. [29], Ehrl et al. describe how to determine the transport parameters of electrolytes.

For example, the OCV curves of the electrodes can be determined by galvanostatic intermittent titration technique (GITT) measurements. Focused ion beam scanning electron microscopy (FIB-SEM) can be used to determine parameters that describe the electrode structure [23, 18].

In the following, we describe the experimental techniques, that we use to extract parameters from the cells of satellite REIMEI. These are limited to the micro computed tomography (micro CT) data described in sec. 3.2.2.

Image Analysis

Morphological parameters like the porosity of materials or thickness of layers can be extracted from image data. These data are obtained by imaging techniques like micro CT or FIB-SEM. The latter can only be applied if the object that is to be analyzed can be destroyed [23]. The major advantage of CT imaging is that virtual three-dimensional (3D) representations of objects can be gained without destroying the object. Ohser et al. give a comprehensive description of the processing of 3D images for the analysis of materials [67]. In the following, we will describe techniques to process 3D images in order to extract parameters of the P2D model.

Computed Tomography (CT) Data. To generate a 3D CT image of an object, X-rays irradiate the entire volume of the object and project it onto a plane, while the object rotates. From the projection images, a three-dimensional gray value image is reconstructed. The gray value represents the magnitude with which a region absorbs the radiation. In Fig. 3.3, CT images of a Li-ion cell is shown. In the images with higher resolution (a) and (b), several layers of different materials can be seen. The light thin layer for example is a copper metal foil, which is represented by high gray values.

Image Preprocessing. To take care of noise in the image data, it might be necessary to preprocess the CT image. Therefore, every voxel of the gray value image is processed. Usually, this is done by determining the average of gray values in the neighborhood of a voxel. The neighborhood is a set of voxels surrounding the currently considered voxel. This can be for example a cube with edge length three or five. To compute the average of gray values, typically, the mean or median is used.

Segmentation. One essential tool in analyzing CT images of material structures is the segmentation of objects or areas in the structure. The gray valued image is converted to an image where the value of a voxel classifies it as belonging to a specific object or to the background. One of the simplest approaches is to generate a binary image by setting a threshold where voxels with a gray value larger than the threshold are assigned the value one and the other voxels are set to zero.

Separation of Layers. In order to investigate different materials in homogeneous areas of a layered structure, these layers have to be separated. With this separation, also the thickness of the individual layers can be determined.

As the layers of the structure might not be parallel to the voxel layers of the CT image, first, they have to be tilted. To determine the orientation of the planes separating the layers, a representative layer can be identified to determine its orientation. This could be a layer of some homogeneous material that has a high contrast in the gray value compared to its surrounding, like a metal. The layer is segmented with a suitable threshold. Next, the point cloud of the segmented voxels is fitted with linear regression to gain a plane of the form $y = b_1 \cdot x_1 + b_2 \cdot x_2$. With this, the whole 3D image gets rotated so that the plane is parallel to the voxel layers.

Next, a criterion is calculated to distinguish different layers in the structure. This can be the median of gray values, which differs for different materials. Since the layers shall get separated along the voxel layers, the median of the gray value is determined for every voxel layer parallel to the structure layer. This results in a one-dimensional (1D) array of gray values. Subsequently, this array can be processed with signal processing methods to determine major changes in the gray value, which indicates a transition from one layer to another.

Porosity. After separating layers of homogeneous material compositions, characteristics of the material morphology like porosity and surface properties can be studied.

The simplest approach to distinguish pore voxels from material voxels in a CT image is the aforementioned threshold segmentation. A gray value is determined so that voxels with a gray value smaller than the threshold are labeled as pore space and those with a gray value larger than the threshold are labeled as belonging to the material. To find a suitable threshold, the overall distribution of gray values is identified with a histogram. This typically results in a bimodal distribution, where a point between the two modes is chosen as the threshold. This approach has the drawback that for some material compositions the modes of the distribution can not be clearly separated as the gray values of different phases overlap. This might be due to the quality of the CT image or the kind of material in the structure. In this case, a more complex method is required.

In Ref. [78], Prifling et al. propose a sophisticated method to segment CT images of structures consisting of three phases. The basic idea of this method is to reproduce the distribution of gray values with the determined segmentation. Therefore, first, the distribution of gray values of a representative section of the CT image is identified. This distribution is approximated by a combination of three normal distributions. These are a measure for the volume fractions of the three different phases.

Next, after some intermediate processing steps, all voxels are classified into three classes with k-means clustering. The classification of every voxel is performed based on feature vectors, which are arrays of the gray values in the neighborhood of the currently considered voxel [78].

After that, a post-processing step is undertaken, where small spots in the three different regions are removed. The quality of the final segmentation can be validated by comparing the distributions of the gray values in the segmented regions to the initially determined distributions [78].

Specific Surface Area. To compute the specific surface area of an object, which is represented by a set of voxels, the easiest approach would be to count the external surfaces of the voxels. However, this approach overestimates the surface area of the object obviously. A more sophisticated approach is explained in Ref. [66], where the surface is approximated by a grid that connects the vertices of the voxels.

4.2.2 Optimization Techniques

Parameters of the cell model can also be determined by an optimization using experimental data that can be simulated with the model. The optimization algorithm then minimizes the deviation between experiment and simulation, given as an objective function.

The optimization algorithm should find the global minimum and preferably it is parallelizable as the evaluation of the time-evolution of our physics-based model is time-consuming. There are several optimization algorithms suitable for the search of a global minimum, like particle swarm optimization, genetic algorithm, or simulated annealing [31, 81].

Here, we describe the surrogate optimization, which is a stochastic optimization algorithm. The benefits of this algorithm are that its convergence to the global optimum is proven and that it can run in parallel [82].

Surrogate Optimization

We briefly outline the algorithm for surrogate optimization. For further details, we refer to Refs. [82, 109]. In a first phase, the algorithm evaluates the objective function for a given number of points, which are randomly chosen in the given parameter space. These points get interpolated by radial basis functions to build a surrogate function.

In the next phase, the point with the smallest value is found. Around this point, multiple points are sampled and an additional merit function is evaluated at these points. The merit function consists of the surrogate and a function that describes the distance of sampled points to already evaluated points. This ensures that the surrogate function is minimized while searching in new regions. At the point, where the merit function has its minimal value, the objective function is evaluated and the surrogate function is updated.

This procedure is repeated until a stopping criterion is reached. Subsequently, the surrogate gets rejected and a new surrogate is created with new random points, while the best fit of the previous surrogate is kept for comparison. This overall procedure of generating new surrogate functions can be repeated until the global optimum is found. Usually, the search for the optimum is stopped after a predefined time.

4.3 Parameterization and Simulation of P2D Cell Model

We simulate battery cycling with the volume-averaged P2D model. To simulate the specific satellite batteries according to the cycling in space, we parameterized the model with experimental data of the corresponding cells.

The parameterization of the P2D model is a challenging task, which can be addressed by optimization techniques, where the error between experiment and model simulation, depending on the parameters, is to be minimized. Different approaches can be found in the literature. Forman et al. use a genetic algorithm to identify the parameters of the P2D model [31]. Rahman et al. use a particle swarm optimization algorithm [81].

Several battery parameters are to be determined. We extract the parameters describing the microstructure morphologies from CT data. These are layer thicknesses, porosities, and specific surface areas. The concentration-dependent electrolyte parameters are taken from Ref. [29]. The OCV curves of the electrodes we fit to the measured curves in Ref. [20]. The remaining cell parameters, which are the maximum Li concentrations, diffusion coefficients, and rate constants, we determine with an optimization algorithm, where experimental data of a fresh cell from Ref. [105] are used. All parameters can be found in Table B.1 and B.2.

Since we use the full cell model, where the P2D model and the degradation model are coupled, we also have to take the degradation parameters into account.

4.3.1 Parameterization with Experimental Techniques

We determine some of the parameters with experimental techniques. In this special use case of the batteries of satellite REIMEI, it is difficult to gain all parameters experimentally, since the cell development and testing were done a long time ago. Part of the available experimental data of the cells are micro CT measurements (see sec. 3.2.2). From the CT images with 1 μm and 3.5 μm resolution, we extract the thicknesses and porosities of anode, cathode, and separator and the specific surface areas of the electrode particles with the methods described in sec. 4.2.1. Since the cells were already aged, it may occur that certain determined parameters differ a little from those of the fresh cell.

Furthermore, we fitted the OCV curves of the electrodes, which were measured with GITT (see sec. 3).

Thickness of layers. The thickness of anode, cathode, and separator is determined by separating the layers of the micro CT image of the cell as described in sec. 4.2.1. The 3D image gets tilted so that the layers of the cell are parallel to the voxel layers. Then the median gray value is determined for every voxel layer. The resulting 1D representation of the layers can be seen in Fig. 4.1 as the blue line. The plateaus of the material layers can be distinguished by eye.

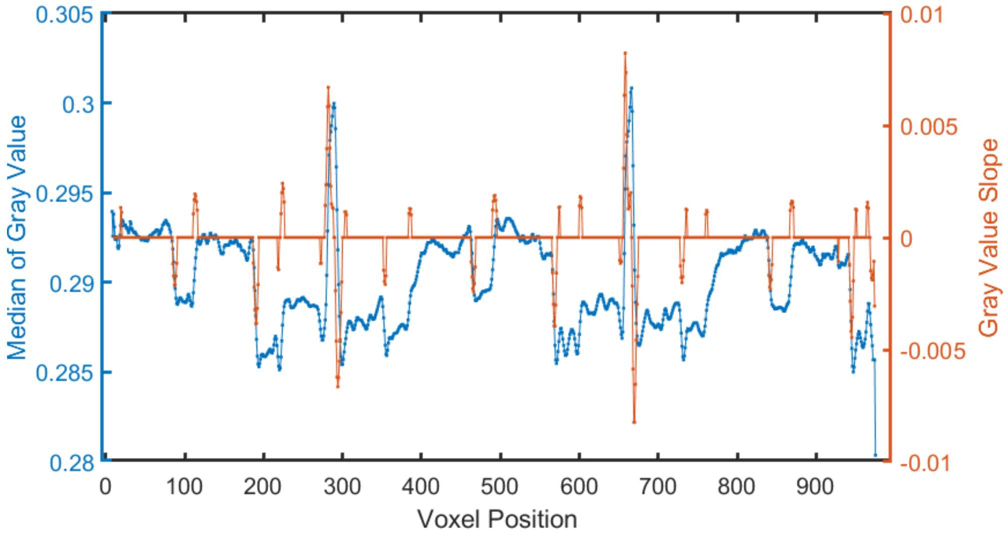

Figure 4.1: Array of gray value medians for voxel layers in a layered structure.

To identify the exact interface between the layers, the second derivative of the 1D vector of gray values is determined. This gives peaks at the points where there is a change between the gray values. The large changes represent the interfaces. Using a threshold the relevant peaks can be selected. These peaks are shown as an orange curve in the figure. Since we have several layers of the same material in one micro CT image, we determine the mean thickness of all layers of one kind. In Fig. 4.2, we see the resulting separated layers.

Porosities. The porosities ϵ of the different electrodes are determined from a representative section of the 1 μm resolution CT image. The histogram of gray values within this volume is determined and approximated by the combination three normal distributions.

In Fig. 4.3, we show exemplarily the histogram (blue curve) and the corresponding distribution approximation (red curve) for the cathode. The integrals of the distributions yield the volume fractions of the phases in the electrode, the pore space (yellow curve), the active solid phase (purple curve), and the passive solid phase (green curve), which consists of binder and conductive material. From the distributions, we get a binarization of the electrode volume using k-means clustering. We use a simplified version of the method described in Ref. [78]. Here, we only want to classify the voxels as pore space or solid phase. The classification is assumed sufficient, when the gray value distribution classes have the same integral

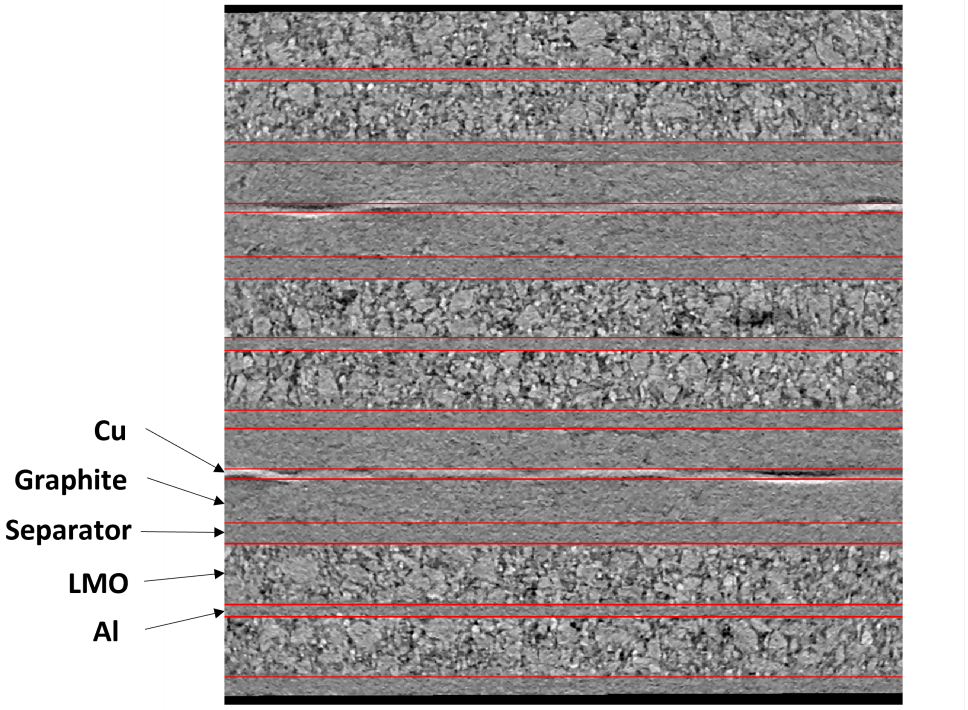

Figure 4.2: Micro-CT of Li-ion cell with separated layers of current collectors, electrodes, and separator.

as the approximated distributions.

For the separator we proceed in the same way as for the electrodes. However, here the histogram of the gray values is approximated by only two normal distributions. The porosity is then again obtained from the integral of the distributions.

Specific Surface Area. We use the binarization obtained in the determination of the porosities to determine the specific surface area A_{spec} of the electrodes. We do this with the software GeoDict [60], which uses the approach described in Ref. [66].

Cell Area. In the experiments of Brown et al. [19, 20] and Uno et al. [105], the cell current is sometimes given in A and sometimes in A m^{-2}. The full cell area A_{cell} is required to convert into one or the other unit. To determine this value, the width, length, and number of cell layers are needed. The length is taken from the CT image with 140 μm resolution, which shows the whole cell. The width and number of layers are taken from the CT image with 24 μm resolution, which

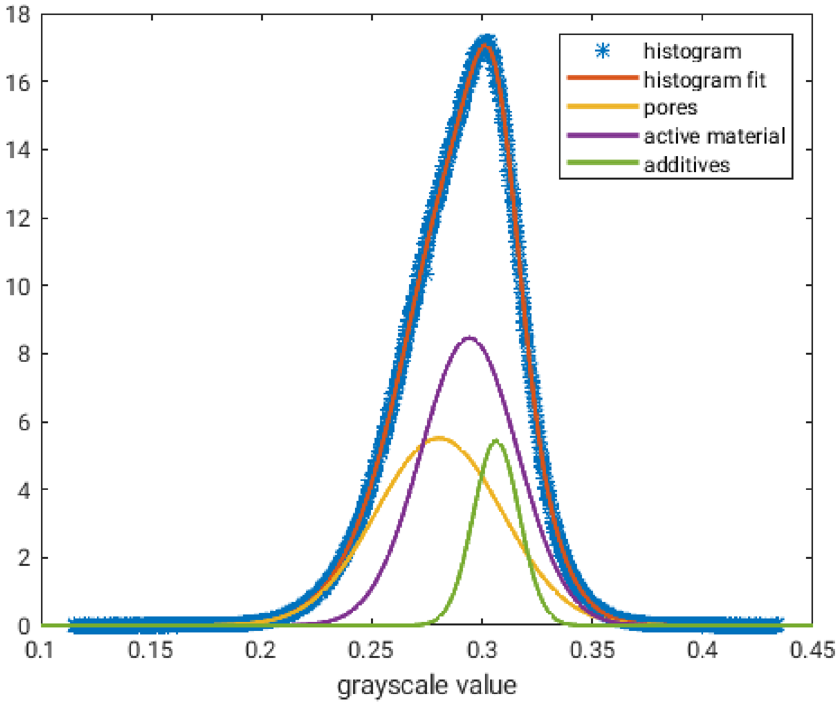

Figure 4.3: Histogram of cathode gray values and corresponding distribution approximation. From Bolay et al. [15].

shows the upper part of the cell. We get $A_{\text{cell}} = 0.139\ \text{m}^2$.

OCV Curves

Brown et al. measured charge and discharge curves of half cells for both electrodes [20]. They performed the cycling with a current rate of C/10. With this slow current, the hysteresis is quite small. We fit the OCV curves for anode and cathode to the median of the cycling curves. The resulting curves are shown in Fig. 4.4 and 4.5, where the blue lines show the measurements and the red line shows the fitted curve. The left side shows the entire measured area. The right side zooms into a detailed area. The corresponding eq. (B.1) and eq. (B.2) can be found in sec. B. In Fig. 4.5, we see that the OCV of the cathode is extended beyond the measurements, which is necessary for the simulations being numerically stable. This definition of the SOC is arbitrary and can be adapted by scaling.

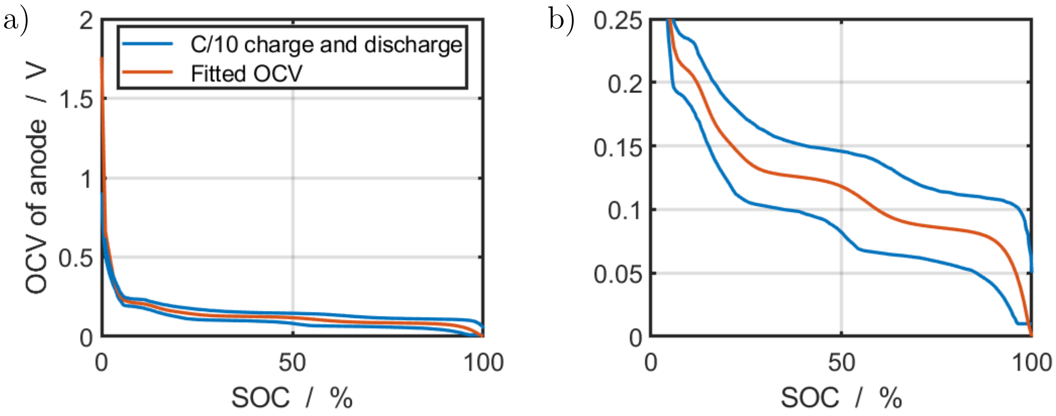

Figure 4.4: Anode OCV. Measured curves of C/10 charge and discharge and fitted OCV curve. a) Entire measured area. b) Zoom-in to detailed area.

4.3.2 Parameterization with Surrogate Optimization

The parameters of the cell model, that are not known from literature or measurements, are determined with an optimization. The optimization algorithm searches for the optimal parameters that minimize the deviation between experiment and simulation, given as an objective function.

The remaining parameters determined this way, are the initial SOC of the anode and, for both electrodes, the respective maximum concentration of Li-ions in the active material $c_{\mathrm{s,max}}$, the diffusion coefficient of Li-ions in the active material D_{s}, and the rate constant k. The cathode SOC can be set to a fixed initial value and is adapted via the anode SOC.

We use the surrogate optimization because of the previously mentioned advantages, cf. 4.2.2. To the best of our knowledge, this is the first time that the surrogate optimization has been used to identify parameters of the P2D model.

The parameters of the battery cycling and those of the degradation are correlated. Thus, the parameterization of both models needs to be linked to each other. For that purpose, the degradation parameters are also taken into account in this section.

To determine the parameters of the REIMEI battery cell, we simulate the cell model with changing parameter settings and compare them to the experimental data of Uno et al. [105] described in sec. 3.2.1. According to the experiments, we simulate two full discharges with 1 A from 4.1 V to 3.0 V, which are used to

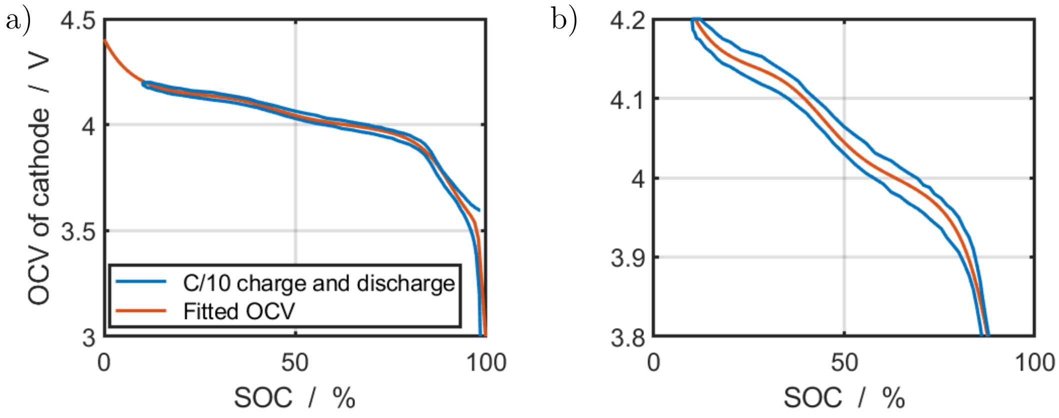

Figure 4.5: Cathode OCV. Measured curves of C/10 charge and discharge and fitted OCV curve. a) Entire measured area. b) Zoom-in to detailed area.

determine the cell capacity, followed by several cycles with the satellite protocol P2 (see Table 4.1). We compare the second full discharge of our simulation to the corresponding initial discharge curve of the experiment. The EoDV after several cycles is compared to the value at the beginning of the EoDV measurements. The EoDV error gets measured after a few cycles, since the cycling range has to level off after full discharge in the experiment as well as in the simulation. Fig. 4.6 shows the cell voltage of the cycling. We set the beginning of the second discharge to zero. This way the capacity can be read directly. The parts of the simulation used to evaluate the error in the optimization are highlighted in red.

The objective function for the optimization is a weighted sum of the discharge curve error $\mathrm{err_V}$ and the EoDV error $\mathrm{err_{EoDV}}$. We define the function as $f_{\mathrm{objective}} = 1 \cdot \mathrm{err_V} + 2 \cdot \mathrm{err_{EoDV}}$. We choose the L^1-Norm to measure the discharge curve error:

$$\mathrm{err_V}(\theta) = \int_T |V_{\mathrm{exp}}(t) - V_{\mathrm{sim}}(t;\theta)|dt, \tag{4.4}$$

where V_{exp} is the experimental voltage and V_{sim} is the voltage output of the simulation (cf. eq. (4.2)) over the discharge time T for a given parameter vector θ. And $\mathrm{err_{EoDV}}$ is the difference between the last EoDV value of the simulation and the EoDV at the beginning of the long-term cycling experiment.

The parameters are optimized in a reasonable parameter space. The parameter window for the maximum Li concentration is $c_{\mathrm{C,max}} \in [28000, 34000]$ mol m^{-3} for the anode and $c_{\mathrm{LMO,max}} \in [21500, 26000]$ mol m^{-3} for the cathode. For the

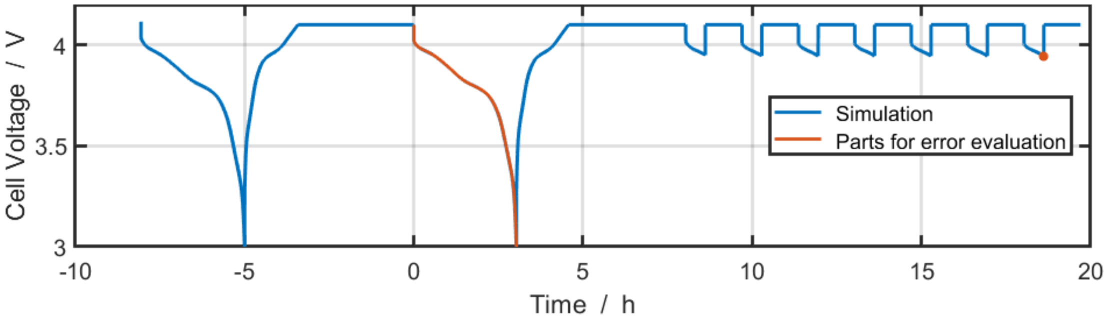

Figure 4.6: Cell voltage of cycling protocol for the parameterization of cell model. Two full cycles for determination of cell capacity followed by several cycles with typical satellite protocol (cf. P2 in Table 4.1). Simulation parts relevant for error evaluation are highlighted.

diffusion coefficients of Li in the electrodes $D_{\mathrm{C}} \in [10^{-15}, 10^{-12}]$ m^2 s^{-1} for the anode and $D_{\mathrm{LMO}} \in [10^{-15}, 10^{-12}]$ m^2 s^{-1} for the cathode. For the rate constants in the Butler-Volmer term $k_{\mathrm{C}} \in [10^{-6.5}, 10^{-4.5}]$ A m$^{5/2}$ mol$^{-3/2}$ for the anode and $k_{\mathrm{LMO}} \in [10^{-7}, 10^{-5}]$ A m$^{5/2}$ mol$^{-3/2}$ for the cathode. And for the initial SOC of the anode $\mathrm{SOC}_{\mathrm{C},0} \in [75, 99.5]$ %.

The degradation parameters for the simulations are the initial SEI thickness $L_{\mathrm{SEI},0} = 10$ nm, the diffusion coefficient of localized electrons in the SEI $D^{e^-} = 10^{-12}$ m^2 s^{-1}, the conductivity of Li-ions in the SEI $\kappa_{\mathrm{SEI}}^{\mathrm{Li}^+} = 10^{-5}$ S m^{-1}, and the migration factor $\omega = 0.5$. The choice of the degradation parameters will be explained in more detail in sec. 4.4.1.

With this setting the surrogate optimization is run in MATLAB on a computer cluster, using the implemented surrogate optimization function. It is executed with 16 parallel processes. The stopping criterion for the algorithm is a maximum time of about 48 hours. Another parameter of the algorithm, which can be adapted, is the minimum number of initial random points in the parameter space that are evaluated in every phase. We choose this number to be 21, which is three times the number of parameters.

Fig. 4.7 shows parts of the optimization process. In a) and c) the value of the objective function is depicted. It is plotted with a logarithmic axis to make the minima of each phase distinguishable. To demonstrate the behavior of the parameter optimization, we pick one of the parameters exemplarily. Plots b) and d) show the progress of the rate constant of the cathode k_{LMO}. For this parameter, we vary the exponent to base 10. The y-axis shows only the exponent. The whole optimization process is depicted in a) and b), while c) and d) show a zoom-in to four phases.

The algorithm performed 84 phases in the time given before the maximum time was reached. In a) we see that the individual phases have different durations and that they find different minima.

At the beginning of each phase, random points at which the objective function is evaluated are chosen in the parameter space. This can be seen especially in d), where the random points are highlighted in color. Subsequently, the corresponding surrogate function is minimized. This can be seen on the one hand in a) and c), where the values converge to a local minimum, and on the other hand in b) and d), where the value of the parameter also converges in each phase. It is remarkable, as one can clearly see in b), that the value towards this parameter converges is often in the same range around -6.3, apart from a few outliers that take on a high value. Since the evaluation of individual points runs in parallel, the values do not converge monotonically.

In c) and d), we see that a small minimum of the objective function corresponds to those values of the parameter that lie in the favored range around -6.3. This suggests that the optimal parameter can be found in that range. However, the objective function also depends on the other parameters.

To analyze the distribution of the values to which the parameters converge during the optimization phases, we visualize them in Fig. 4.8 with boxplots. These show the medians, quartiles, minima, maxima, and outliers of the temporary optimal parameters. The y-axis of the diffusion coefficients and the rate constants show the exponents to base 10. For some parameters like k_{LMO} and $c_{\mathrm{C,max}}$, the window of the box is small, which means that the surrogate optimization finds 50 % of the optimal parameters in this small range. For most of the parameters, the maximum value reaches the upper limit of the search window. This suggests to search for values above this maximum. But as the parameter windows were chosen in a physically sensible range and the medians have enough distance to the limits, these windows are assumed to be appropriate.

The analysis of the distribution of the temporary optimal parameters may give a hint on the actual optimal parameter and the identifiability of the parameter. Also, it can be used to change or narrow down the window in which parameters are optimized. However, it is not possible to select the median value for each parameter in order to define the optimal parameter set, because the parameters may depend on each other.

To that end, it would be interesting to analyze the correlation between the param-

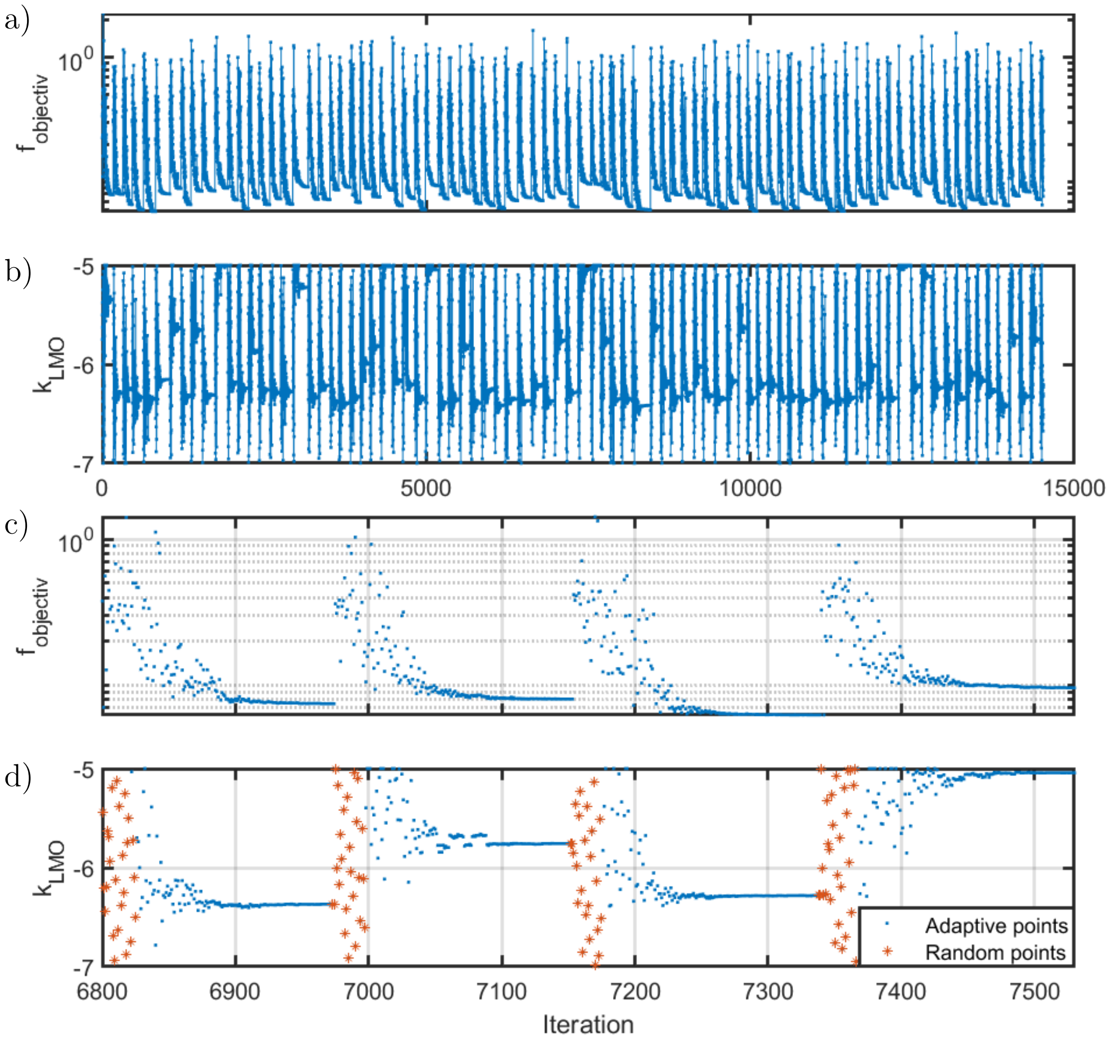

Figure 4.7: Surrogate optimization for the determination of cell model parameters with progress of one exemplarily model parameter. a) Progress of objective function during optimization process. b) Progress of rate constant of cathode during optimization process. c) Zoom-in to four phases of the optimization. d) Corresponding phases of the parameter.

eters to be able to make further conclusions about the identifiability. In former tests, we investigated the correlation between the initial SOCs of anode and cathode. We found that they are linearly correlated, which is why only the SOC of the anode is included in the study presented here.

Here we do not investigate the correlation of the parameters further, but choose the parameter set that the algorithm has determined to be the optimal set based on the minimum value of the objective function. The resulting discharge curve

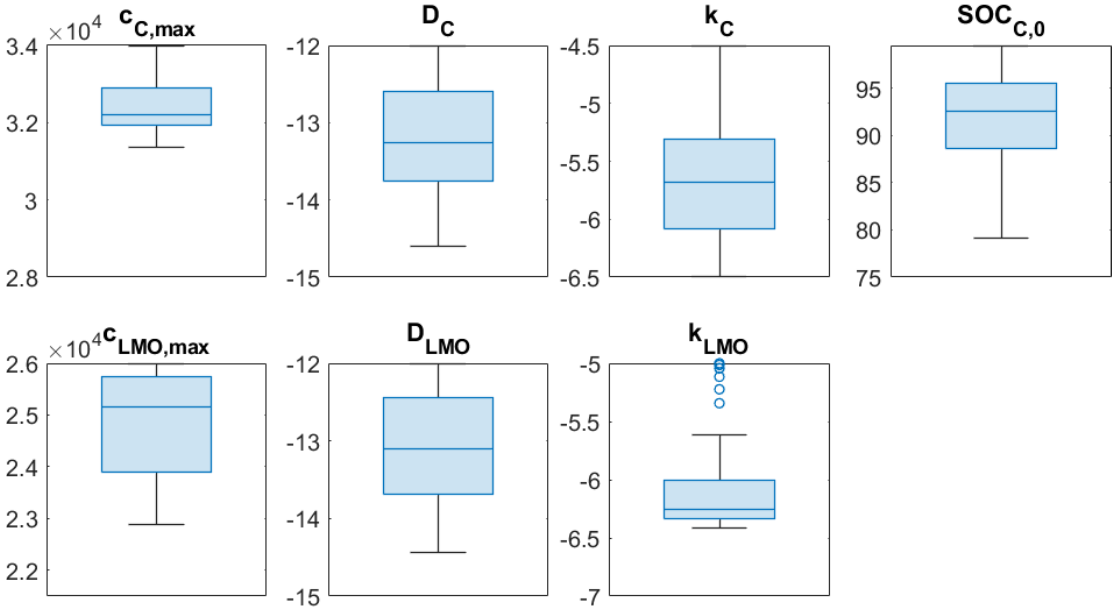

Figure 4.8: Boxplots of the output from surrogate optimization. The surrogate algorithm provides an incumbent best fit of every parameter in each surrogate phase.

of these optimal parameters is shown in Fig. 4.9. The experimental discharge curve from Uno et al. is depicted in blue dots and the simulation curve in red. The simulation matches the experiment very well. Especially, at the beginning and at the end of the discharge they agree perfectly. This also means, that the simulation matches the capacity of the cell, which is of further importance for the degradation simulation.

The resulting optimal parameters can be found in Table B.2. As the algorithm stopped due to a time stopping criterion, it is not guaranteed that the surrogate optimization algorithm determined the global optimum. Also, it has not been shown yet that the parameters of the P2D model are identifiable at all. Bizeray et al. showed the identifiability for the single particle model in Ref. [13], which is a reduced version of the P2D model. In Ref. [53], Li et al. analyzed the sensitivity of the P2D model parameters. They showed that only part of the parameters is identifiable. However, for our purposes, the result is sufficient to be used in the next step, where we determine the parameters of the degradation model.

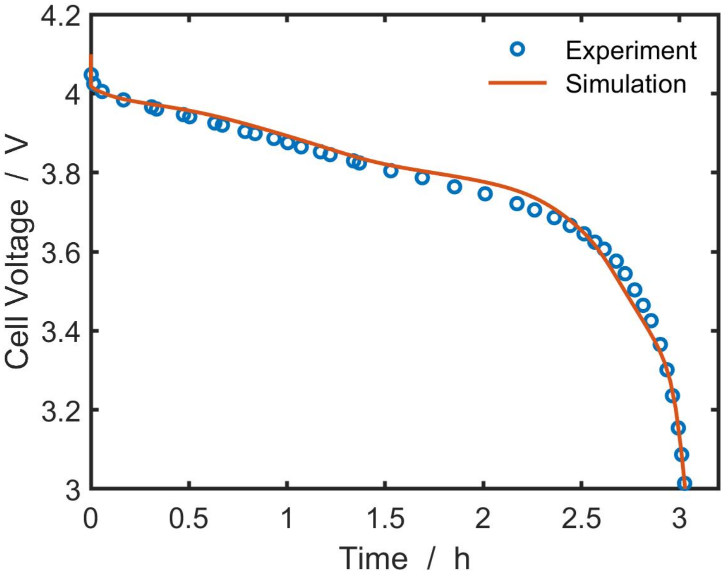

Figure 4.9: Simulation of capacity measurement with optimal parameters determined with surrogate optimization. From Bolay et al. [15].

4.3.3 Simulation and Validation with In-flight Data

To validate the determined parameters, the satellite in-flight data are used. On orbit, the cells get charged via the solar panels with a CC/CV profile. During the eclipse period, they get discharged to power the cameras for the aurora observation. There are two different discharge profiles, depending on whether the aurora of the north or the south pole is observed. The cycling protocols are described in detail in Ref. [19].

In Fig. 4.10, the simulation of the in-flight data is depicted. The data were taken from the early life of the battery in 2005. The cycling protocol, that has been used during this period of satellite operation, was for north pole observation, where the cells get charged with CC of 1.5 A followed by a CV of 4.1 V. For the discharge, two different constant currents are used. The cells get discharged with 0.88 A for 15 minutes followed by 0.74 A for 19 minutes. This results in a total discharge time of 34 minutes. The protocol can also be found in Table 4.1 (P1).

In the figure, we show the agreement between simulation and experiment over the course of three cycles. The cell current, which is depicted in red, is met by the simulation only during discharge, which is obvious, since the current is the input of the simulation during discharge. During charge, the simulation does not fit the cell current, since this was not part of the objective function of the parameterization.

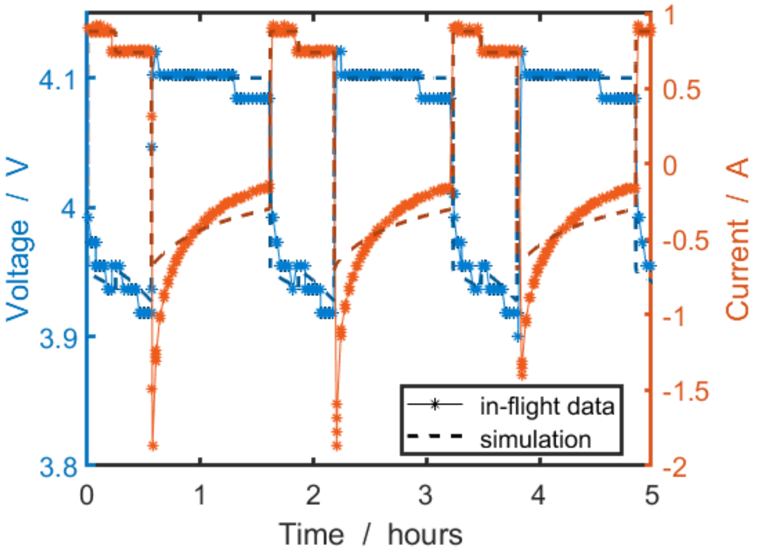

Figure 4.10: Three cycles of the satellite REIMEI battery. In-flight data and simulation corresponding to the satellite cycling protocol of north pole observation. In-flight data from beginning of satellite lifetime. From Bolay et al. [15].

For the voltage curve, it can be seen that it is in accordance with the simulation during charge and discharge. During charge, the major part of the input of the simulation is constant voltage. In the experimental data, it looks like there are three different values for constant voltage. However, this is only due to a slight drop in the constant voltage, which is represented as voltage steps due to the measurement inaccuracy. The step in the voltage discharge curve caused by the drop in the constant current is reliably reproduced by the simulation, which was also the main focus of the parameterization. From this, we can conclude that the determined parameters of the cell model are appropriate to describe the satellite cell behavior also during flight.

4.4 Parameterization and Simulation of Degradation Model

To gain insight into the aging of the cells, we use the degradation model and perform long-term simulations in different resolution frameworks. To be able to use the model, it first has to be parameterized. Subsequently, the parameterized model can be used for simulations.

Until recently, electrode level continuum models had not reproduced the experimentally observed SEI heterogeneity [71, 104]. In his PhD thesis, Schmitt implemented a preliminary version of the model of Ref. [48] in the software BEST [43] and simulated the growth behavior in a 3D resolved microstructure. Thereby, it was shown that the SEI is growing inhomogeneously [89]. This was the first time that experimentally observed inhomogeneities in the SEI thickness could be shown with a physics-based model. Considering reaction-limited growth, such heterogeneous SEI growth has also been recently analyzed by Chouchane et al. [24].

Here, we discuss how to parameterize and simulate the SEI growth in a pseudo-two-dimensional (P2D) framework and in 3D. With this, we show inhomogeneous long-term growth of the SEI.

To determine the parameters of the degradation model, long-term cycling is simulated with the full cell model in a P2D framework, cf. sec. 4.4.1. The simulation output is compared to the long-term cycling experiments described in sec. 3.2.1. Subsequently, 3D simulations are performed with the determined parameters. Different cycling protocols are used to examine the influence of charge and discharge currents on the SEI growth in the microstructure (see sec. 4.4.2).

The parameterization of the degradation model is carried out with the P2D model and not with the 3D model, which is much more expensive in terms of computation time. As many simulations are required, the computation time is crucial here.

4.4.1 Parameterization with P2D model

We simulate the long-term cycling protocol according to the experiments of Uno et al. [105]. They cycled the cells about 27,000 times. After around 24,000 cycles, when the EoDV reaches 3.75 V, the charge voltage is changed from 4.1 V to 4.2 V. At 12 different points in time, the cells are fully discharged to 3.0 V to measure the remaining capacity. This can also be seen in Fig. 4.11. The cycling protocol used here can be found in Table 4.1 (P2).

The degradation parameters, examined in this subsection, are the initial SEI thickness $L_{\mathrm{SEI},0}$, the diffusion coefficient D^{e^-} of localized electrons in the SEI, the conductivity $\kappa_{\mathrm{SEI}}^{\mathrm{Li}^+}$ of Li-ions in the SEI, and the migration factor ω. The other parameters, like the mean partial molar volume of the SEI, contribute to the

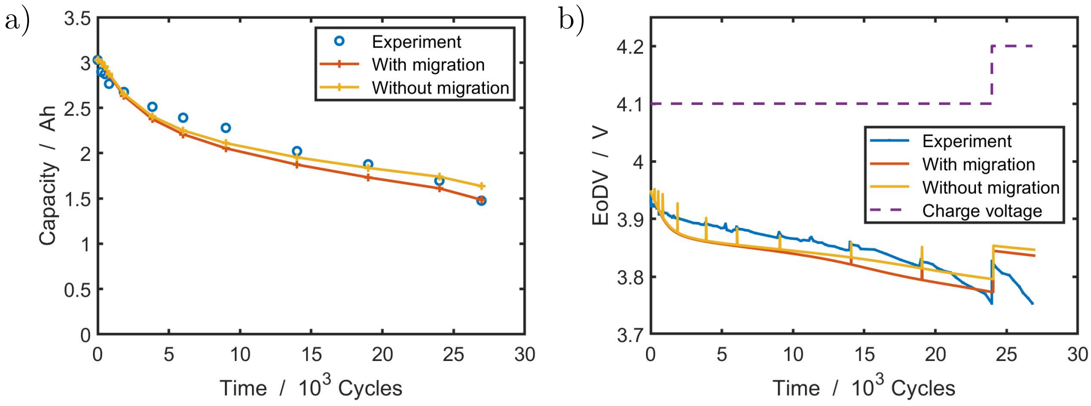

Figure 4.11: Two simulations of degradation experiment with satellite cycling protocol. Both simulations with equal parameters, one with and the other without electron migration flux. a) Capacity and b) end of discharge voltage (EoDV) of simulation and experiment. From Bolay et al. [15].

model as multiplicative factors and hence are not identifiable. Those parameters are taken from literature. All parameters of the degradation model are given in Table B.4.

The determination of the optimal parameter set is a multi-objective optimization problem, where the capacity fading as well as the EoDV error have to be minimized. As the simulation of around 27,000 cycles is quite expensive in terms of computation time, a sophisticated optimization algorithm is inappropriate. For that reason, a fixed parameter space is used, where the parameters are uniformly distributed in a reasonable range. The cycling is then simulated for all combinations of parameters simultaneously on the computer cluster. Since the optimal parameters of the P2D model, which were determined with the surrogate optimization, also depend on the chosen degradation parameters, we optimized the P2D model parameters for each set of degradation parameters. When we simulate the degradation for a particular set of degradation parameters, we use the corresponding optimal parameters of the P2D model. Eventually, the optimal degradation parameter set of the fixed parameter space, which minimizes the capacity error and the EoDV error, is chosen.

In Fig. 4.11 a), the capacity fading over around 27,000 cycles is depicted. Fig. 4.11 b) shows the corresponding EoDV. At around 24,000 cycles, when the charge voltage is raised from 4.1 V to 4.2 V, the degradation accelerates. For the discussion of the simulation results, we first consider the red lines. In both graphs, we see that the degradation gets overrated at the beginning of the cycling. This can be explained by a not globally optimal choice of cell parameters. As we already described in sec. 4.3, the optimization of the parameters is a difficult task due to computation time and the identifiability of the parameters. After around 2,000 cycles, over a wide range of the cycling, the trend of the simulation corresponds quite well to that of the experiment, especially in the EoDV. At the end, after about 20,000 cycles, the simulation underrates the degradation of the experiment. At this late period of cycling, there are probably additional degradation processes taking place in the cell, that are not covered by the SEI growth model. This could be for example the cracking of anode particles as described in Ref. [83] or Li plating. These processes lead, among other things, to a sudden increase of anode surface, which accelerates the SEI growth. Furthermore, Mendoza-Hernandez et al. [63] observe indicators for plating in the satellite in-flight data. These occur more frequently at a later stage of the cycling. Plating is responsible for or accelerates a number of degradation processes. This may be another reason why accelerated aging is observed that cannot be explained by SEI growth.

We compare the models for SEI growth of von Kolzenberg et al. [48] and of Single et al. [94]. The difference between the extended model of von Kolzenberg et al. and the model of Single et al. is the additional consideration of the Li-ion flux through the SEI during charging. This causes the migration of electrons due to an electric potential drop in addition to diffusion. To discuss the influence of the electron migration flux on SEI growth, we perform simulations with $\omega = 0.5$, as established by von Kolzenberg et al., and with $\omega = 0$. When setting ω to zero, the term that describes the electron migration ($zF\kappa_{\mathrm{SEI}}^{\mathrm{e}^-}\nabla\Phi = 0$) in the equation for the SEI flux eq. (2.11) vanishes. The simulation result of the model without the migration rate is shown in Fig. 4.11 as yellow lines. It can be seen that the degradation decreases significantly in that case already after a few thousand cycles. Also, the trend of the simulation does not correspond to the experiments in both graphs. This leads to the conclusion, that the migration component is necessary to describe the degradation behavior reliably.

The parameterized degradation model in the P2D framework is used extensively in sec. 5 for diverse long-term simulations of the battery degradation.

4.4.2 3D Microstructure-resolved Simulations

The microstructure-resolved SEI growth is simulated in 3D with the same degradation parameters as determined before with the P2D model. The cell and degra-

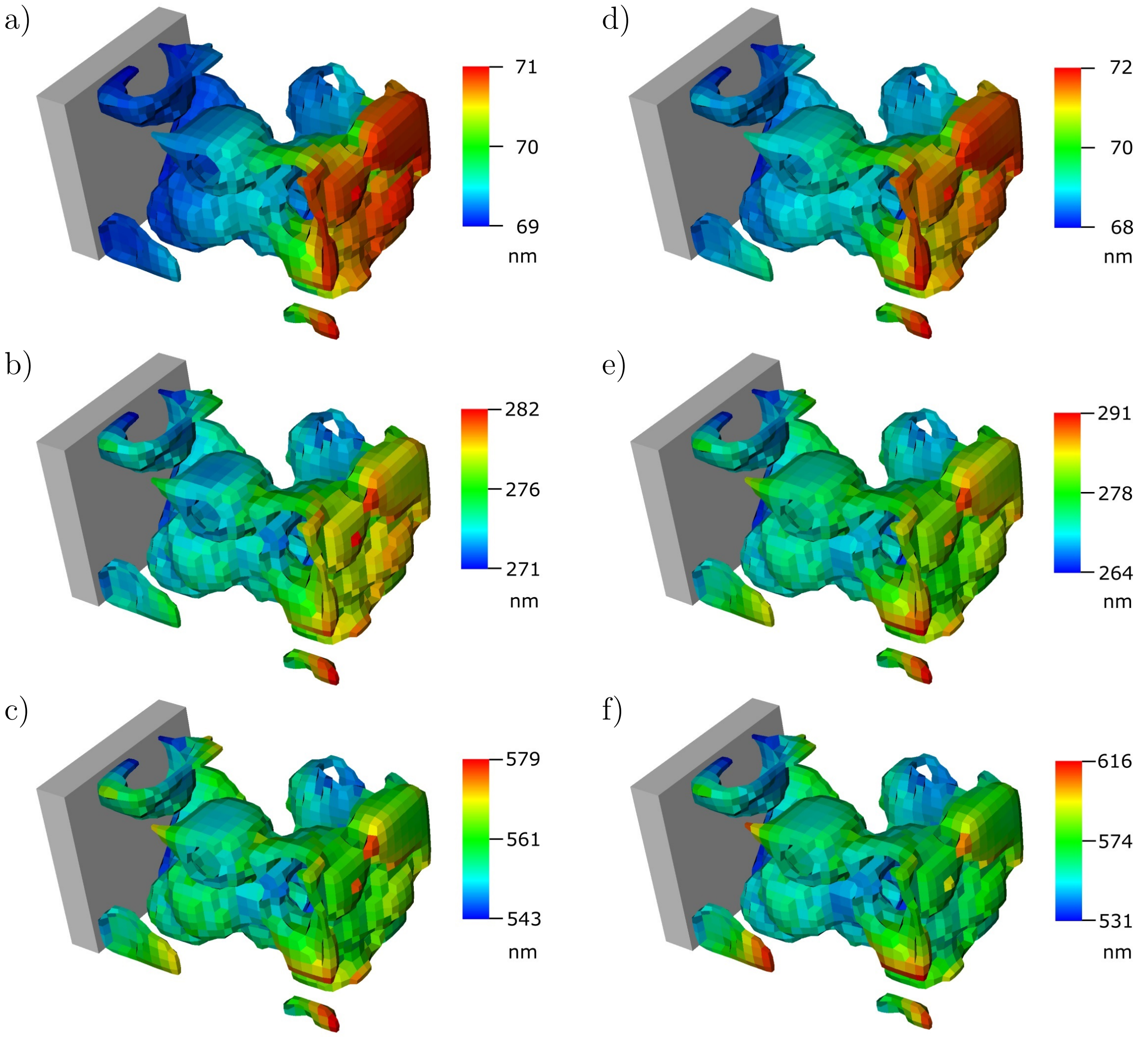

Figure 4.12: SEI thickness of anode particles connected to current collector for two cycling protocols at three time points. Left column (a, b, and c) shows cycling protocol P3, right column (d, e and f) shows P4 (cf. Table 4.2). a) and d) 8 cycles. b) and e) 136 cycles. c) and f) 672 cycles. From Bolay et al. [15].

Table 4.2: Cycling protocols used in 3D simulations.

Protocol	Charge (CC-CV)	Discharge (CC)	Temperature
P3 (3D)	1.5 A / 4.1 V 65 min	1.0 A 35 min	25°C
P4 (3D)	1.5 A / 4.1 V 65 min	2.0 A 35 min	25°C
P5 (3D)	3.0 A / 4.1 V 65 min	2.0 A 35 min	25°C

dation parameters for the 3D simulations can be found in Table B.3 and B.4. For the 3D simulations, we use three different cycling protocols. They differ in charge and discharge currents to investigate how the current influences the SEI growth behavior. The protocols (P3 - P5) can be found in Table 4.2. P3 is equivalent to the cycling protocol used with the P2D model (P2). In P4, the discharge current is doubled. This is based on the experiments in Ref. [19]. In P5, both the charge current and the discharge current are twice as large as in P3. The time intervals for charging and discharging are the same in all protocols and correspond to the typical satellite battery cycling protocols.

The 3D simulations reveal an inhomogeneous growth of the SEI. In Fig. 4.12, the results of the simulations with two different cycling protocols at three points in time are shown. We see anode particles connected to a current collector. The color represents the thickness of the SEI after a certain amount of cycles. In the left column, the cell is cycled with protocol P3, the right one is cycled with P4. Fig. 4.12 a) and d) show the SEI thickness after 8 cycles, Fig. 4.12 b) and e) after 136 cycles, and Fig. 4.12 c) and f) after 672 cycles.

For all states shown in Fig. 4.12, there are coexisting regions with a thicker SEI and regions with a thinner SEI. In Fig. 4.12 a) and d) we see that, at the beginning of the cycling, the particles near the separator have a thicker SEI than those near the current collector. Yet the difference is very small and comprises only a few nanometers. Fig. 4.12 b), c), e), and f) show that after several cycles, the inhomogeneity spreads over the whole anode. When comparing Fig. 4.12 b) and e) or Fig. 4.12 c) and f), we see that this happens sooner for the protocol with the higher discharge current.

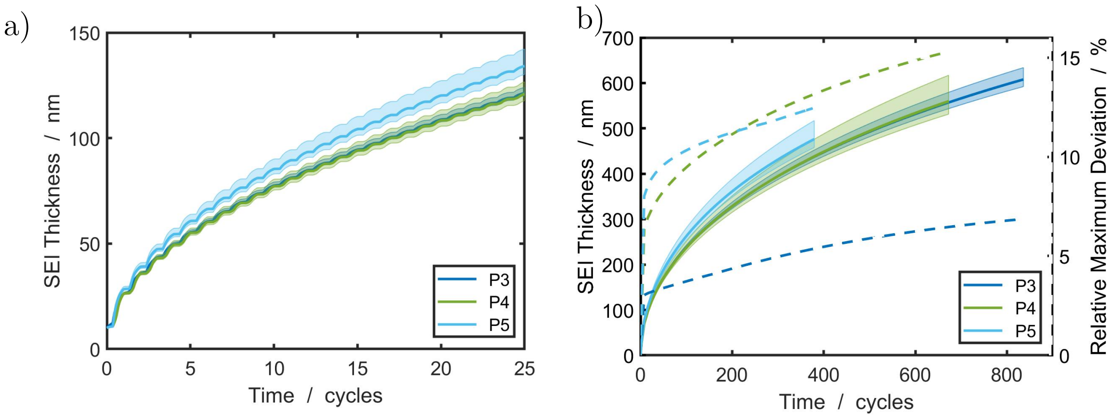

Figure 4.13: Variation of SEI thickness in 3D simulation for three different cycling protocols (cf. Table 4.2). a) Stepwise growth behavior in each cycle. b) SEI thickness and relative maximum deviation (dashed lines) over a long cycling period. From Bolay et al. [15].

After many cycles, there are particular domains of the anode, where the SEI is noticeably thicker. In Fig. 4.12 f), we observe that these are the thinner parts of the anode. Especially the peak-like structures, such as the one in the top left corner, have the thickest SEI.

The inhomogeneous growth is caused by the spatially varying SOCs through the anode and varying overpotentials at the anode SEI interface. This accelerates diffusion and thus SEI growth. At the beginning of the cycle, the SEI grows faster near the separator, as the Li-ions in the electrolyte reach this area first when the cell is charged. The SOC therefore increases there first. Only later do the Li-ions pass through the porous structure and reach the area near the current collector, causing the SOC to rise there too. After further cycling, the SEI is growing faster at the thinner parts of the particles since these reach higher SOCs faster when charging the cell. This is caused by the higher specific surface area at these thin structures.

For a quantitative analysis of the growth and variation of SEI thickness, its mean, minimum, and maximum, throughout the anode, at every computed time step, is depicted in Fig. 4.13. We investigate here the three cycling protocols P3 - P5 at a short period of 25 cycles, which corresponds to about two days, and a long period of 400 - 800 cycles, which corresponds to approximately 1 - 2 months.

When regarding the SEI thickness at the short period, as shown in Fig. 4.13 a), we observe a stepwise growth behavior. During charging of the cell or more precisely during lithiation of the anode, the SEI is growing faster than during delithiation.

These simulations reflect that the growth rate depends on the current density, which has been observed experimentally in Ref. [5].

Furthermore, when comparing the cycling protocols in Fig. 4.13 a), we note differences in SEI thickness and its inhomogeneity. This becomes even clearer in the longer period in Fig. 4.13 b). The differences in the total length of the cycling simulations are due to numerical instabilities, when using higher currents. When comparing the mean SEI thickness of the different protocols, we observe that for P3 and P4, which differ in the discharge current, there is no significant difference in the thickness. In contrast, the SEI is growing faster for P5, which has a higher charge current than the other two protocols. This is also in accordance with the growth behavior observed in Ref. [5] and rationalized in Ref. [48].

The relative maximum deviation, i.e. the difference between minimum and maximum divided by the mean of the thickness, is shown as dashed lines in Fig. 4.13 b). The simulations with doubled discharging currents (P4 and P5) show a significantly larger deviation, i.e. a more inhomogeneous SEI growth. We also see that the deviation is already remarkable for the first few cycles and increases only slightly thereafter. One reason for this could be that the SEI is very thin at the beginning, which makes small differences more significant.

This analysis shows that the combination of the degradation model with the 3D model is a useful tool to get a theoretical insight into the SEI growth behavior of Li-ion cells under varying cycling conditions.

The inhomogeneous SEI growth can also be observed in the P2D framework. There, the deviation only concerns the position in the anode. This is the distance from the separator and the current collector. Several examples of the long-term SEI growth and its inhomogeneity can be observed in sec. 5.

5 State Estimation of Satellite Batteries

In battery applications and especially when they are used in aerospace applications, it is essential to be able to predict the battery behavior and to estimate the states of the battery. The states that are of major importance are the state of charge (SOC) and the state of health (SOH). These states are hidden states of a dynamical system. That means they can not be directly measured while the battery is in use. Especially in aerospace applications, the availability of information about the battery is very limited. To conclude from the measurable quantities of a dynamical system to the hidden states bears several difficulties. It is not possible to prove the accuracy of the estimated states. Also, the measurements contain errors. Furthermore, every model that describes physical processes of the real world is only an approximation and can be too simple or miss processes that influence the measurable quantities. There are sophisticated algorithms for the state estimation of dynamical systems using physics-based models, which account for the uncertainties both in the measurements and in the models. Among the commonly used are Kalman filters and their variants. These were already often used for the state estimation of Li-ion batteries. Other possible algorithms for the state estimation are other filters, like the particle filter or the H-infinity filter, or state observers like the sliding-mode observer or the Luenberger observer [47, 52, 53].

Plett was one of the first to use Kalman filters for the state estimation of Li-ion batteries [72, 75]. In a series of papers, he applies different kinds of Kalman filters like the extended Kalman filter (EKF) or the sigma point Kalman filter in combination with an equivalent circuit model (ECM) to estimate the SOC. Also, he describes a dual filter to additionally estimate parameters of the model which account for the aging of the cell [74].

There are various battery models employed for the SOC estimation. The ECM is a commonly used model, especially in battery management systems (BMS) of micro controllers, as they are computationally advantageous and easy to apply. They are also often used in combination with filters as in Refs. [56, 3, 106, 115, 21, 111]. However, ECMs are only usable in a narrow range in which they are parameterized and give little insight into the actual physical processes in the battery. To that end, physics-based models like the pseudo-2D (P2D) model or the single particle model (SPM) are more suitable to get a better understanding of the battery, although they are computationally more expensive. Bizeray et al. [14] were one of the first to use the P2D model combined with an EKF, which they modify based on [9] to employ the filter on the differential algebraic equations (DAE) of the model. Due to their accurate prediction of cell behavior, these models are also widely used in combination with Kalman filters [106, 80, 101, 114, 102, 11, 55].

To account for the degradation of the cell and to be able to estimate the SOH, there are different approaches depending on the cell model in use. First, it is important to define which variable or parameter describes the SOH. Usually, the remaining capacity of the cell is appropriate. For some applications, the power fade or cell resistance are of primary interest. In the case of the ECM, the SOH can be derived from the model parameters, which can then be adapted to model the degradation of the cell [74]. In the case of physics-based models, there are different approaches. Some use empirical models for the SOH evolution or determine the cell model parameters for various aging conditions of the cell [80, 95]. To gain a better understanding of the processes that occur during aging and to make reliable predictions, it is useful to physically model SOH evolution as well [114, 11, 15].

Often only the SOC is estimated. In these cases, the reliability of the model decreases over time as the cell degrades and the model parameters no longer match the condition of the cell. Sometimes the SOH is the only state that is estimated [11].

If both states, the SOC and SOH, get estimated, combinations of filters are required. But already for the choice of the filter for one of the states, there are several possibilities. The original Kalman filter is only suitable for linear problems. In the nonlinear case, there are variants like the EKF and the unscented Kalman filter. Also, the particle filter is often used in this setting. In Refs. [75, 52, 106, 47, 21], the different filters are compared. The combined estimation of SOC and SOH is not trivial since these states evolve on different timescales. Hence, there are various approaches for the combination. One simple approach is to use the ECM with a joint or dual filter [74, 76, 3, 21, 110]. Here, the states and the parameters get estimated in every time step either by combining them to one comprehensive state vector or by using two filters, which update mutually in each step. This approach ignores the fact that the SOH is evolving much slower than the SOC.

Thus, more sophisticated algorithms use multi-timescale approaches. In Ref. [41], Hu et al. developed a multiscale framework, where SOC and capacity estimation are decoupled and compared it to a dual EKF. Their battery model is based on Coulomb counting. Zou et al. use a multi-timescale approach, where they generate a map for various SOC and input conditions, which can then be used online for state estimation [114].

The data to validate the state estimation approaches can be synthetic or real data. The advantage of synthetic data is, that the states, which are hidden in real applications, are known here. With this it is possible to prove that the algorithm is able to find the right values [80, 14, 101, 114, 102, 95]. To check the applicability of the algorithm, it is also necessary to validate it with real battery data [72, 75, 41, 3, 55, 6]. Usually, these are gained experimentally. Only few use field data [56]. Often the application field is EVs. There are also a few publications, which consider aerospace applications [45, 80, 6].

Another possibility to predict the performance and degradation of Li-ion batteries are machine learning approaches. These are used a lot in literature to estimate the battery states [90, 113, 2, 103, 57, 54]. For our work, we choose the approach of combining physics-based models with Kalman filters as this allows to gain a deeper understanding of the processes in the battery and to associate the estimated states with physical variables in the cells.

Here, we design a novel algorithm to estimate the SOC and SOH of a Li-ion battery. The algorithm uses two extended Kalman filters for the states. It is based on the full cell model described and parameterized in sec. 4. In this model, the SOC and SOH evolution are coupled and calculated simultaneously. Since these states evolve on different timescales, the algorithm needs to filter the states separately while taking into account that they are coupled by the model. Therefore, we design a multi-timescale algorithm where the filter for the SOC is nested in the filter for the SOH.

We test our filter with synthetic data, which are generated with the battery degradation model, based on a satellite cycling protocol. Subsequently, we validate the algorithm with the real in-flight data of satellite REIMEI. These data are particularly appropriate to test the applicability of the algorithm to real-world problems. They span a very long period, which is essential for reliable aging prediction. To the best of our knowledge, this is the longest data period with which a state estimation algorithm was tested. Furthermore, the data is noisy and incomplete, which gives insight into how the filter behaves under imperfect conditions.

The algorithm can be used in different ways. Applied to a measured data set, it can make the degradation of the cell more comprehensible. Additionally, when continuing the simulation, the further aging can be predicted. The algorithm can also be used to filter the battery cycling in real-time. The model might be too computationally intensive for online filtering. However, the satellite application has the advantage that the batteries can be controlled remotely. Another application for the algorithm is the validation of the accuracy of the degradation model.

In this chapter, we first summarize the theory of the Kalman filter and its variants. Subsequently, we describe our multi-timescale algorithm and explain how it is used to estimate the states of a battery. The functionality of the filter is demonstrated with synthetic and in-flight data. Finally, we will use the filter to validate different models and show how the filter can be used to gain further insight into the accuracy of the chosen model.

5.1 Filter Theory

This section summarizes the theory of Kalman filters. Since the Kalman filter can only be used for linear models and our battery model is nonlinear, we also describe a variant called extended Kalman filter and explain how it is used for differential algebraic equations.

5.1.1 State-Space Models and Dynamical Systems

A physical system is described by the inner states of the system that propagate in time, which is governed by differential equations. The system can be represented by a state-space model. This makes it easier to handle it in a mathematical framework. The representation for linear models is given as

$$\dot{x} = Ax + Bu \tag{5.1}$$

$$y = Cx \tag{5.2}$$

and for nonlinear models

$$\dot{x} = f(x, u) \tag{5.3}$$

$$y = h(x) \tag{5.4}$$

with the time dependent state vector x, the input vector u, and the output vector y. In the linear case, A is the system matrix, B is the input matrix, and C is the output matrix. In the nonlinear case, f and h are arbitrary functions [93].

5.1.2 Kalman Filter

The Kalman filter (KF) is a mathematical method to estimate the states of a dynamical system, which can be described by a stochastic linear state-space model. Sometimes, the inner states of a system can not be measured. The KF improves the estimate of these unknown states by using observable measures of the system. Also, it accounts for process noise and observation noise.

Under the assumption that the errors are normally distributed, it can be shown that the Kalman filter is an optimal estimator for linear problems [93].

The discretized stochastic state-space model is given as

$$x_{k+1} = A_k x_k + B_k u_k + w_k \tag{5.5}$$

$$y_k = C_k x_k + v_k \tag{5.6}$$

with the process noise w_k and measurement noise v_k. These noises are assumed to be normally distributed with $w_k \sim \mathcal{N}(0, Q)$ and $v_k \sim \mathcal{N}(0, R)$, where Q and R are the corresponding covariance matrices [93, 72, 14].

The Kalman filter describes how the mean $\hat{x}$ and covariance P of the state evolve in time. Therefore, the filtering process starts with estimates of mean and covariance for $k = 0$. These are obtained with the statistical expectation, where

$$\hat{x}_0 = \mathbb{E}[x_0] \tag{5.7}$$

$$P_0 = \mathbb{E}[(x_0 - \hat{x}_0)(x_0 - \hat{x}_0)^T]. \tag{5.8}$$

The Kalman filter steps are given as follows. First, the state and covariance are updated in time to get the a priori estimates $\hat{x}_k^-$ and P_k^-

$$\hat{x}_k^- = A_k \hat{x}_{k-1}^+ + B_k u_k \tag{5.9}$$
$$P_k^- = A_k P_{k-1}^+ A_k^T + Q \tag{5.10}$$

and the estimated output $\hat{y}_k$ is computed from the a priori state estimate

$$\hat{y}_k = C_k \hat{x}_k^- . \tag{5.11}$$

Then, the a posteriori estimates $\hat{x}_k^+$ and P_k^+ are computed with the Kalman gain K_k using the actual measurement y_k

$$K_k = P_k^- C_k^T (C_k P_k^- C_k^T + R)^{-1} \tag{5.12}$$
$$\hat{x}_k^+ = \hat{x}_k^- + K_k (y_k - \hat{y}_k) \tag{5.13}$$
$$P_k^+ = (I - K_k C_k) P_k^- . \tag{5.14}$$

Extended Kalman Filter

The major drawback of the Kalman filter is that it is only applicable to linear problems. Yet, most problems are nonlinear as linear systems barely exist in reality. For the filtering of nonlinear models, several variations of the Kalman filter exist, one of which is the Extended Kalman filter (EKF). The approach of the EKF is to linearize the system at each time step so that the Kalman filter can be applied [93, 72].

The discretized nonlinear state-space model is given as

$$x_{k+1} = f(x_k, u_k) + w_k \tag{5.15}$$
$$y_k = h(x_k) + v_k . \tag{5.16}$$

The partial derivatives of the nonlinear model are computed as

$$A_k = \left. \frac{\partial f(x_k, u_k)}{\partial x_k} \right|_{x_k = \hat{x}_k^+} \qquad C_k = \left. \frac{\partial h(x_k)}{\partial x_k} \right|_{x_k = \hat{x}_k^-} \tag{5.17}$$

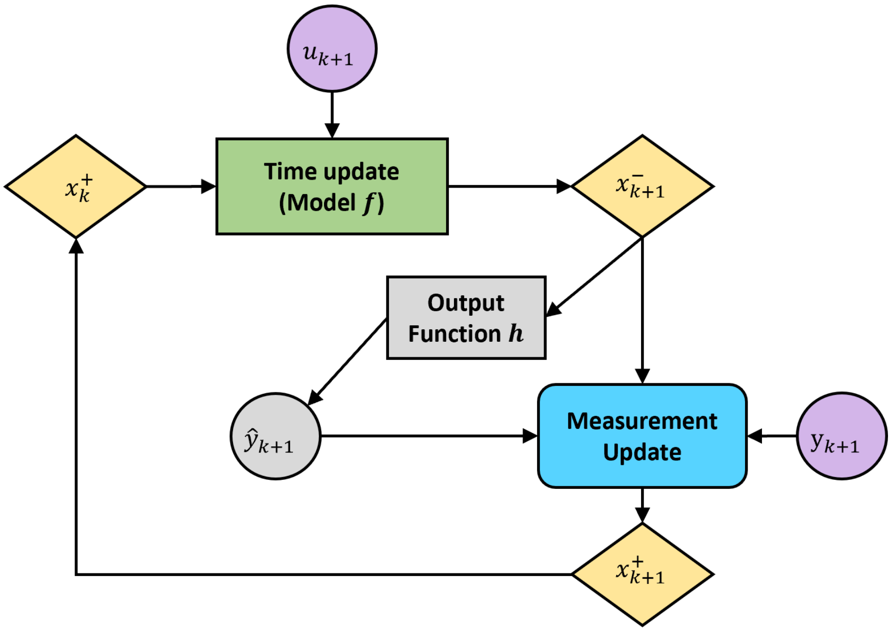

Figure 5.1: Flowchart of (extended) Kalman filter.

The a priori state estimate is now obtained by the nonlinear model with

$$\hat{x}_k^- = f(\hat{x}_{k-1}^+, u_{k-1}). \tag{5.18}$$

The subsequent steps are analogous to the Kalman filter algorithm for the linear case decribed in eqs. (5.10) to (5.14) using the derivatives of the model stated in eq. (5.17). The procedure of the EKF for every time step t_k is illustrated by the flowchart in Fig. 5.1.

Extended Kalman Filter for Differential Algebraic Equations

In the case, where differential-algebraic equations describe the nonlinear model, the EKF gets more complex. In Ref. [9], Beccera et al. describe how the filter is modified to take the algebraic equations into account. Bizeray et al. describe in Ref. [14] how this version of the EKF is used for a battery model. We summarize the procedure here. A detailed explanation of the modification steps can be found in Ref. [9, 14].

The state-space representation of a DAE system is given as

$$\dot{x}^d = g(x^d, x^a, u) \tag{5.19}$$

$$0 = \gamma(x^d, x^a) \tag{5.20}$$

with the differential equations in (5.19) and the algebraic equation in (5.20). The state vector x is split up in the differential state vector x^d and the algebraic state vector x^a. Again, the nonlinear functions g and γ need to be linearized. By rearrangements, the algebraic terms can be expressed by the differential state vector. This way, the system can be transformed into a stochastic linear state-space model

$$\dot{x}^d = \mathcal{A}x(t) + \mathcal{B}u(t) + w(t) \tag{5.21}$$

with the linearised matrices $\mathcal{A}$ and $\mathcal{B}$.

By integrating eq. (5.21) as described in [9, 14] the state matrix $A_k = e^{\mathcal{A}_k T}$ is obtained, where T is the sampling period. With this, the EKF can be applied as described in sec. 5.1.2.

5.2 Estimation of Battery States on Different Timescales

For the filtering of states evolving on different timescales, an algorithm is needed that filters the states separately, while considering the nested nature of the models to determine the states and their interdependence. Therefore, we develop a novel algorithm, where the filter for SOC estimation is nested in the filter for SOH estimation.

5.2.1 Multi-Timescale Algorithm with Nested Filters

In this section, our algorithm is explained for a general system with states that evolve on different timescales. The application of the algorithm to battery data is described in sec. 5.2.2.

When considering a complex system with processes evolving on different time scales, the corresponding states must be filtered separately. Otherwise, the state,

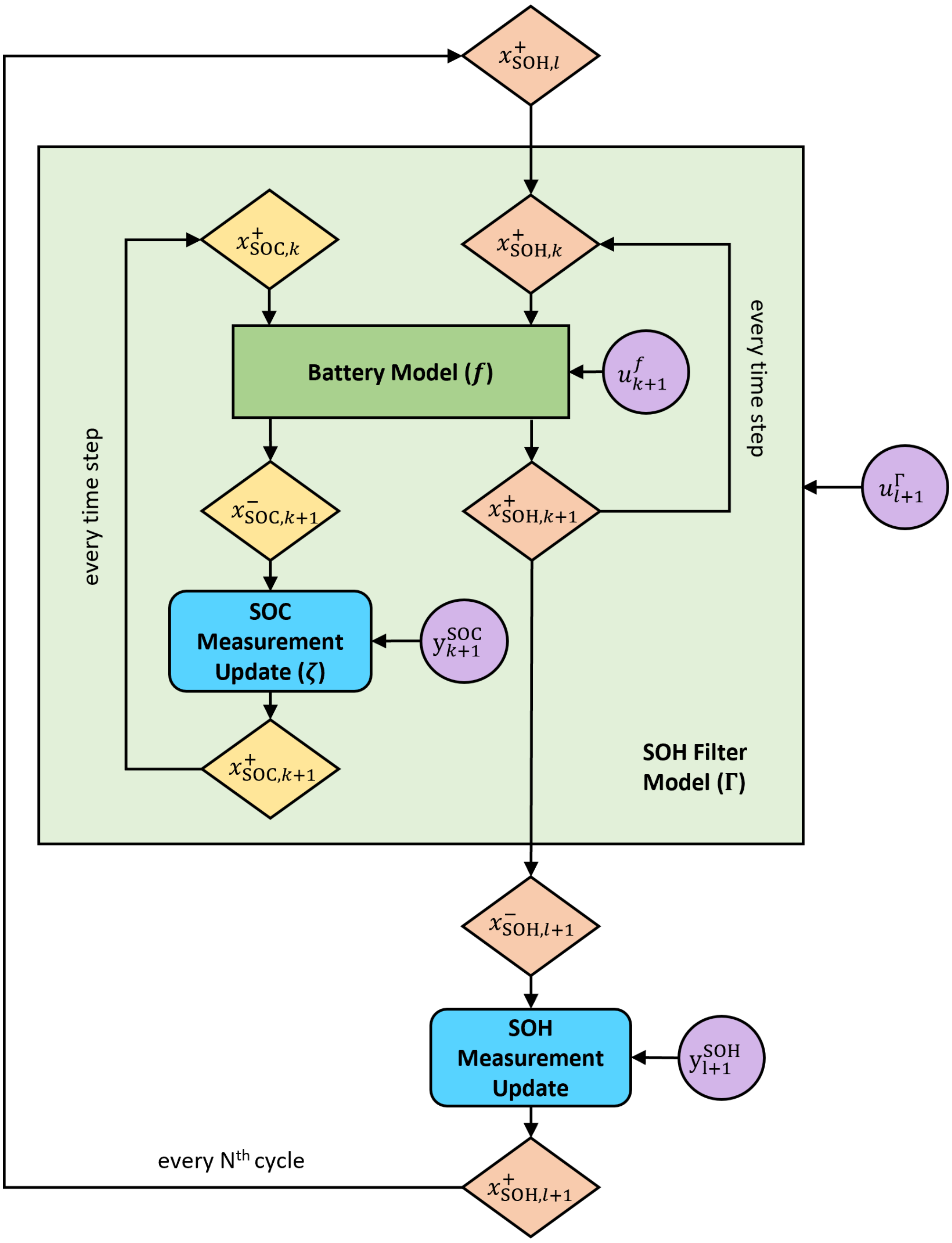

Figure 5.2: Flowchart of multi-timescale algorithm applied to battery states.

which is evolving slowly in time, will be corrected too much. For this reason, we developed a nested multi-timescale (MTS) filter algorithm that combines two EKFs, where the filter for the fast evolving state is nested in the filter for the slow one.

If we describe the measurement update of the fast state by a function ζ, with $\zeta(x_k^-) = x_k^+$, we can combine the time update of the fast state, which is expressed by the function f, and the measurement update to $\zeta \circ f$. With this, we define an operator

$$\Gamma_{\tau(l)} = (\zeta \circ f)^{\tau(l)} \tag{5.22}$$

that calculates $\tau(l)$ iterations of this operation, so that $\Gamma_{\tau(l)}(x_{l-1}^+) = x_l^-$. This is the model that is used for the outer filter. The function τ is a function that describes the necessary number of time steps t_k to get from one defined point of time t_l, where the slow state gets filtered, to the next one t_{l+1}. The index k counts the filter steps of the fast state, while l counts those of the slow state. To use the model for the EKF, this model needs to be linearized corresponding to eq. (5.17). The Jacobian of the outer model is approximated numerically with

$$\frac{\partial \Gamma_{\tau(l+1)}(x_l)}{\partial x_{i,l}} = \frac{\Gamma_{\tau(l+1)}(x_l) - \Gamma_{\tau(l)}(x_{l-1})}{x_{i,l} - x_{i,l-1}} \tag{5.23}$$

where $x_{i,l}$ are the components of the state vector at time t_l. This way, the EKF can be applied as described in sec. 5.1.2.

The scheme for the MTS filter algorithm and its application to battery states is depicted in Fig. 5.2 as a flowchart. It will be further described in the next section.

5.2.2 Application of the MTS Algorithm to Battery Data

The MTS algorithm can be applied to estimate the SOC and the SOH of batteries. The SOC is a fast evolving state as it can cover its whole value range during a single cycle. The SOH evolves slowly in time throughout the lifetime of the battery.

The model for the battery behavior and degradation has been described in sec. 2. This model is used in the inner loop of the nested algorithm to compute the time update of the states in every time step.

It is necessary that the filtering runs fast, since it should be usable in real time and needs to simulate several thousand cycles for the test procedures. To that end, we chose a coarse discretization for the P2D model. We described the discretization in sec. 4.1. Here, the anode is discretized with three nodes, the cathode with four, and the particles with three discretization points. This results in a state vector $x^d = (x_{\mathrm{SOC}}, x_{\mathrm{SOH}})$ with 21 entries for the SOC and three for the SOH. The dimensions of the state covariance matrices P^{SOC} and P^{SOH} and the noise covariance matrices Q^{SOC} and Q^{SOH} of the filters are chosen accordingly.

Definition of SOC and SOH. Before describing how the algorithm is used to estimate the battery states, we give a definition of SOC and SOH. For both, there exists no universal definition in literature. Instead, the definition also depends on the use case. We use the variables of our model to define the states. From this general form, they can be transformed according to specific requirements.

The state of charge (SOC) is given for every discretization point in the electrodes as the ratio of the Li concentration in the solid and the maximum Li concentration of the respective electrode:

$$\mathrm{SOC} = \frac{c_{\mathrm{s}}}{c_{\mathrm{s,max}}} \cdot 100\%.$$

The state of health (SOH) shall give information about the remaining lifetime of the battery. It is often defined as the remaining capacity of the cell. In this application, the satellite mission requires a minimum voltage to operate the loads. The EoDV is therefore one feature of the SOH of the satellite cells. Since we describe the degradation of the cell by the growth of the SEI, we define this variable as a further feature of the SOH. The capacity of the cell can be directly related to the SEI thickness, since SEI growth consumes Li-ions that can no longer be cycled. In this way, one can directly convert the thickness of the SEI into irreversible capacity loss, as described in eq. (2.9). However, the measured cell capacity is not only determined by the remaining Li-ions but also by the internal resistance of the cell, which also depends on the thickness of the SEI.

We do not have any capacity measurements in our data, so we will not give the cell capacity based on our simulations but only the thickness of the SEI. If this algorithm is applied to data that also contains capacity measurements, it is easy to simulate these measurements and thereby obtain a value for the remaining capacity.

Filter Parameters. The parameters of the filters are the measurement covariance matrix R, the process covariance matrix Q, and the initial covariance matrix of the states P_0. These exist for the SOC filter and for the SOH filter respectively.

Here, our measurements are the cell current and voltage. These values are one-dimensional, which is why R is a scalar. The parameter can be determined from the distribution of the measurements. Assuming that the measurements are normally distributed, the standard deviation can be determined in the sections where the values are constant. This applies to the voltage during charging and to the current during discharging. For the in-flight data of the satellite batteries, we obtain the standard deviations $\sigma_I = 0.08$ A and $\sigma_V = 0.005$ V. From these, we get the variances $R_I = \sigma_I^2 = 6.4 \cdot 10^{-3}$ and $R_V = \sigma_V^2 = 2.5 \cdot 10^{-5}$.

The process covariance matrix Q is used in eq. (5.10) to calculate the time update of the state covariance matrix. It can be chosen to prevent this matrix from getting too small. The process and measurement covariance matrices can be used to control the stability and convergence of the filter [9, 41].

The covariance matrix P represents the uncertainty of the states. There are several ways to determine the initial matrix P_0. It can be estimated from samples of the initial state estimate according to eq. (5.8). A simpler method is to initialize P_0 with a matrix where all entries are identical. The size of the entries represents the uncertainty at the beginning [9, 14, 72].

All covariance matrices need to be determined for both the SOC filter and the SOH filter. We determine them by studying their influence on the filtering behavior as described in sec. 5.2.4.

Filtering SOC and SOH with the MTS Algorithm

With this, the MTS algorithm can be applied to filter the battery states. Several aspects must be considered when filtering the SOC and the SOH. The details will be described in the following.

The SOC is basically filtered in every time step that is available from the data. This is depicted by the left inner loop in Fig. 5.2, where the time update is calculated with the battery model f and the measurement update with the filter function ζ.

However, the SOC is only filtered during charging or discharging. The measurement uncertainty influences, among others, the evolution of the state covariance matrix. Since the measurement uncertainty corresponds to the measurement error of the current during charging and to that of the voltage during discharging, the evolution of the state covariance matrix is too strongly influenced by this switching if filtering is done continuously.

Both, filtering during charge and filtering during discharge is possible. We decided to filter the SOC only during charge with the current as corresponding measurement, since the voltage is already used for the SOH filtering with the EoDV. This results in the measurement covariance matrices being $R^{\mathrm{SOC}} = R_I$ and $R^{\mathrm{SOH}} = R_V$. It is also possible to filter the SOC during charge and during discharge. To that end, the filter would require two independent covariance matrices of the SOC. Here, this is not necessary, as the filter provides sufficiently good results when filtering only during charging or during discharging.

So, at time step k, the input for the battery model f is the constant cell voltage of the cycling protocol $u_k^f = V_k$ and the output, which is used for the measurement update of the SOC filter, is the measured cell current $y_k^{\mathrm{SOC}} = I_k$. The SOH is also updated in time by the battery model f at every time step, as is depicted by the right inner loop in Fig. 5.2, but not filtered.

For the SOC filtering, it turned out to be unstable to start the filter at the beginning of the simulation. So, for a robust filtering of battery cycling, it is recommendable to let the SOC simulation stabilize for the first few cycles. We have found it to be sufficient if the first three to four cycles are simulated before starting the filtering of the SOC. In Fig. 5.14 a) on the left-hand side, one can see that the filter starts in the fourth cycle.

Further, the filter gets unstable, when the constant current is switched from one value to another. Therefore, filtering is suspended during switching. However, this is only relevant for filtering during discharge. Another case in which the filter becomes unstable is when the cells get charged with a higher constant voltage. In the data under consideration, this is only the case within short time intervals. Thus, filtering can also be suspended here to make it perform more stably.

The SOH is filtered periodically after every Nth cycles at the time steps t_l. In Fig. 5.2, this is the outer loop. The light green box represents the time update model Γ used in the SOH filter, cf. eq. (5.22). The input for this model is the constant current of the cycling protocol $u_l^\Gamma = I_l$. The output is the measured EoDV $y_l^{\mathrm{SOH}} = V_l$.

Since the measurement points have a mean distance of 32 seconds and one cycle has an approximate duration of 100 minutes, the SOH filter time steps t_l comprises around $N \cdot 185$ time steps t_k. The exact determination of the filtering points, which correspond to the function τ in eq. (5.22), differs for the synthetic data and the in-flight data. The SOH is always filtered at the end of discharge, since this is the point at which the EoDV is measured. For the synthetic data, which is in perfect regularity, without gaps, it is always possible to filter after N cycles. However, for the in-flight data, the Nth cycle may coincide with a data gap, where no measurements are available for the cycles. In this case, the filter point of time is shifted to the next cycle block, where measurement points are available.

The numerical calculation of the Jacobian of the function Γ for each time step t_l comprises the evaluation of $\Gamma_{\tau(l)}$ for every component of the SOH state vector, cf. eq. (5.23). Here, this means that it is evaluated three times. This is a further reason to choose a coarse discretization.

To determine the frequency of the SOH filter, there are several aspects to consider. On the one hand, it is not possible to filter more frequently than once per cycle, since the EoDV is the determining factor. Also, since the SOH evolves slowly in time, it does not make sense to filter too frequently. Considering that in a space application the state estimation may be performed remotely, the contact to the satellite is also relevant. If we assume that the satellite is operated once per day, this corresponds to 15 cycles. Thus, it may make sense to choose the frequency in this order of magnitude.

The frequency of SOH filtering can be treated as an additional filter parameter. The influence of the frequency on the filtering behavior will also be studied in sec. 5.2.4.

5.2.3 State Estimation with Synthetic Data

Filters are generally used to estimate states of a system that can not be measured. When developing a new algorithm to estimate hidden states, the procedure has to be tested to make sure that it is able to find the actual true values. This can not be ensured with real data. Instead, the algorithm must be tested with synthetic data that behave like the real data for which the algorithm is to be used, but where the true states are known at the same time. Therefore, we generate synthetic data, based on our degradation model and use these to develop and test the MTS algorithm.

Using synthetic data to develop and evaluate state estimation algorithms is a common procedure [80, 14, 101]. But only some additionally validate the algorithm with real data [41, 53].

We have also described the generation of synthetic data in Ref. [15] and give it again here.

Generation of Synthetic Data

We generate the synthetic data by simulating a typical LEO cycling with degradation. To reproduce the uncertainty in the measured data, we add noise to the corresponding quantities of the simulation. These synthetic data imitate the satellites in-flight data with the crucial difference that both the inner states as well as the model including its parameters are known.

The cycling protocol used to simulate the synthetic data is based on the laboratory cycling tests of Uno et al. in Ref. [105]. At a temperature of 25 °C, the cells get discharged with a constant current of 1.0 A (C/3) for 35 minutes and get charged with a constant current-constant voltage profile with 1.5 A (C/2) to 4.1 V for 65 minutes. The parameters of the model can be found in the tables in sec. B. We simulated several thousand cycles with this cycling protocol. The data points are equidistant with a distance of 32 seconds.

The output of the simulation is either current or voltage. To these, we add white noise corresponding to the distribution of the measured in-flight data. We assume a normal distribution with zero mean. For the voltage we determined a standard deviation of 0.005 V and for the current it is 0.08 A.

The synthetic data are depicted in Fig. 5.3. a) and b) show the simulated exact and noisy cell voltage and current. The true simulated states, which are the SOC of anode and cathode and the SEI thickness, are depicted in c).

5.2.4 Calibration of Algorithm

To calibrate the algorithm, we perform multiple tests under various conditions. The tests are conducted with synthetic and in-flight data. The advantage of the synthetic data is, that we can prove if the algorithm actually estimates the true values, before checking whether the filter also works reliably with real data.

The calibration of the algorithm is done in two steps. On the one hand, the influence of the initial states on the filtering behavior needs to be investigated. On the other, the filter parameters must be tuned to ensure that the algorithm is robust, that it minimizes the errors or converges fast, and that the calculated states are physically appropriate. Accuracy, robustness, and convergence of an SOC filter are investigated by Li et al. [52]. In Ref. [64], Mößle et al. also investigated the filter parameters of a Kalman filter for the estimation of the

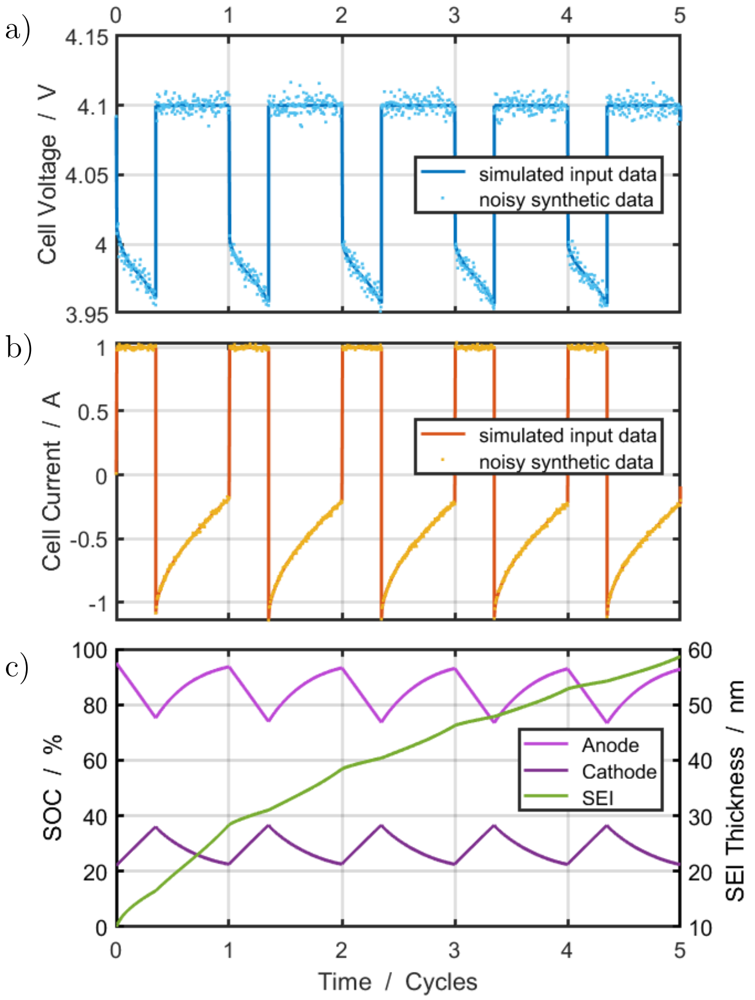

Figure 5.3: Synthetic data generated with battery degradation model based on LEO cycling profile. 5 cycles with true simulated data and added white noise. a) Cell voltage. b) Cell current. c) SOC and SEI thickness.

battery SOC based on an ECM. They developed an algorithm which tunes the filter parameters automatically regarding these requirements.

Our calibrated algorithm can be used to estimate the SOC and SOH and to investigate the filtering behavior for various models.

Investigation of Initial States

Kalman filters are used to find the true states from initial estimates. So it is not necessary to know the initial true state. Independently from the chosen initial

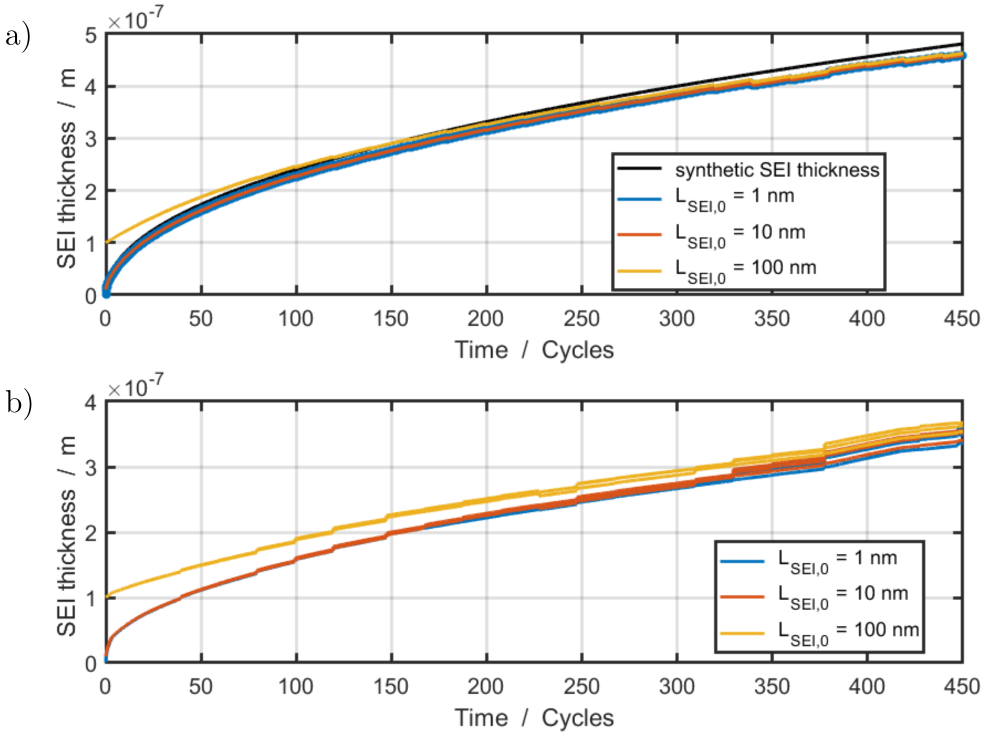

Figure 5.4: SEI growth behavior dependent on different initial values. a) In-flight data. b) Synthetic data.

state, the filter should come to the same result after several time steps. Yet, the filter might find a local minimum or it might be unstable under certain starting conditions. To that end, we investigate the filter behavior for a test set of several start values.

We test $\mathrm{SOC}_{\mathrm{anode},0}$ for the values $\{80, 85, 90, 95\}$ %, $\mathrm{SOC}_{\mathrm{cathode},0}$ for the values $\{15, 20, 25, 30\}$ %, and for $L_{\mathrm{SEI},0}$ we test $\{1, 10, 100\}$ nm. This yields a test set of 48 starting conditions. This test set is used for the synthetic as well as for the in-flight data. For the synthetic data, the true initial states are known. These are $\mathrm{SOC}_{\mathrm{anode},0} = 95$ %, $\mathrm{SOC}_{\mathrm{cathode},0} = 22$ %, and $L_{\mathrm{SEI},0} = 10$ nm.

In Fig. 5.4, we compare the SEI growth behavior for synthetic (a) and in-flight (b) data, depending on different initial values. In the figure we show the curves for an initial anode SOC of 80 % and an initial cathode SOC of 15 %. The results for other initial SOC values are almost identical. In both data cases, the curves deviate at the beginning, but converge after a few hundred cycles. From this we can already conclude that the initial SEI thickness has no substantial influence on the filter behavior when varied in the tested range.

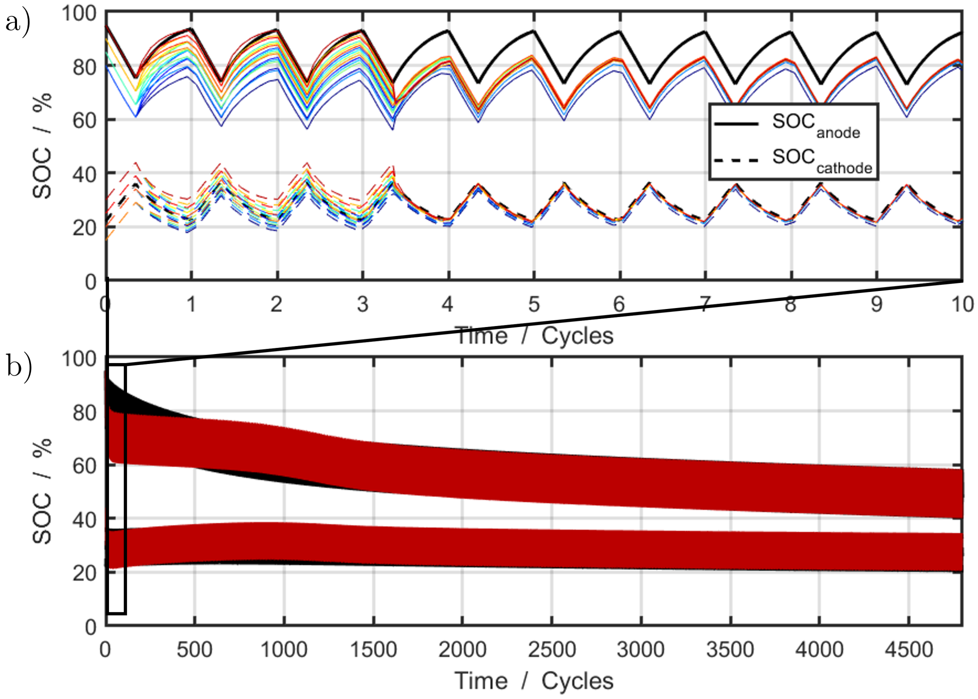

Figure 5.5: SOC trend of filtered synthetic data for different initial states. True SOC is shown in black. Filtered curves for 16 different start values are shown in color. a) First ten cycles. b) Whole period.

In Fig. 5.5, the results of the SOC behavior for the synthetic data can be seen. We only show the results for $L_{\mathrm{SEI},0} = 1$ nm and the 16 combinations of initial SOCs. For the different SOCs, we see in Fig. 5.5 a) that in the first three cycles the variance of the curves increases. After the filter sets in in the fourth cycle, the variance of the curves decreases and they converge to the same curve, which is, what we expect from the filter. In 5.5 b) the trend of the SOCs is depicted for the whole cycling period, where the upper bar represents the SOC range for the anode and the lower bar represents that for the cathode. After a few hundred cycles, the states converge to the true values.

The same test as for the synthetic data was performed on the in-flight data. Again, as the initial SEI thickness has no influence on the filtering, the results for the 16 combinations of initial SOCs are compared. These are shown in Fig. 5.6. As can be seen, in this case not all starting conditions lead to the same result. There are two ranges to which the SOCs converge, when the filter sets in in the fourth cycle. In Fig. 5.6 a) we see that the curves drift apart very quickly. In one case both the SOC of the anode and that of the cathode are corrected by the filter to low values.

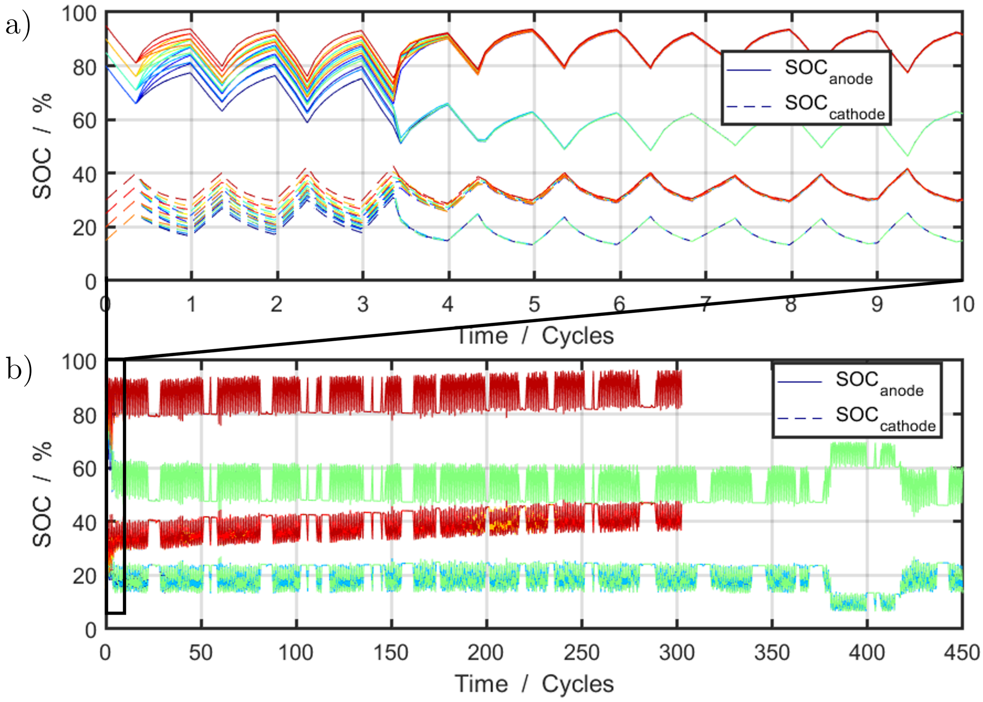

Figure 5.6: SOC trend of filtered in-flight data for different initial states. Filtered curves for 16 different start values are shown in color. a) First 10 cycles. b) First 450 cycles.

This occurs for the initial SOC pairs $\{(80,15),(80,20),(85,15),(85,20),(90,15)\}$. For the remaining 11 pairs the SOCs stay in the range from before the filtering starts and increase slowly. They continue to rise until the simulation aborts after about 300 cycles, as can be seen in Fig. 5.6 b). Therefore, the initial SOCs have to be chosen in the range of the stated pairs, where the SOCs are corrected to low values, when in-flight data are filtered.

Tuning of Filter Parameters

There are several filter parameters that can be tuned to improve the filtering. The criteria for the parameter choice are that they reduce the error of the measurable quantities and, in case of the synthetic data, the error of the states. Also, the filter should run stably and the estimated states should be physically reasonable. With inappropriate parameters, it could occur, for example, that the filter corrects the states too much, so that the SOC takes on values above 100 % or that the SEI thickness gets negative.

The parameters that can be adapted to control the filtering behavior are the measurement covariance matrix R, the process covariance matrix Q, the initial covariance matrix of the states P_0, and the frequency N of SOH filtering. The covariance matrices can be adapted for both the SOC filter and the SOH filter.

In the following, we describe how to determine reasonable parameters by testing their behavior with synthetic and in-flight data. We will not determine the best parameter only with synthetic data since the filtering is sometimes less robust when applied to the in-flight data. So, we choose for every filter parameter the setting that provides more significant results.

The tests are a simple parameter study where we test fixed parameter sets. As in sec. 4.4.1, the simulation of several thousand cycles per parameter is too expensive in time to use an optimization algorithm. Moreover, it is difficult to define an objective function. On the one hand, the target properties are difficult to quantify. On the other hand, it is a multi-objective optimization problem where several target properties have to be optimized simultaneously.

SOH Filter Frequency N. In order to decide with which frequency N the SOH needs to be filtered, we compare results of frequent and rare SOH filtering. We choose $N = 20$ for the frequent filtering and $N = 100$ for the rare one. We do not want the SOH filtered too frequently, e.g. with one filter step at each cycle ($N = 1$) to avoid overfitting. The filter parameters of the SOC filter used here are the covariance matrices $P_0^{\mathrm{SOC}} = 10^{-25} \cdot J_n$, $R_{\mathrm{I}}^{\mathrm{SOC}} = 1$, and $Q^{\mathrm{SOC}} = 10^{-29} \cdot I_n$. Here, J_n is a $n \times n$ matrix of ones and I_n is the identity matrix of size n, where n is the size of the states vector. The covariance matrices for the SOH filter are $P_0^{\mathrm{SOH}} = 10^{-20} \cdot J_n$, $R_{\mathrm{V}}^{\mathrm{SOH}} = 2.5 \cdot 10^{-5}$, and $Q^{\mathrm{SOH}} = 10^{-16} \cdot I_n$. The initial states are $\mathrm{SOC}_{\mathrm{anode},0} = 80$ %, $\mathrm{SOC}_{\mathrm{cathode},0} = 20$ %, and $L_{\mathrm{SEI},0} = 10$ nm.

In Fig. 5.7, we compare the two filtering results. We choose the results of the in-flight data since these show a significant difference in the filtering behavior for the two frequencies. In a) and c) the error of the cell voltage and the EoDV is depicted. Both show that the error is significantly smaller in case of the frequent filtering. The error of the cell current in b) is almost identical in both cases. The same applies to the SOC trends in d). This can be explained by the fact, that these quantities are controlled by the SOC filter. In e) the SEI thickness of the three anode discretization points is depicted. The trend is similar for both filter frequencies. Only the trends of the single discretization points deviate more in case of the frequent filtering. An explanation could be that by simply having more chances to change, the trends can deviate more. Also, the error of the voltage values can be reduced faster this way. As the filter appears to be stable in both frequency cases, we decide for the parameter which reduces the errors better, which is the filter with $N = 20$.

Measurement Covariance Matrix R. For the choice of the measurement covariance matrix R there are two possibilities. Either one determines the variance of the corresponding measurement or several values can be tested with regard to the filter behavior. In case of the SOH filter, which uses the voltage measurement, we determined the variance of the measurements, which results in $R_{\mathrm{V}}^{\mathrm{SOH}} = 2.5 \cdot 10^{-5}$, cf. sec. 5.2.2. For the SOC filter, which uses the current measurements, we tested $R_{\mathrm{I}}^{\mathrm{SOC}} \in \{1, 10^{-1}, 10^{-2}, 10^{-3}, 10^{-4}, 10^{-5}\}$. The covariance R_{I} could also be obtained from the variance of the measurement. Here, we determine this parameter by testing, as this is an additional possibility to make the filter more stable.

The other filter parameters of the SOC filter used for the test are the covariance matrices $P_0^{\mathrm{SOC}} = 10^{-25} \cdot J_n$ and $Q^{\mathrm{SOC}} = 10^{-29} \cdot I_n$. The covariance matrices for the SOH filter are $P_0^{\mathrm{SOH}} = 10^{-15} \cdot J_n$ and $Q^{\mathrm{SOH}} = 5 \cdot 10^{-17} \cdot I_n$. The frequency of the SOH filter is $N = 20$. The initial states are $\mathrm{SOC}_{\mathrm{anode},0} = 95$ %, $\mathrm{SOC}_{\mathrm{cathode},0} = 22$ %, and $L_{\mathrm{SEI},0} = 10$ nm.

Fig. 5.8 shows the results of the test for the synthetic data. In a) and c) we see that the error of the cell voltage and the EoDV are the smallest for $R_{\mathrm{I}}^{\mathrm{SOC}} = 10^{-1}$ and $R_{\mathrm{I}}^{\mathrm{SOC}} = 1$. The error of the cell current in b) is almost identical for all values except for $R_{\mathrm{I}}^{\mathrm{SOC}} = 10^{-3}$, which produces a larger error than the other values. The trends of the states in d) and e) are almost identical for all values. So, for the measurement covariance matrix of the SOC filter, both $R_{\mathrm{I}}^{\mathrm{SOC}} = 10^{-1}$ and $R_{\mathrm{I}}^{\mathrm{SOC}} = 1$ are suitable.

Process Covariance Matrix Q. The process covariance matrix Q accounts for the uncertainty in the model. It is another parameter that can be used to control the filter behavior. If not equal to zero, it prevents the state covariance matrix, cf. eq. (5.10), from becoming too small, which would result in a decrease in the filter corrections. However, it can also lead to a filter that corrects too much. To determine the matrix, which leads to an accurate correction, we test again several values. We only test diagonal matrices with identical entries, and state in the following the factor with which the matrix I_n is multiplied.

Here, we describe the results for the process covariance matrix of the SOH filter

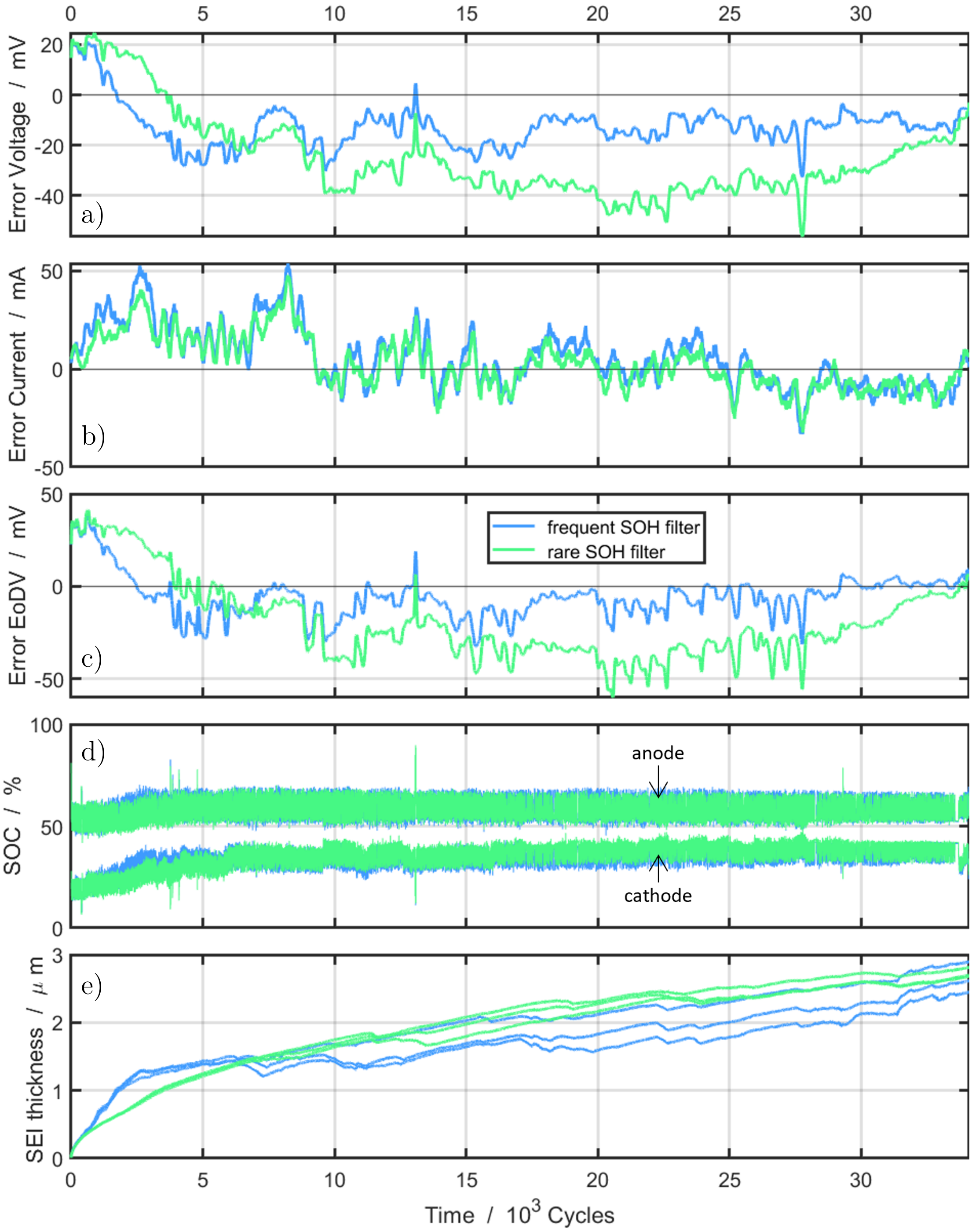

Figure 5.7: Filtering behavior for different SOH filter frequencies for in-flight data. Comparison between filtering every 20 cycles to every 100 cycles. a) Error of cell voltage. b) Error of cell current. c) Error of EoDV. d) Trend of SOC of anode and cathode. e) Trend of SEI thickness.

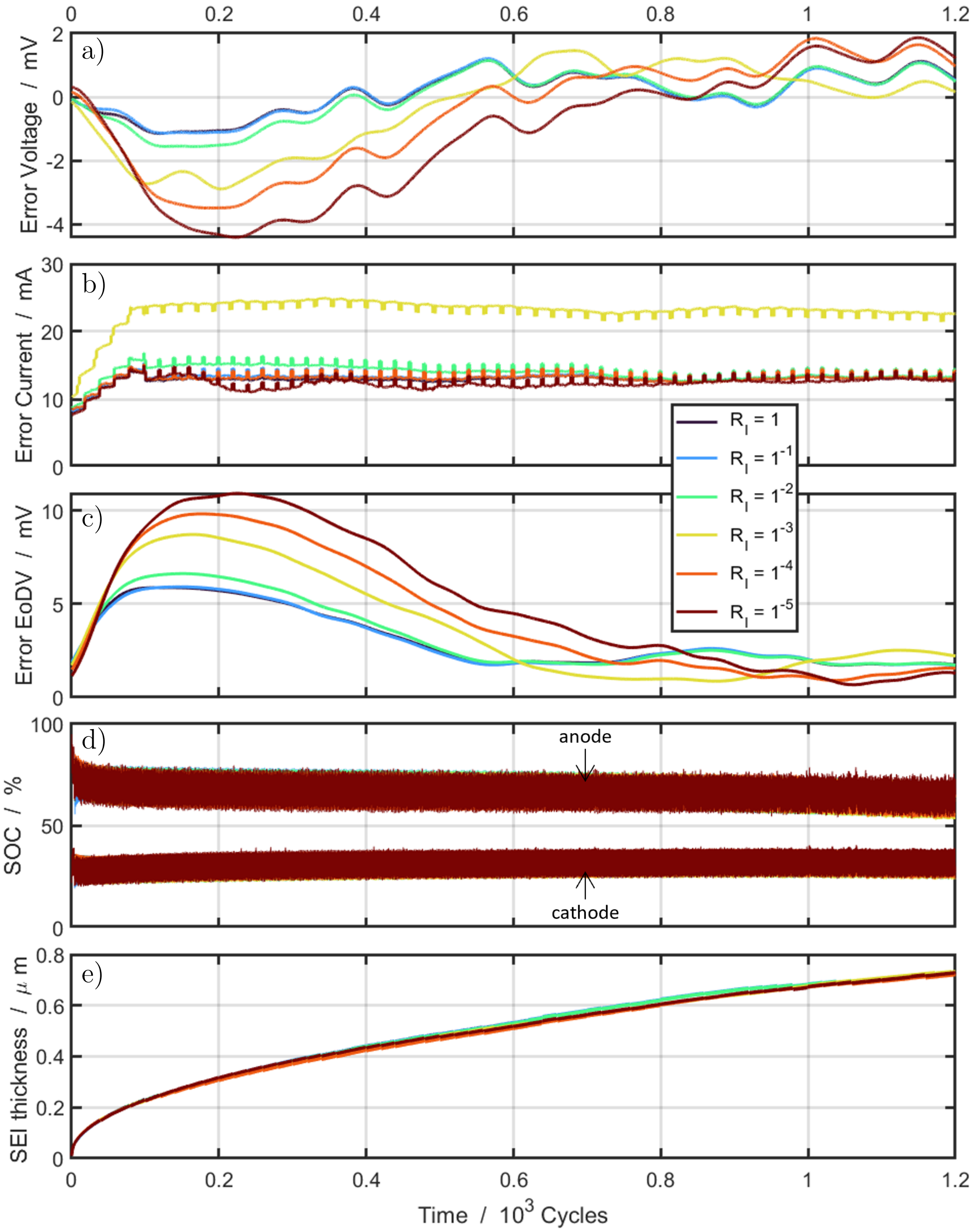

Figure 5.8: Comparison of filtering behavior for different measurement covariance matrix values for synthetic data. a) Error of cell voltage. b) Error of cell current. c) Error of EoDV. d) Trend of SOC of anode and cathode. e) Trend of SEI thickness.

tested with in-flight data. The values tested are $5 \cdot 10^{-17}$,10^{-16},$5 \cdot 10^{-16}$, and $5 \cdot 10^{-15}$. The filter parameters of the SOC filter are the covariance matrices $P_0^{\mathrm{SOC}} = 10^{-25} \cdot J_n$, $R_{\mathrm{I}}^{\mathrm{SOC}} = 1$, and $Q^{\mathrm{SOC}} = 10^{-29} \cdot I_n$. The other parameters for the SOH filter are the covariance matrices $P_0^{\mathrm{SOH}} = 10^{-20} \cdot J_n$ and $R_{\mathrm{V}}^{\mathrm{SOH}} = 2.5 \cdot 10^{-5}$. The frequency of the SOH filter is $N = 20$. The initial states are $\mathrm{SOC}_{\mathrm{anode},0} = 80$ %, $\mathrm{SOC}_{\mathrm{cathode},0} = 22$ %, and $L_{\mathrm{SEI},0} = 50$ nm.

The results are shown in Fig. 5.9. The first thing to notice is that the simulation aborts for $5 \cdot 10^{-15}$. Although this factor produces the smallest error of the voltages, it is not applicable as the filter needs to be stable. The other factors lead to a stable filter behavior. All factors lead to a similar error of the cell current and also to a similar trend of the SOCs as shown in b) and d). Differences can be observed in the error of the cell voltage and the EoDV in a) and c), where the factor $5 \cdot 10^{-16}$ leads to the smallest error, followed by 10^{-16}. When observing the growth of the SEI in e), we see that all factors that lead to a stable filter behavior have a similar trend. For the factor $5 \cdot 10^{-16}$, we see that the state fluctuates a lot. The fluctuation decreases with a decreasing value of the matrix factor, which is to be expected since a higher value of matrix entries adds more uncertainty to the state covariance matrix. For $5 \cdot 10^{-17}$ the SEI thickness values of the different discretization points deviate stronger than for the other factors. The factor 10^{-16} produces a physically sensible trend.

Since the choice of the right filter parameter is a multi-objective optimization problem, there might not exist an optimal parameter. Increasing the matrix factor of the process covariance matrix improves the error convergence of the voltage. While at the same time, smaller values seem to lead to a more stable filter behavior and physically sensible trends of the estimated states. The parameter needs to be chosen according to the specific requirements.

The results for the process covariance matrix of the SOC filter and tests with the synthetic data can be found in sec. C.

Initial Covariance Matrix of States P_0. The state covariance matrix P_k represents the uncertainty of the states. In contrast to the other filter parameters, it is not constant but evolves in time in every filter step. So, only the initial state covariance matrix P_0^{SOC} and P_0^{SOH} for the SOC and the SOH filter needs to be determined. As described before, there are several possibilities to determine these filter parameters. Again, we test different matrices with identical entries. But in this case we choose a matrix type with no zero elements. One could also

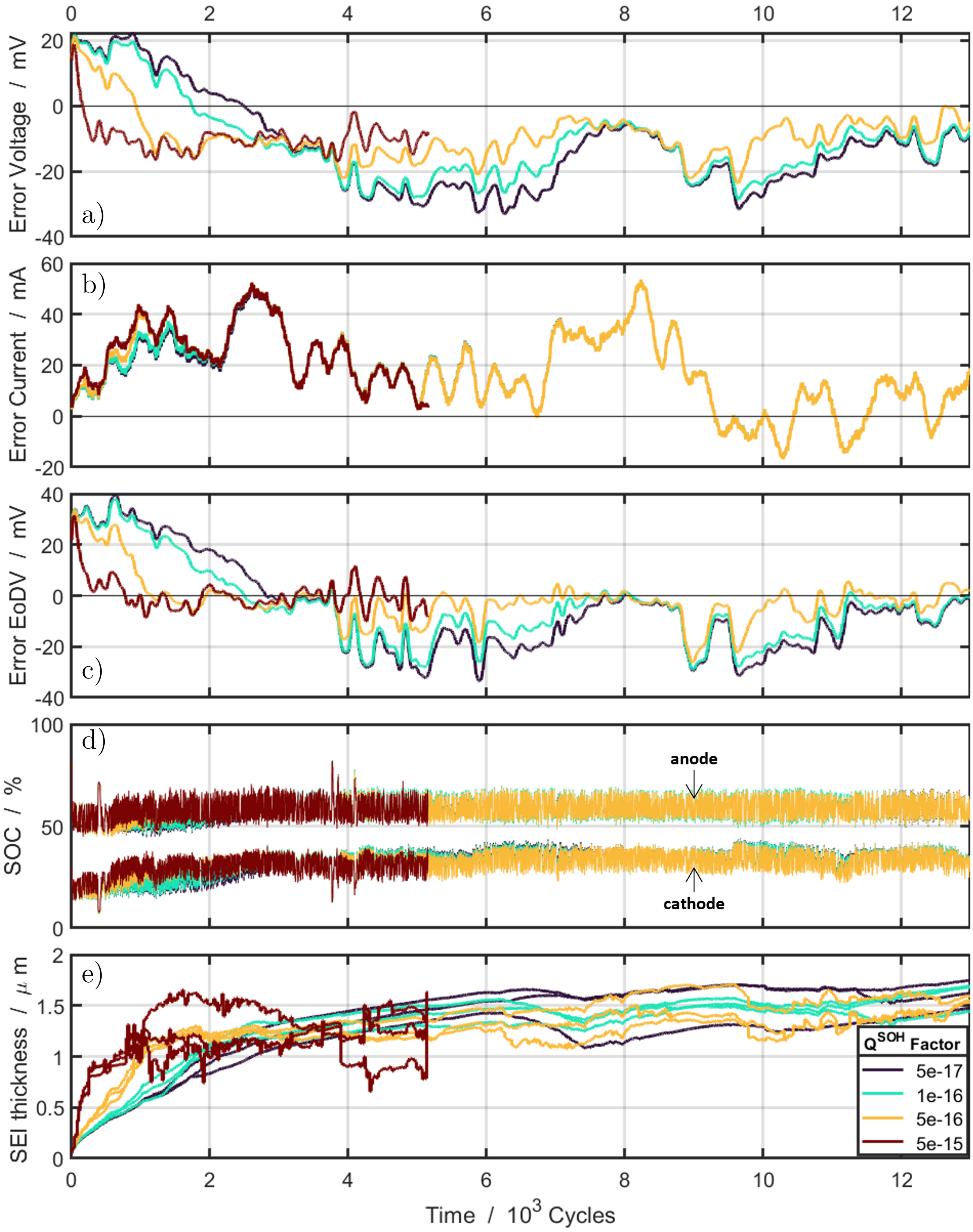

Figure 5.9: Comparison of filtering behavior for different process covariance matrices Q^{SOH} for inflight data. a) Error of cell voltage. b) Error of cell current. c) Error of EoDV. d) Trend of SOC of anode and cathode. e) Trend of SEI thickness.

use diagonal matrices, but these turned out to lead to unstable filter behavior in preliminary tests. In the following, we only state the factor multiplied with the matrix J_n.

Here, we only show exemplarily the results of the SOC filter state covariance matrix for synthetic data. Results for in-flight data and for the SOH filter state covariance matrix can be found in sec. C.

We test the factors 10^{-15},10^{-20},10^{-25}, and 10^{-30}. The other filter parameters of the SOC filter used here are the covariance matrices $R_{\mathrm{I}}^{\mathrm{SOC}} = 0.1$ and $Q^{\mathrm{SOC}} = 10^{-29} \cdot I_n$. The covariance matrices for the SOH filter are $P_0^{\mathrm{SOH}} = 10^{-15} \cdot J_n$, $R_{\mathrm{V}}^{\mathrm{SOH}} = 2.5 \cdot 10^{-5}$, and $Q^{\mathrm{SOH}} = 5 \cdot 10^{-17} \cdot I_n$. The frequency of the SOH filter is $N = 100$. The initial states are $\mathrm{SOC}_{\mathrm{anode},0} = 95$ %, $\mathrm{SOC}_{\mathrm{cathode},0} = 22$ %, and $L_{\mathrm{SEI},0} = 10$ nm.

Fig. 5.10 shows the results of the test of different matrices. As for the previous parameters, we show the errors of the measurable quantities and the trends of the states. In this case, we do not show the error of the cell current, since it is identical for all matrix factors. The error of the cell voltage and the EoDV in a) and b) show only little differences. The factor 10^{-25} seems to have the smallest error, but with only a very small advantage over the other factors. In c) we show the SEI growth and in d) the trend of the SOCs. In both cases, the different matrices produce almost identical results. Only when zoomed in to the first few cycles, as shown in e), a difference can be detected. Namely, the correction in the fourth cycle, when the SOC filter sets in, is stronger for the factors greater than 10^{-30}.

Altogether, the choice of the initial state covariance matrix does not seem to have much influence on the filter result. The value 10^{-25} seems to give the best result with a small advantage. This value also leads to the most stable result when tested with in-flight data, as can be seen in Fig. C.3.

5.2.5 Results of MTS Algorithm

After testing the influence of the initial states and determining appropriate filter parameters, we demonstrate the overall performance of the MTS algorithm, both for synthetic and for in-flight data.

In both cases, almost the same setting for the algorithm is chosen. Only the initial states differ. The SOC filtering is started in the fourth cycle and it gets filtered

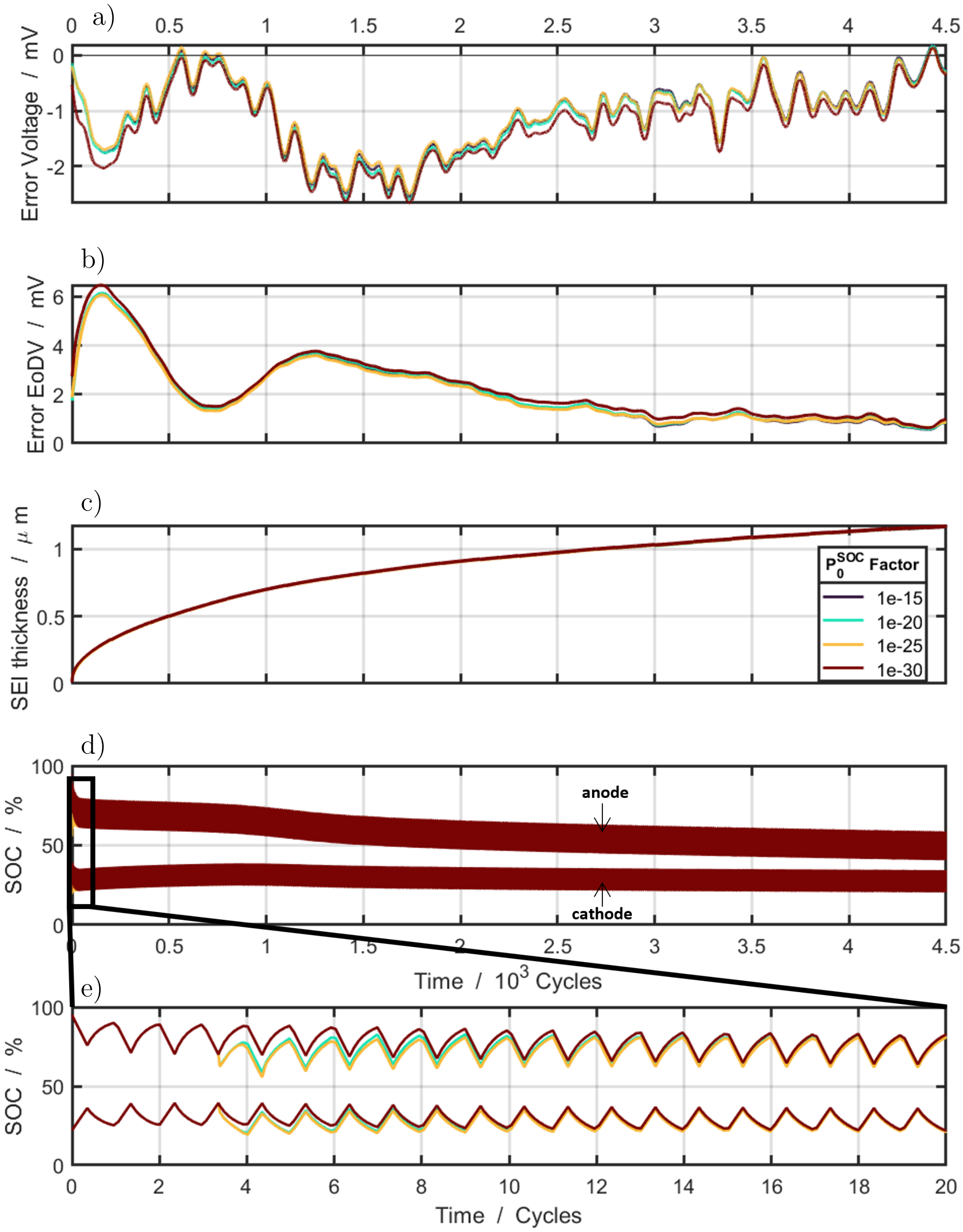

Figure 5.10: Comparison of filtering behavior for different initial covariance matrices of states P_0^{SOC} for synthetic data. a) Error of cell voltage. b) Error of EoDV. c) Trend of SEI thickness. d) Trend of SOC of anode and cathode. e) Zoom-in of initial 20 cycles of trend of SOC of anode and cathode.

during charging. The SOH is filtered every 20 cycles. The filter parameters of the SOC filter used here are the covariance matrices $P_0^{\mathrm{SOC}} = 10^{-25} \cdot J_n$, $R_{\mathrm{I}}^{\mathrm{SOC}} = 1$, and $Q^{\mathrm{SOC}} = 10^{-29} \cdot I_n$. Here, J_n is a $n \times n$ matrix of ones and I_n is the identity matrix of size n, where n is the size of the states vector. The covariance matrices for the SOH filter are $P_0^{\mathrm{SOH}} = 10^{-20} \cdot J_n$, $R_{\mathrm{V}}^{\mathrm{SOH}} = 2.5 \cdot 10^{-5}$, and $Q^{\mathrm{SOH}} = 10^{-16} \cdot I_n$. The battery model used here for the simulation is the one described in sec. 2 with the parameters obtained in sec. 4.

Results for Synthetic Data

We show the results of filtering synthetic data with the MTS algorithm in Fig. 5.11 and Fig. 5.12. The initial states of the filter are $\mathrm{SOC}_{\mathrm{anode},0} = 80$ %, $\mathrm{SOC}_{\mathrm{cathode},0} = 20$ %, and $L_{\mathrm{SEI},0} = 1\mu$m. The true initial states of the synthetic data are $\mathrm{SOC}_{\mathrm{anode},0} = 98$ %, $\mathrm{SOC}_{\mathrm{cathode},0} = 25$ %, and $L_{\mathrm{SEI},0} = 10$ nm as stated in Table B.2 and B.4. We choose these large errors to test the efficiency of the algorithm.

Fig. 5.11 comprises the results for the outputs and measurements and Fig. 5.12 shows the estimated states compared to the true states, which are known in case of the synthetic data. We show the long-term behavior of around 4,000 simulated and filtered cycles and zoom-ins at two different positions to demonstrate how the filter results evolve in time. In Fig. 5.11 b) and d) we depict the cell voltage and cell current of the whole simulated period. The figures include the cycling protocol for the simulation of the synthetic data, the filter output, and the error between synthetic and filtered data. a) and c) show zoom-ins of the first ten cycles and of the ten cycles after the 1,500th cycle. In e) we see the synthetic data, the filter output, and the error of the EoDV.

Fig. 5.12 shows the corresponding states. The SOC of anode and cathode is depicted in b) with zoom-ins corresponding to Fig. 5.11 in a). The result for the SEI thickness is shown in c). We show the true states, the states estimated by the filter, and the error between true and estimated states.

The zoom-ins in both figures do not include the errors, as the extent of the agreement is obvious.

We observe in Fig. 5.11 a), b), and e) that the discrepancy between cell voltage and EoDV from the synthetic data is very large at the beginning. This is to be expected since the SEI thickness has a large initial error. The error is efficiently reduced in the first few hundred cycles and stays close to zero afterwards. In the

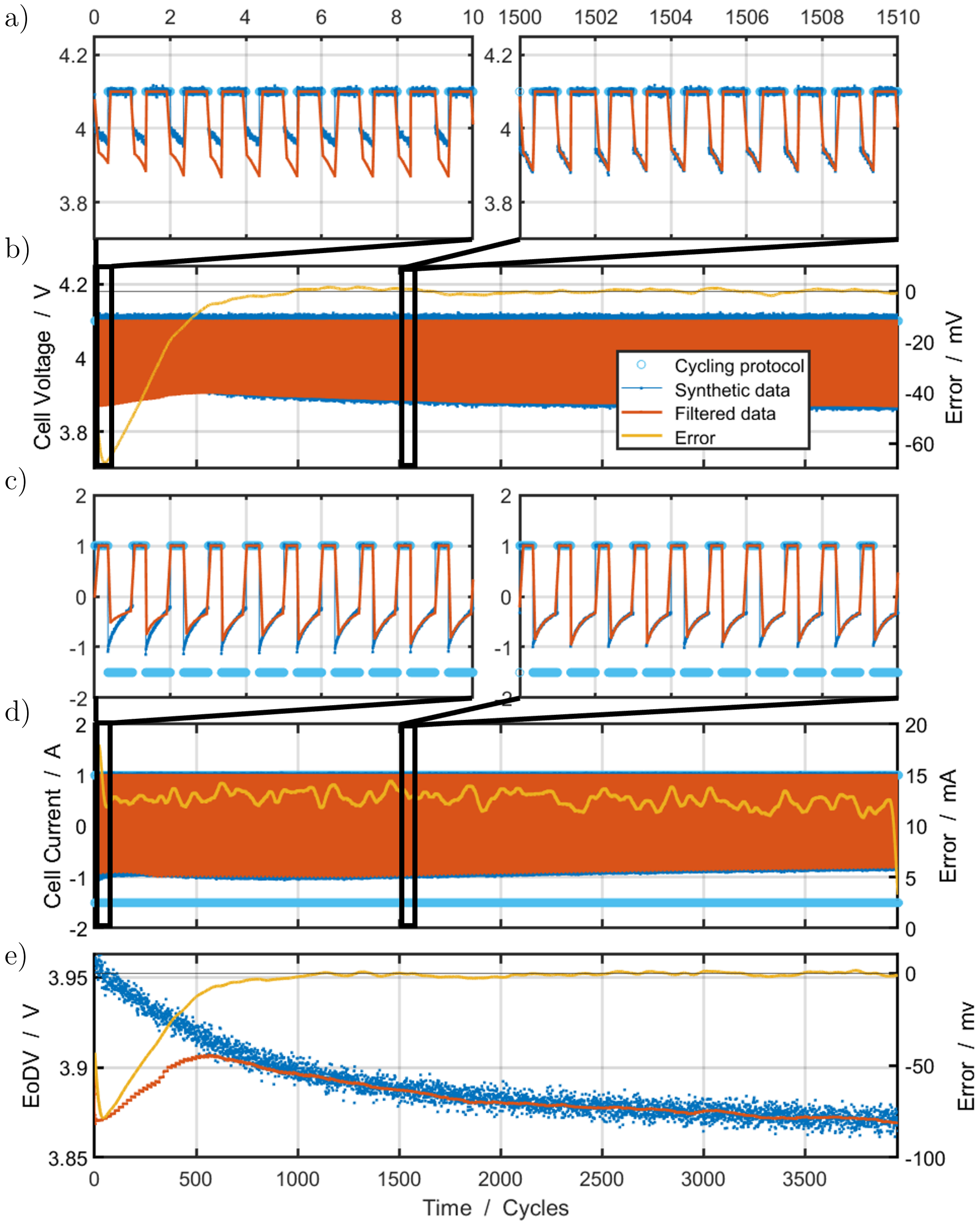

Figure 5.11: Results of filtering synthetic data with MTS algorithm. Synthetic measurement points and simulation output are displayed for the whole period of 4,000 cycles and zoom-ins of ten cycles at beginning and after 1,500 cycles. a) Zoom-ins of cell voltage. b) Cell voltage with error. c) Zoom-ins of cell current. d) Cell current with error. e) EoDV with error.

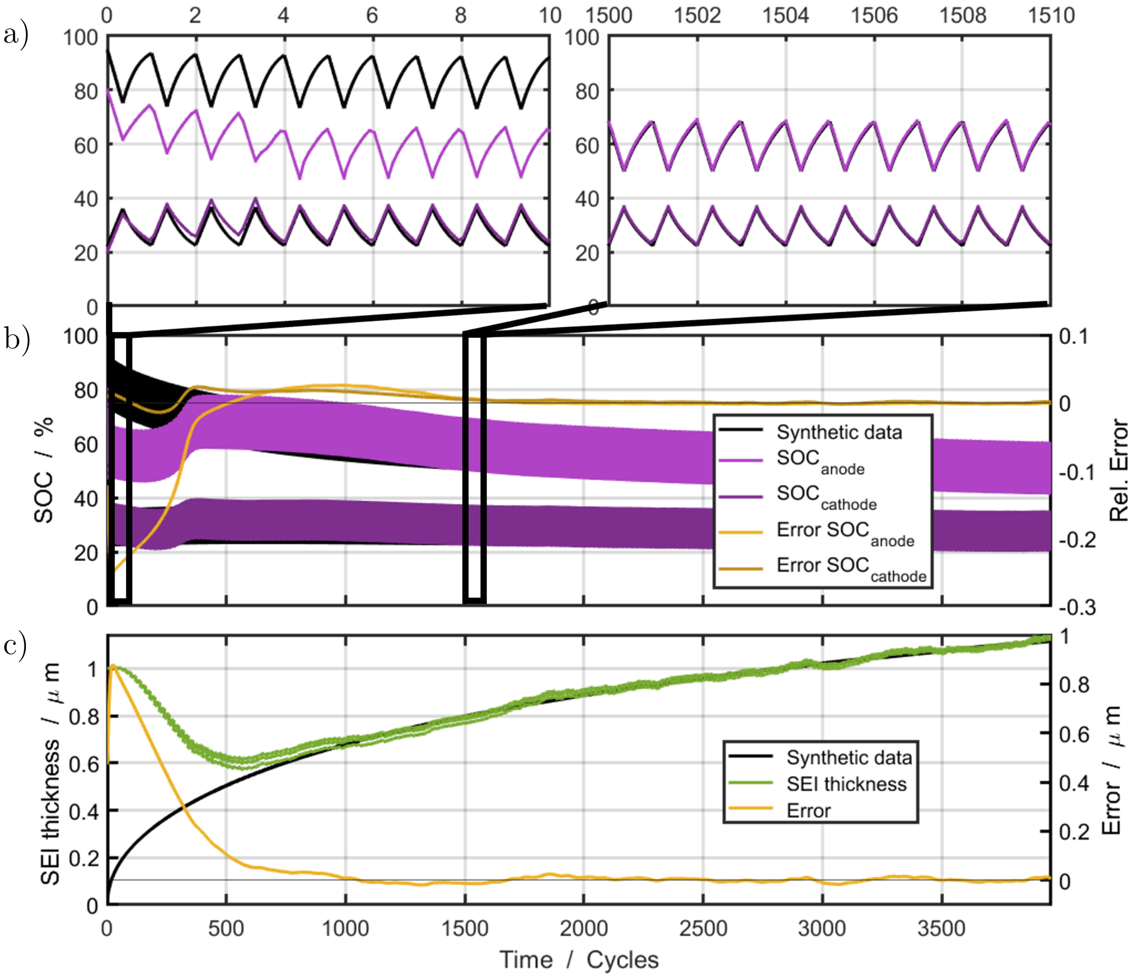

Figure 5.12: Results of filtering synthetic data with MTS algorithm. Filtered states are displayed for the whole period of 4,000 cycles and zoom-ins of ten cycles at beginning and after 1,500 cycles. a) Zoom-ins of anode and cathode SOC. b) SOCs with errors. c) SEI thickness with error.

zoom-in after 1,500 cycles, we observe a good accordance between synthetic and filtered data.

In case of the cell current in c) and d) the discrepancy is less than for the voltage. But still, the accordance between filtered and synthetic data gets better, as can be seen in c) in the zoom-ins.

Observing the estimated states in Fig. 5.12 shows the same behavior. The error of the states is very large at the beginning, especially for the anode SOC and the SEI thickness, but converges efficiently to zero after a few hundred cycles, as can be seen in b) and c). When observing the zoom-in in a), we also see how the match between true and filtered SOC gets better and that they are in very good accordance in the second zoom-in.

The zoom-in of the first ten cycles shows that the deviation between the true anode SOC and the estimated state gets worse when the SOC filter sets in. This can be explained by the fact that there are several SOC ranges that reduce the output error. This could be due to the plateaus of the OCV curve for the anode. But despite the initial increase of the error, the true value is reliably found later.

This test of filtering synthetic data demonstrates, that our MTS algorithm works very reliably for this kind of data even when the states have a huge initial error. The true states are estimated correctly both for the SOCs and for the SOH after a few hundred cycles. This proves that the algorithm performs as intended when the model is known.

Results for In-flight Data

Fig. 5.13 and Fig. 5.14 show the results of filtering the in-flight data of satellite REIMEI with the MTS algorithm. The data comprise the first 34,000 cycles, which is the period between August 2005 and December 2011. Fig. 5.13 shows the results of the measurements and outputs and Fig. 5.14 shows the results of the estimated states. Both the entire period that was simulated and filtered is displayed, as well as zoom-ins of the first ten cycles and the first 500 cycles. Here, the initial states are $\mathrm{SOC}_{\mathrm{anode},0} = 80$ %, $\mathrm{SOC}_{\mathrm{cathode},0} = 20$ %, and $L_{\mathrm{SEI},0} = 10$ nm.

In Fig. 5.13 a) and b), we see the cell voltage, including the CV cycling protocol, the in-flight measurements, and the filtered voltage. The corresponding error between the measured and the filtered voltage, which is shown in b) for the whole period, was smoothed with a Gaussian filter. a) shows the zoom-ins. The same structure is used for the cell current in c) and d) and for the EoDV in e) without the zoom-ins.

We see in b), d) and e), that the error is reduced quickly and stays relatively small over the whole period. In d) it seems as if the filtered current does not cover the whole range of measured values. When examining the behavior in the zoom-in in c) on the left-hand side, we see that only the first few points of each charging period are not hit. This might be due to the fact that in the simulation the period of CC charging before switching to CV charging is too short to be depicted. Furthermore, we see that the simulation matches the measurements

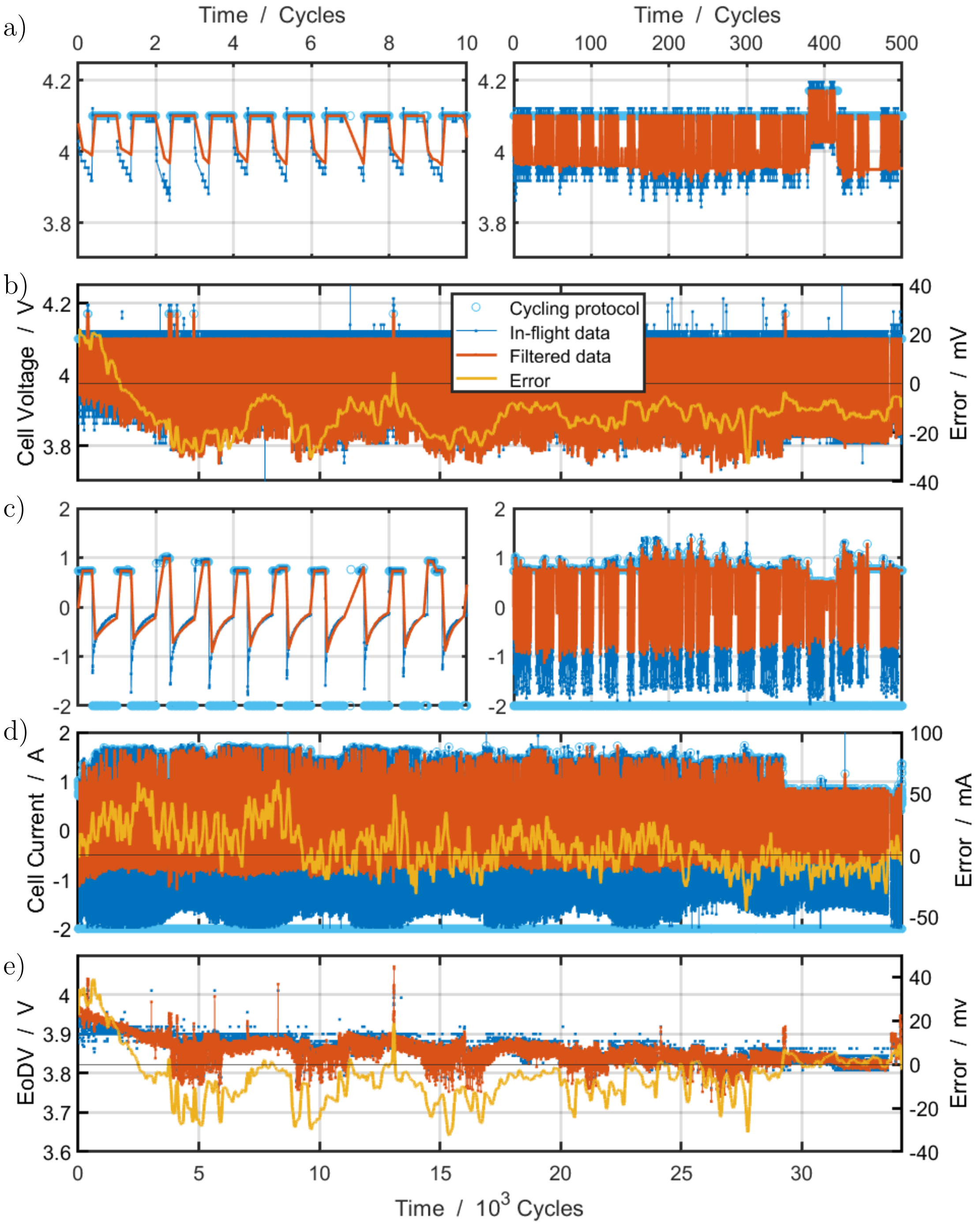

Figure 5.13: Results of filtering in-flight data with MTS algorithm. Measurement points and simulation output are displayed for the whole period of 34,000 cycles and zoom-ins of first ten and first 500 cycles. a) Zoom-ins of cell voltage. b) Cell voltage with error. c) Zoom-ins of cell current. d) Cell current with error. e) EoDV with error.

a)

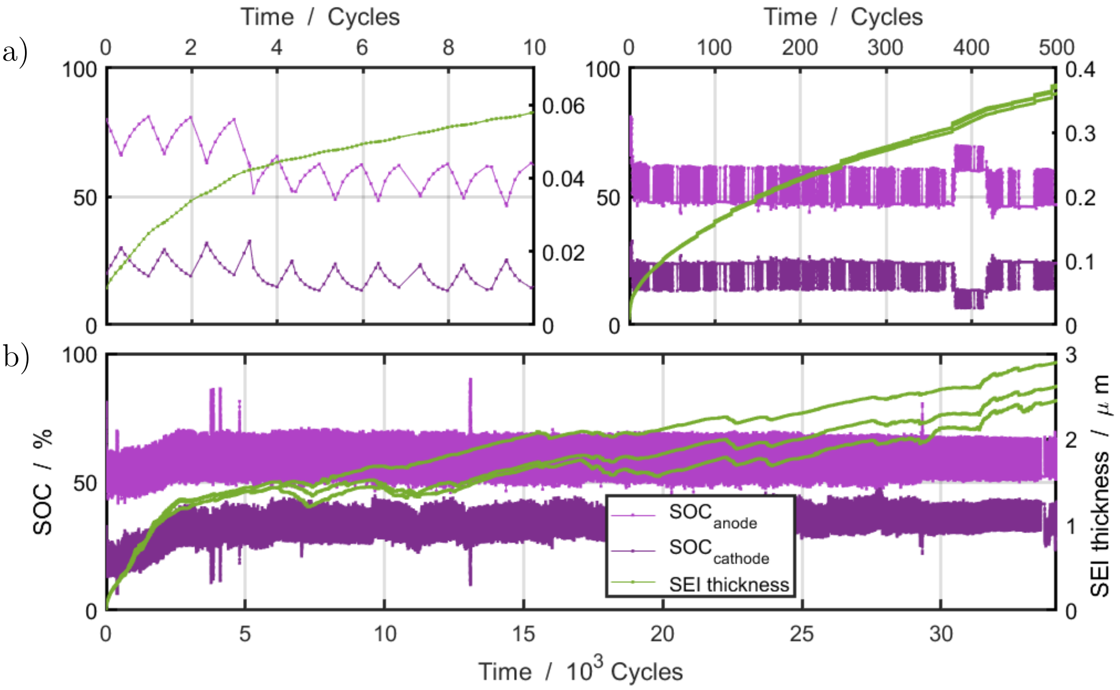

Figure 5.14: Results of filtering in-flight data with MTS algorithm. Filtered states are displayed for the whole period of 34,000 cycles and zoom-ins of first ten and first 500 cycles. a) Zoom-ins of SOC and SEI thickness. b) SOC and SEI thickness of whole period.

very accurately during charging, after the SOC filtering is started in the fourth cycle. Also in the case of voltage in a), the simulation agrees better with the measurements after the fourth cycle.

In Fig. 5.14, the filtered states are depicted. In case of the SOC, we show only one entry of the state vector for anode and cathode respectively, since they all have a very similar trend. In the case of SEI thickness, the state vector consists of three entries for the discretization points of the anode. These can have very different trends under certain filter conditions. Also, the SEI grows inhomogeneously as has been described in [15] and in sec. 4.4, which is why it is sensible to examine the growth behavior at different discretization points.

In a) in the zoom-in on the left-hand side, the onset of SOC filtering is clearly seen when the SOC of the anode and cathode are strongly corrected by the filter. When observing the filtered states of the whole period in b), we see that the states have a physically sensible trend. The SEI is growing with a square root of time behavior at the beginning and then it changes into a linear growth behavior. This is what we expect, as this aging behavior can be seen in experiments [51, 33, 46]. Furthermore, we see in a) on the right-hand plot and in b) that the SEI is growing inhomogeneously, which is also consistent with experimental studies [16, 42, 79, 70].

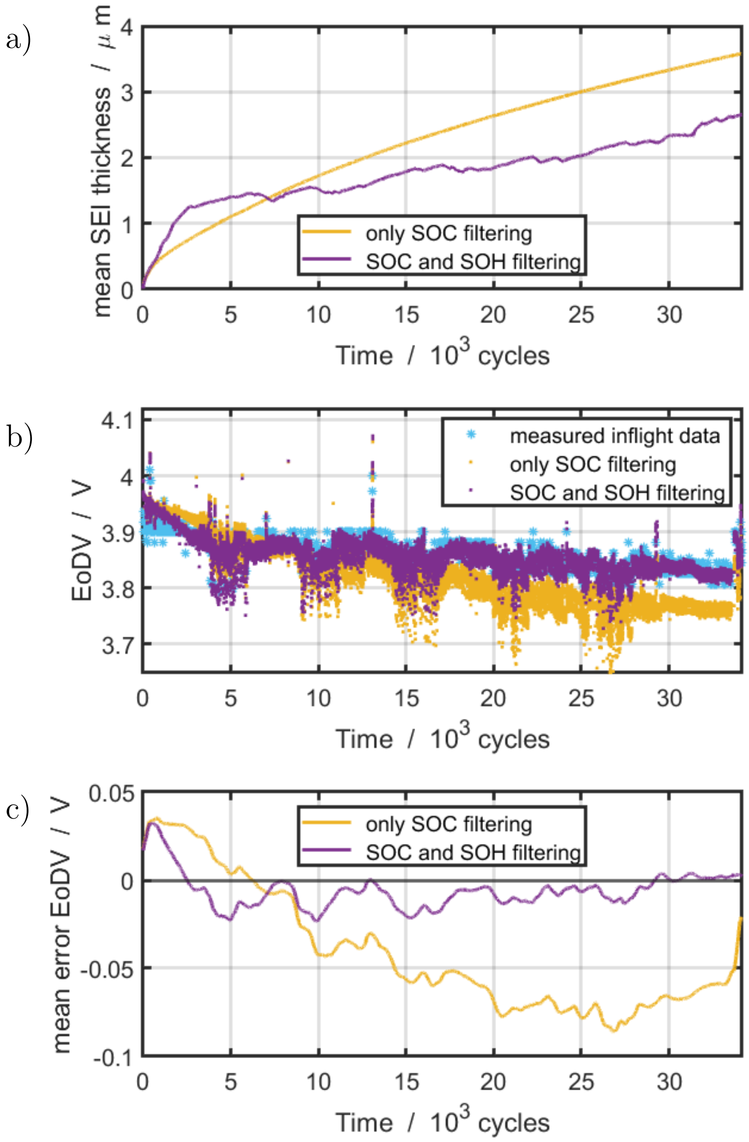

Figure 5.15: Comparison of filtering in-flight data with MTS algorithm and filtering only SOC. a) Trend of SEI thickness. b) Trend of simulated EoDV compared to measured data. c) Error of EoDV.

To prove the necessity of the MTS algorithm, we examine whether it is necessary to estimate the SOH in addition to the SOC. For this purpose, we estimate the entire period of in-flight data using only the SOC filter and compare the results with those of the MTS algorithm. All parameters and initial states remain unchanged. Fig. 5.15 shows this comparison. In a) we see the trends of the SEI thickness. In b) the EoDV trends are compared to the measured data. And c) shows the Error of EoDV. We see that the error is much larger when only the SOC is filtered and that it is not possible to obtain the right EoDV if not also the SOH is filtered. From this we can conclude, that it is indispensable for the reliability to estimate both the SOC and SOH.

5.3 Investigation of Models with Kalman Gain

The Kalman filter is used to compensate for the uncertainty in the measured data. In addition, the filter takes uncertainties in the model into account and can counteract them. In case of the in-flight data, unlike the synthetic data, we have the additional uncertainty that we do not know the true model.

Up to this point, the degradation model that was determined by the parameter study in sec. 4 was used for the state determination. This was parameterized with the satellite battery data, so it can be assumed that it already fits well. Now, the filter can give further hints on the goodness of the model. On the one hand, this allows the parameters chosen for the model to be evaluated, and on the other hand, the model itself can be evaluated, meaning whether the model represents the processes that are mainly responsible for the degradation with reliable accuracy.

The degree to which the filter corrects the prior estimate of the time update of the model can be read from the value $K_k(y_k - \hat{y}_k)$ from eq. (5.13). We call this value Kalman gain correction. If the true model is known and used for the simulation, the filter will correct the state only at the beginning of the simulation until the output error is small enough. Afterwards, there will only be small corrections and the value of the Kalman gain correction will be close to zero. Assuming that the model is inaccurate or represents the processes insufficiently, the filter will have to correct the states the whole time to reduce the output error. This would be the case if e.g. the chosen model results in a SEI growth, which is faster than in reality. Then the filter would need to reduce d_{SEI} during the whole period and the Kalman gain correction of the SOH would be negative. So, a Kalman gain correction value close to zero is an indicator for the accuracy of the model.

Furthermore, it is necessary that the EoDV error is minimized and that the SEI thickness shows a reasonable evolution, meaning that it grows in an expectable

Table 5.1: Scaling factors of degradation model parameters for model studies with Kalman gain correction.

Model	1	4	5	6	9	13	14	18	19	22	23	25	26	27
diffusion coefficient D^{e^-}	0.1	0.1	1	10	10	0.1	1	10	0.1	0.1	1	0.1	1	10
conductivity $\kappa_{\mathrm{SEI}}^{\mathrm{Li}^+}$	0.1	1	1	1	10	1	1	10	0.1	1	1	10	10	10
migration factor ω	0.1	0.1	0.1	0.1	0.1	1	1	1	10	10	10	10	10	10

order of magnitude and neither the growth rate nor the thickness itself becomes negative. Especially, if the model respectively the states are known, which is the case for synthetic data, the time evolution of the SEI thickness is also given.

Here, we will only study the Kalman gain correction of the SOH in dependence on the degradation model. First, we investigate the filter behavior when the model is altered from the true model, which we know in case of the synthetic data. Afterwards, we will apply the filter to the in-flight data to learn more about the accuracy of our model in case of an actually unknown model.

To investigate the filter behavior for different models, we vary the three parameters of the degradation model, to be exact the diffusion coefficient D^{e^-}, the conductivity $\kappa_{\mathrm{SEI}}^{\mathrm{Li}^+}$, and the migration factor ω, by orders of magnitude and multiplied them with the scaling factors 0.1, 1, and 10. This results in a test set of 27 different degradation models. The filter parameters are chosen as described in sec. 5.2.4 and are the same as in sec. 5.2.5. The initial states are $\mathrm{SOC}_{\mathrm{anode},0} = 80$ %, $\mathrm{SOC}_{\mathrm{cathode},0} = 20$ %, and $L_{\mathrm{SEI},0} = 10$ nm. We also tested the same set with initial SEI thickness $L_{\mathrm{SEI},0} = 1\mu$m, which produced the same results.

To evaluate the models of the study, we analyze the SEI growth, the error of the EoDV, and the Kalman gain correction. The models which have a small error of the SEI thickness or the EoDV or have a small Kalman gain correction, regarding either synthetic or in-flight data, are candidates for being accurate models. A selection of such candidates is listed in Table 5.1. In Fig. 5.16 and 5.17, we show the results for these models for synthetic and in-flight data.

5.3.1 Results for Synthetic Data

In Fig. 5.16, we compare the filtering of synthetic data with ten different models. On the left-hand side, the quantities to evaluate the models are depicted for the whole range of values. On the right-hand side, zoom-ins show the relevant section or smaller values. We see that with models 14, 5, 22, 4, 23, and 6 the algorithm estimates the SEI growth very or at least reasonably accurately. The error of the EoDV is very small for models 14, 5, 22, 4, and 1, and still relatively small for models 23 and 19. Models 14, 5, 22, 4, 18, and 27 have small Kalman gain correction.

For model 14, which is the true model, we see the best fit of the SEI thickness, a very small EoDV error, and the smallest Kalman gain correction. Model 5, which differs from model 14 only in the migration factor, has similar good values in the evaluation.

If we would only consider the error of the EoDV and ignore the Kalman gain correction, model 1 could also be accurate. But both the unexpectable trend of the SEI and the significantly negative value of the Kalman gain correction lead to the conclusion that this model is inaccurate. Also, with models 1 and 19, the SEI thickness is significantly too small. A possible explanation for the small EoDV error with model 1 could be found in the model parameters. The main difference to the models that give good results is that the conductivity is an order of magnitude smaller. This parameter influences not only the growth rate of the SEI, but also the cell internal resistance via the Butler-Volmer equation. This in turn affects the voltage curve, since a larger internal resistance leads to a larger hysteresis. As a result, with the help of a large correction by the filter, the error of the EoDV can be reduced.

If we do not know the true SEI thickness, we need the EoDV error and the Kalman gain correction to decide which model is accurate. Models 23 and 19 have a relatively small EoDV error but a large Kalman gain correction, from which we can conclude that the models are incorrect. Model 6 has a plausible trend of the SEI thickness, but since both the error of the EoDV and the Kalman gain correction are large, this model can also be ruled out. Models 18 and 27 have a relatively small Kalman gain correction but a large EoDV error and also the trend of the SEI is not reasonable.

From this, we can conclude that in the case of synthetic data, where the model covers all processes of the degradation and only the model parameters are unknown, the EoDV error and the Kalman gain correction are reliable indicators for the accuracy of the model.

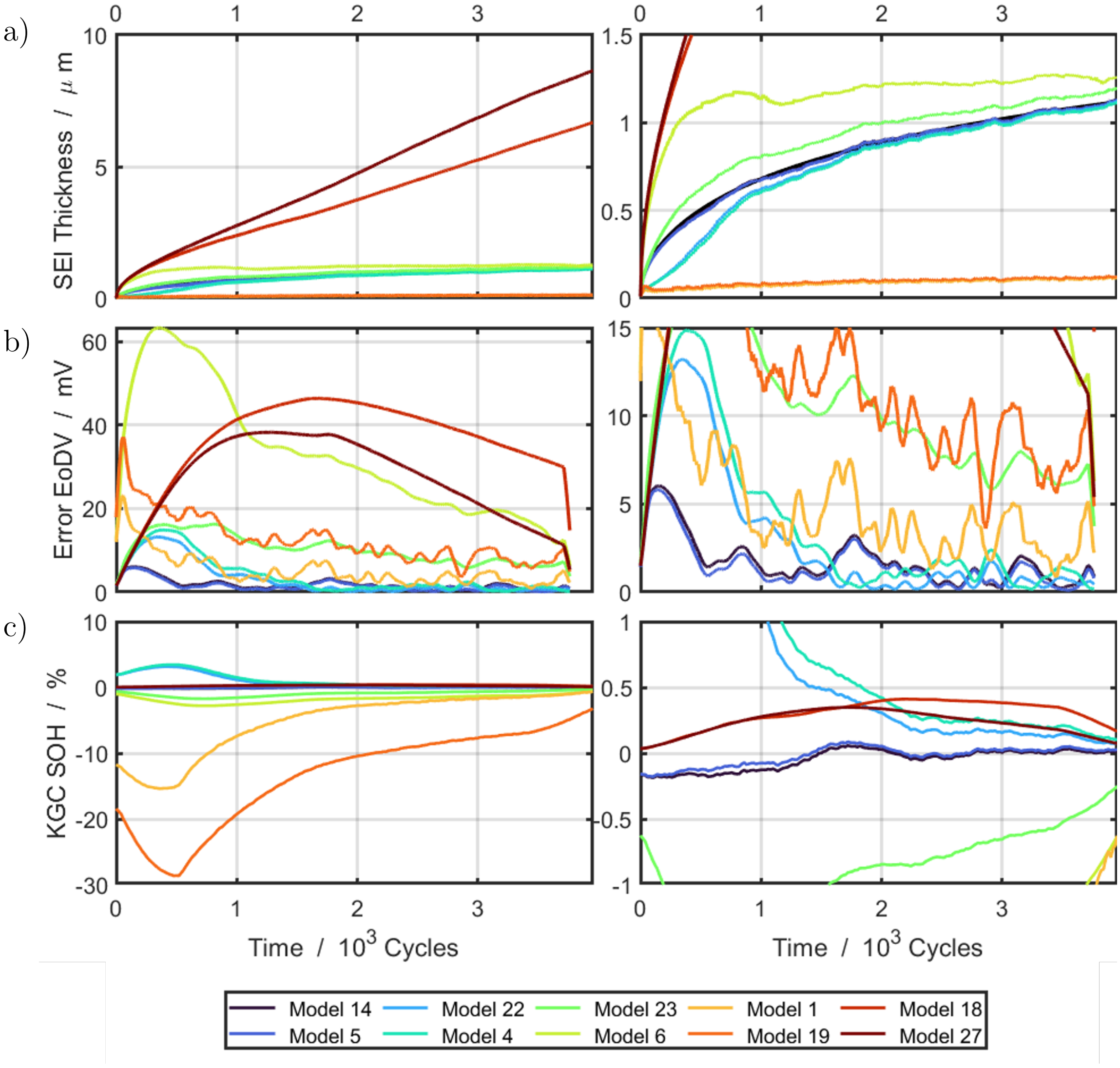

Figure 5.16: Study of degradation model parameters with the help of the Kalman gain correction. Comparison of filtering synthetic data with ten different models. Whole range on the left-hand side and zoom-ins on the right-hand side. a) SEI thickness. b) Error of EoDV. c) Kalman gain correction (KGC) for the SOH.

5.3.2 Results for In-flight Data

We will use these indicators to validate the accuracy of models used to estimate the real in-flight data. In Fig. 5.17, we compare the results of the MTS algorithm applied to the in-flight data for eleven different models. We choose these models, as they fulfill the criterion of a small EoDV or a small Kalman gain correction and demonstrate the variety of possible outcomes of this procedure.

Just as with the synthetic data, we look at the relevant quantities in their entire range on the left-hand side. On the right-hand side, we show zoom-ins to distinguish smaller values. In a) we see the trends of the SEI thickness, in b) the error of the EoDV, and in c) the Kalman gain correction of the SOH filter.

The models, which produce a small EoDV error are models 1, 4, 5, 13, 14, and 22. Models 4, 5, 9, 13, 14, 18, 22, 25, 26, and 27 have a small Kalman gain correction. The models 4, 5, 13, 14, and 22, which have both, a small EoDV error and a small Kalman gain correction, all have a similar trend of the SEI growth. This growth behavior fits our expectation, that the degradation follows a linear trend beginning from a later point of the lifetime. These models are all candidates for being accurate models for the degradation of the satellite batteries.

Again, as in case of the synthetic data, model 1 has a small EoDV error, but a large Kalman gain correction, which leads to the conclusion, that this model is no appropriate candidate.

Models 4, 13, and 22 have the smallest EoDV error. These models all have the same diffusion coefficient D^{e^-} and conductivity $\kappa_{\mathrm{SEI}}^{\mathrm{Li}^+}$. Only the migration factor ω differs. The error for model 22 is slightly larger than for model 4 and 13. From this, we can conclude that the migration factor has a small influence on the simulation and filtering behavior combined with this setting of values for D^{e^-} and $\kappa_{\mathrm{SEI}}^{\mathrm{Li}^+}$. This changes for larger values of D^{e^-} and $\kappa_{\mathrm{SEI}}^{\mathrm{Li}^+}$ as can be observed from models 9, 18, and 27. These models also only differ in the migration factor but have larger factors for the diffusion coefficient and conductivity. They all have a small Kalman gain correction but a large EoDV error. Here the difference between the models becomes more apparent. This can best be seen in the SEI growth, where the SEI grows the most for the model with the largest migration factor.

Model 14, which is the "original" one, meaning that the model parameters were fitted to the satellite batteries in sec. 4.4.1, shows a small EoDV error, a reasonable SEI growth, and a small Kalman gain correction. However, according to this evaluation procedure, model 4 even shows a slightly more accurate agreement. The difference between these models is that D^{e^-} and ω are an order of magnitude smaller in model 4, cf. Table 5.1. From this procedure, we can conclude when comparing the best model candidates, that the conductivity $\kappa_{\mathrm{SEI}}^{\mathrm{Li}^+}$ is already determined appropriately in model 14. The diffusion coefficient D^{e^-} and migration factor ω might be smaller down to one order of magnitude, keeping in mind that these two parameters influence each other.

In summary, the MTS algorithm can reliably estimate the hidden model states and it can even compensate for uncertainties in the model. Moreover, the algorithm can be used to evaluate the accuracy of the model.

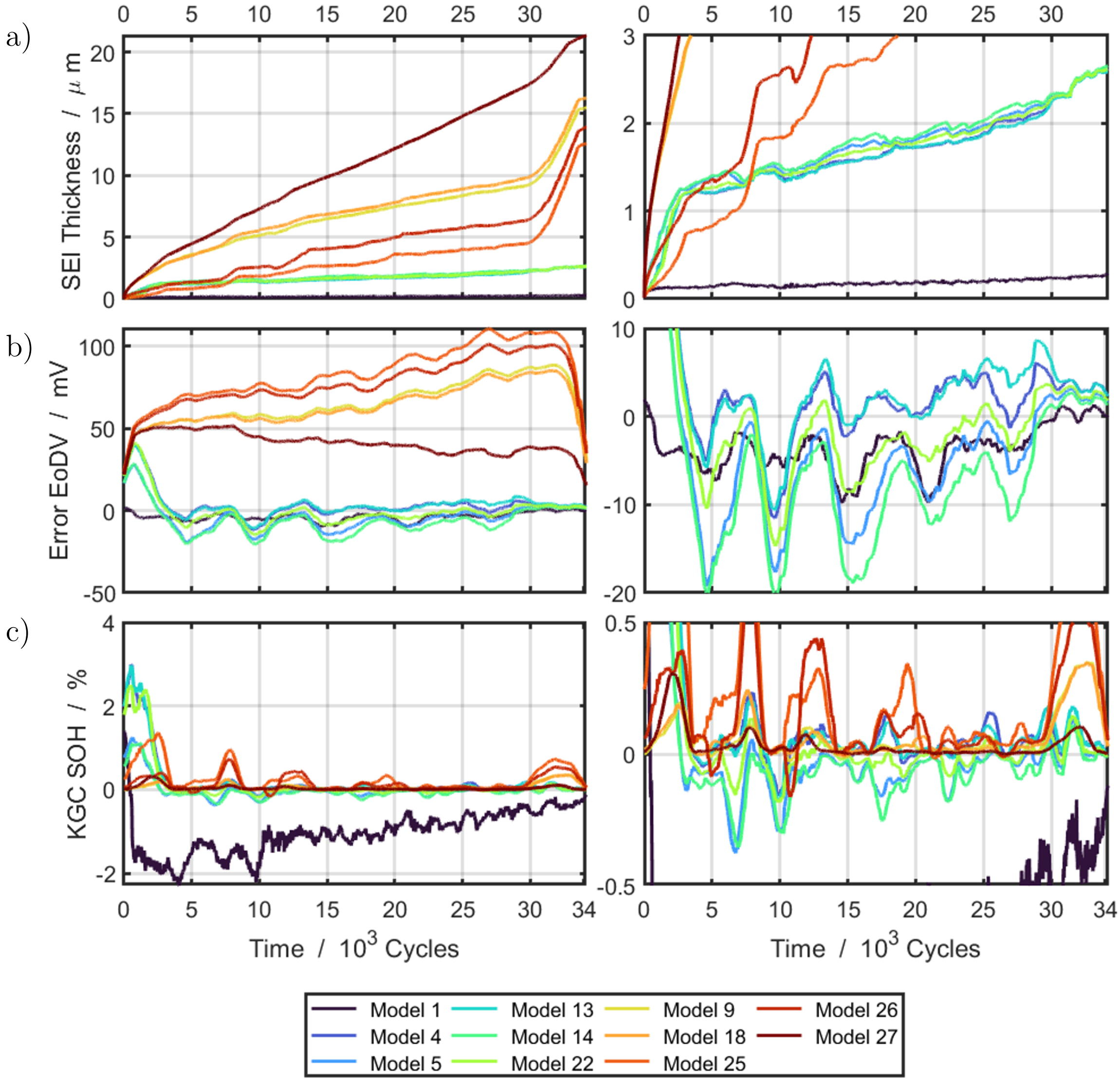

Figure 5.17: Study of degradation model parameters with the help of the Kalman gain correction. Comparison of filtering in-flight data with eleven different models. Whole range on the left-hand side and zoom-ins on the right-hand side. a) SEI thickness. b) Error of EoDV. c) Kalman gain correction (KGC) for the SOH.

6 Conclusion and Outlook

This thesis investigates the degradation of Li-ion batteries in satellites. For this purpose, we have been provided with data from JAXA (Japan Aerospace Exploration Agency). They developed the small scientific satellite REIMEI and sent it into orbit 18 years ago to investigate new technologies and take pictures of the aurora. Part of the mission was to investigate the use of commercial Li-ion batteries in aerospace applications. Over the years, the cells were charged and discharged several thousand times with a cycling profile typical for the low Earth orbit. This leads to a uniform aging of the cells. This recorded data on cell aging is a unique basis for studying the long-term degradation of Li-ion batteries.

In order to gain insights into the cells orbiting on a low Earth orbit, which cannot be accessed directly, physical-based models are used that describe the processes in the battery and can be compared with the measured battery data using simulations. To this end, we first outline two models that describe the processes in the cell during cycling and aging and that, when coupled, provide a complete model to simulate the long-term aging of satellite cells. For aging, the process that is the main reason for capacity fade in Li-ion batteries was considered. This is the continuous growth of the solid-electrolyte interphase.

The models need to be calibrated using experimental data. For this purpose, both the in-flight data from the satellite REIMEI batteries are available, as well as various additional data from terrestrial experiments carried out simultaneously with the satellite mission using the same cells as in the satellite. We have described the experiments in order to be able to use them for calibration of the models.

We then analyzed the in-flight data. These are important - among other things - for evaluating the models. These data are only available as raw data and metadata such as cycling protocols are missing, so they could not be used directly. We processed the data extensively, taking into account various irregularities such as data gaps, and extracted protocols from the data that can be used for the simulations.

Not only the satellite data but also CT data from the satellite batteries were processed in order to obtain parameters of the pouch cells. We used these parameters together with a surrogate optimization to fully parameterize the cell model. The degradation parameters were determined using a basic method due to the long simulation time of long-term cycling. Therefore, a parameter test space was determined in which the parameters are distributed equidistantly and from this space the parameter set that best replicates the experimental data was determined.

The parameterized models were used to simulate different scenarios in order to investigate the degradation of the cells depending on the charging and discharging currents. The models were simulated in a pseudo-2D as well as in a 3D framework. In both cases, it can be observed that the growth of the SEI depends on the current and is different at different points of the anode, meaning it grows inhomogeneously.

The parameterized models are a good basis for a more sophisticated approach to estimate the states of the battery. Knowledge of variables such as the SOC and SOH of a battery is of great interest for the battery management and for planning further steps in the use of the cell.

Since the inner states cannot be measured and both the measurements and the models are uncertain, filters are required for estimation. We have developed a multi-timescale algorithm based on Kalman filters that estimates the states depending on the measured quantities. This involves coupling two filters in order to be able to simultaneously estimate the states, namely SOC and SOH, that evolve on different timescales and influence each other. The algorithm was developed with synthetic data of which the states are known and subsequently validated with the in-flight data. We then applied the algorithm to evaluate different degradation models. We used the state correction of the algorithm together with the error between simulation and measured values as an indicator for the correctness of the model. The mutli-timescale algorithm is able to reliably estimate both the SOC and the SOH. It is a helpful tool to validate the models.

There are several possible adaptations for the approach developed here. When considering the model for a comprehensive simulation of battery behavior and aging, it would be interesting to include other degradation mechanisms, such as particle cracking. The coupling of these is described, for example, in Ref. [68]. This could better describe the accelerated aging that is observed at later points in the battery life. In addition, features were discovered in the satellite data that indicate plating [63]. These also occurred at a later point in time and could be verified by including for example the plating model of Hein et al. [38]. Moreover, the estimation of the SOH could be extended based on this.

In order to model a larger range of aging, the in-flight data could be processed over an even longer period of time. However, this would require more complex data analysis and more background information on the cycling of the satellite batteries.

There are also several approaches for state estimation that could be investigated further. In this work, the Extended Kalman Filter (EKF) was used. Other filters, such as the Particle Filter or Unscented Kalman Filter, can also be used for nonlinear systems. It would be interesting to compare their performance with that of the EKF and investigate whether they deliver even better results, cf. Refs. [75, 106, 47].

In sec. 5.3, we described how the Kalman gain correction can be used to evaluate the accuracy of the degradation model. Here, it would be conceivable on the one hand to extend the model used, in particular the degradation model, in order to achieve greater reliability. It would also be interesting to use this method to check the cell model and its parameters. Furthermore, one could investigate how the Kalman gain correction of the SOC filter behaves and whether information on the cell model can be obtained from this.

Finally, the methods and algorithms were developed based on satellite applications. It would be a valuable addition to validate the methods using other battery data. In particular, other cycling protocols than those for LEO satellites could provide interesting insights. With that, the methods and algorithms can easily be applied to other applications, such as electric vehicles or any devices that require sophisticated battery management.

A REIMEI Batteries

Table A.1: Specifications of Li-ion pouch cell used in satellite REIMEI, cf. [19, 105].

Cell Chemistry	
Positive active material	$Li_xMn_2O_4$-based
Positive current collector material	Al
Negative active material	Graphite-based
Negative current collector material	Cu
Electrolyte	1 M $LiPF_6$ EC/DEC (3:7 by wt%)+additives
Cell Dimensions	
Rated capacity	3 Ah
Weight	75 g
Dimension	145 mm x 80 mm x 4 mm
Specific energy	158 Wh kg^{-1}
Energy density	340 Wh L^{-1}
Voltage Range	
Charge voltage	4.1 V (4.2 V)
Lower voltage limit	3.0 V

Table A.2: Specifications of Li-ion batteries used in satellite REIMEI, cf. [19, 105].

Configuration	14 Cells (7 series, 2 parallel)
Potting material	Epoxy resin
Case material	Al
Dimension	168 mm x 102 mm x 99 mm
Weight	2.42 kg
Specific energy	70 Wh kg^{-1}

Table A.3: Solar eclipses between 2005 and 2011. From Ref. [1].

Date	Total Solar Eclipse	Partial Solar Eclipse	Visibility in Data
2005-10-03	x		no
2006-03-29	x		yes
2006-09-22	x		yes
2007-03-19		x	yes
2007-09-11		x	no
2008-02-07	x		yes
2008-08-01	x		no
2009-01-26	x		no
2009-07-21/22	x		no*
2010-01-15	x		no*
2010-07-11	x		no*
2011-01-04		x	no*
2011-06-01		x	no*
2011-07-01		x	no
2011-11-25		x	no*

B Model Parameter

OCV Curves. The OCV curves are fitted to the half cell measurements of Brown et al. [20] and are also stated in Ref. [15]. They are SOC dependent with $\mathrm{SOC} = c_\mathrm{s}/c_{\mathrm{s,max}}$. For the anode we get

$$\begin{aligned} U_{0,\mathrm{anode}} = \; & 254.5443 - 0.02525 \cdot \mathrm{SOC} \\ & - 254.273365 \cdot \tanh((\mathrm{SOC} + 0.0097) \cdot 319.5) \\ & - 0.3086345 \cdot \tanh((\mathrm{SOC} - 0.0199) \cdot 47.0) \\ & - 0.025 \cdot \tanh((\mathrm{SOC} - 0.1414) \cdot 27.52) \\ & - 0.015 \cdot \tanh((\mathrm{SOC} - 0.2275) \cdot 18.36) \\ & - 0.1978 \cdot \tanh((\mathrm{SOC} - 1.0444) \cdot 14.43) \\ & - 0.0155 \cdot \tanh((\mathrm{SOC} - 0.56616) \cdot 12.625). \end{aligned} \tag{B.1}$$

For the cathode we get

$$\begin{aligned} U_{0,\mathrm{cathode}} = \; & 289.99 - 336.28 \cdot \mathrm{SOC} \\ & - 164.73 \cdot \tanh((\mathrm{SOC} + 0.5302) \cdot 6.824) \\ & - 0.0768 \cdot \tanh((\mathrm{SOC} - 0.442) \cdot 7.617) \\ & - 0.171 \cdot \tanh((\mathrm{SOC} - 0.9051) \cdot 13.16) \\ & - 0.3126 \cdot \tanh((\mathrm{SOC} - 0.9908) \cdot 96.14) \\ & + 3896.375 \cdot \tanh((\mathrm{SOC} - 0.36182) \cdot 0.08632). \end{aligned} \tag{B.2}$$

For the simulations in chapter 5, the OCV curve of the anode was slightly adapted to ensure a robust filtering behavior. It is given as

$$\begin{aligned} U_{0,\mathrm{anode}} = \; & 53.562 - 0.025 \cdot \mathrm{SOC} \\ & - 254.273365 \cdot \tanh((\mathrm{SOC} + 0.0097) \cdot 319.5) \\ & - 0.3086345 \cdot \tanh((\mathrm{SOC} - 0.0199) \cdot 47.0) \\ & - 0.025 \cdot \tanh((\mathrm{SOC} - 0.1414) \cdot 27.52) \\ & - 0.015 \cdot \tanh((\mathrm{SOC} - 0.2275) \cdot 18.36) \\ & - 0.18 \cdot \tanh((\mathrm{SOC} - 1.1) \cdot 6.67) \\ & - 0.0155 \cdot \tanh((\mathrm{SOC} - 0.57) \cdot 12.5) \\ & - 201 \cdot \tanh((\mathrm{SOC} - 1.07) \cdot 100). \end{aligned} \tag{B.3}$$

Table B.1: Electrolyte parameters from [29]. Parameters are concentration dependent with concentration c_e given in units of mol/L. From Bolay et al. [15].

Parameter	Description	Value	Unit
D_e	Binary diffusion coefficient	$2.84 \cdot 10^{-10} \cdot \exp(-0.45 \cdot c_\mathrm{e})$	$\mathrm{m^2 s^{-1}}$
t_+	Transference number	$0.4 + 0.2 \cdot c_\mathrm{e} - 0.125 \cdot c_\mathrm{e}^2$	1
κ	Conductivity	$(3.4 \cdot c_\mathrm{e} - 4.7 \cdot c_\mathrm{e}^{\frac{3}{2}} + 2 \cdot c_\mathrm{e}^2) \cdot (1 + 0.2 \cdot c_\mathrm{e}^4)^{-1}$	$\mathrm{Sm^{-1}}$

Table B.2: Parameters of P2D model. From Bolay et al. [15].

Parameter	Description	Anode	Cathode	Sep.	Unit	Source
L	Thickness	45.5	74.5	30	10^{-6} m	CT data
ε	Porosity	0.4	0.4	0.5	1	CT data
τ	Tortuosity	2.6	2.6	2.6	1	assumed
A_{spec}	Specific surface area of electrode particle	3.03	2.14		10^5 m^{2}m^{-3}	CT data
$c_{\mathrm{s,max}}$	Maximum Li concentration	3.161	2.6		10^4 mol m^{-3}	fit
D_{s}	Diffusion coefficient of Li in electrode	10	1.13		10^{-13} m^{2}s^{-1}	fit
k	Rate constant in Butler-Volmer term	59.2	4.48		$10^{-7}\cdot$ A m$^{5/2}$ mol$^{-3/2}$	fit
$\mathrm{SOC}_{\mathrm{C,0}}$	Initial SOC of anode	98			%	fit
$\mathrm{SOC}_{\mathrm{LMO,0}}$	Initial SOC of cathode		25		%	assumed

Table B.3: Parameters of 3D simulations. From Bolay et al. [15].

Parameter	Description	Anode	Cathode	Unit
L	Thickness	50	58	10^{-6} m
ε	Porosity	0.4883	0.3658	1
A_{spec}	Specific surface area of electrode particle	2.5	2.19	10^{5} $\mathrm{m}^2\mathrm{m}^{-3}$
$c_{\mathrm{s,max}}$	Maximum Li concentration	3.375	3.16	10^{4} mol m^{-3}
D_{s}	Diffusion coefficient of Li in electrode	10	1.13	10^{-13} $\mathrm{m}^2\mathrm{s}^{-1}$
k	Rate constant in Butler-Volmer term	59.2	4.48	$10^{-7}\cdot$ A $\mathrm{m}^{5/2}$ $\mathrm{mol}^{-3/2}$
SOC_0	Initial SOC	95	22	%

Table B.4: Parameters of degradation model. From Bolay et al. [15].

Parameter	Description	Value	Unit	Source
V_{SEI}	Mean partial molar volume of the SEI	$95.86\cdot10^{-6}$	$\mathrm{m}^3\mathrm{mol}^{-1}$	[94]
$c_0^{e^-}$	Interstitial concentration	$1.5\cdot10^{-2}$	mol m^{-3}	[94]
s_{SEI}	Stoichiometric coefficient	2	1	[94]
$L_{\mathrm{SEI,0}}$	Initial SEI thickness	$10\cdot10^{-9}$	m	fit
D^{e^-}	Diffusion coefficient of Li-interstitials	$1.6\cdot10^{-12}$	$\mathrm{m}^2\mathrm{s}^{-1}$	fit
$\kappa_{\mathrm{SEI}}^{\mathrm{Li}^+}$	Conductivity of Li-ions in SEI	$1\cdot10^{-5}$	S m^{-1}	fit

C MTS Algorithm Test Results

In this chapter, we show additional results of the MTS algorithm, which we tested with in-flight and synthetic data to calibrate the filter parameters.

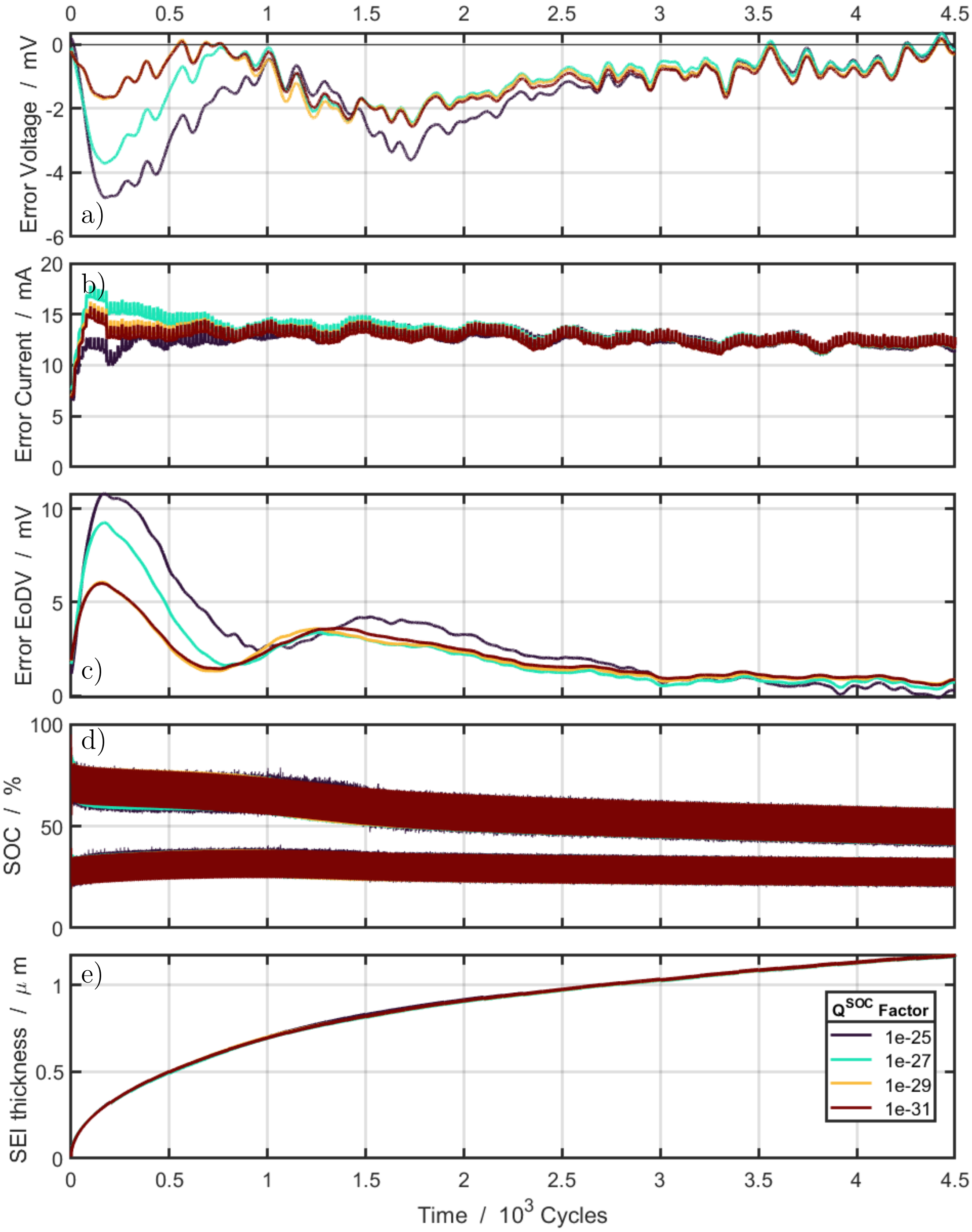

Figure C.1: Comparison of filtering behavior for different process covariance matrices Q^{SOC} for synthetic data. a) Error of cell voltage. b) Error of cell current. c) Error of EoDV. d) Trend of SOC of anode and cathode. e) Trend of SEI thickness.

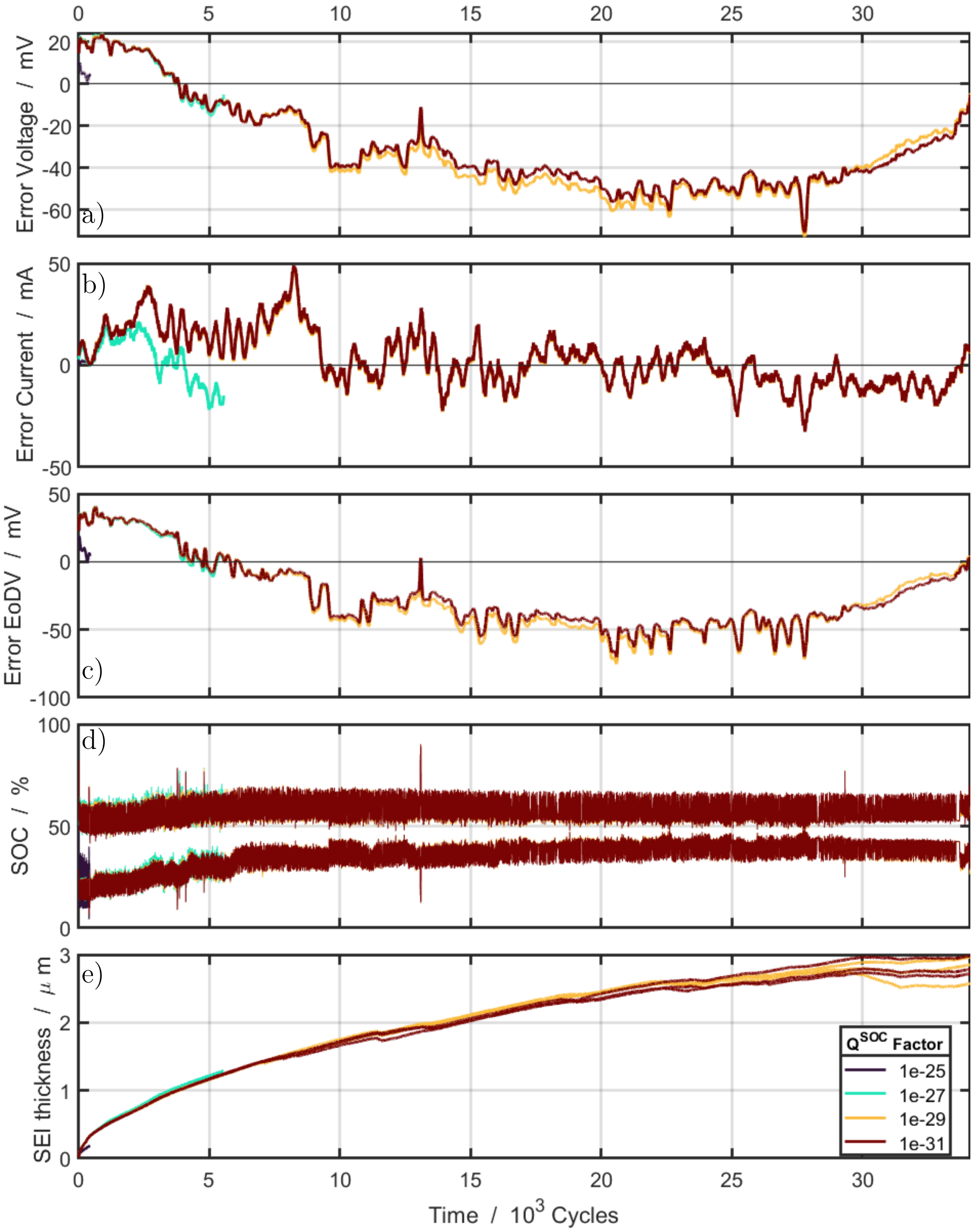

Figure C.2: Comparison of filtering behavior for different process covariance matrices Q^{SOC} for inflight data. a) Error of cell voltage. b) Error of cell current. c) Error of EoDV. d) Trend of SOC of anode and cathode. e) Trend of SEI thickness.

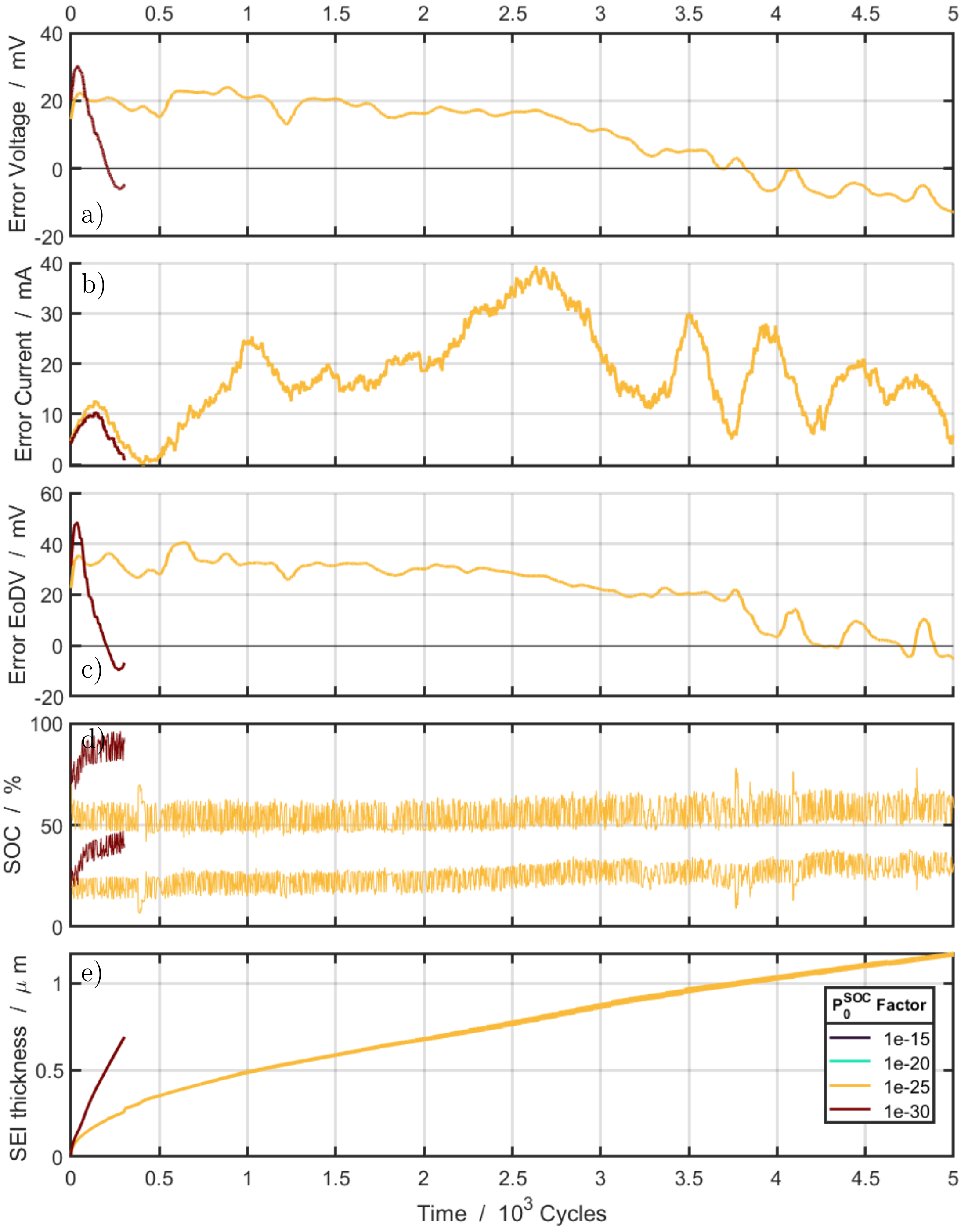

Figure C.3: Comparison of filtering behavior for different process covariance matrices P_0^{SOC} for inflight data. a) Error of cell voltage. b) Error of cell current. c) Error of EoDV. d) Trend of SOC of anode and cathode. e) Trend of SEI thickness.

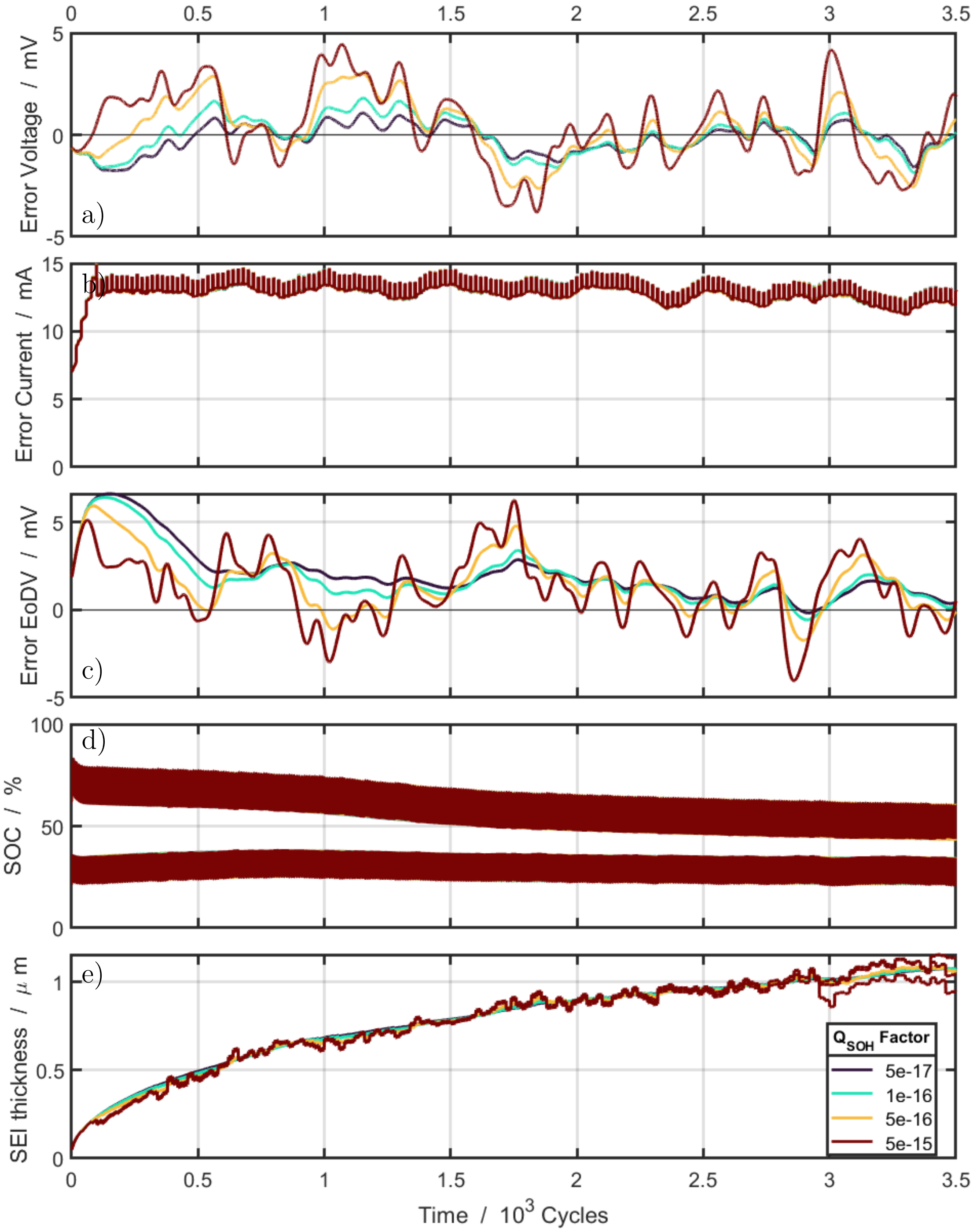

Figure C.4: Comparison of filtering behavior for different process covariance matrices Q^{SOH} for synthetic data. a) Error of cell voltage. b) Error of cell current. c) Error of EoDV. d) Trend of SOC of anode and cathode. e) Trend of SEI thickness.

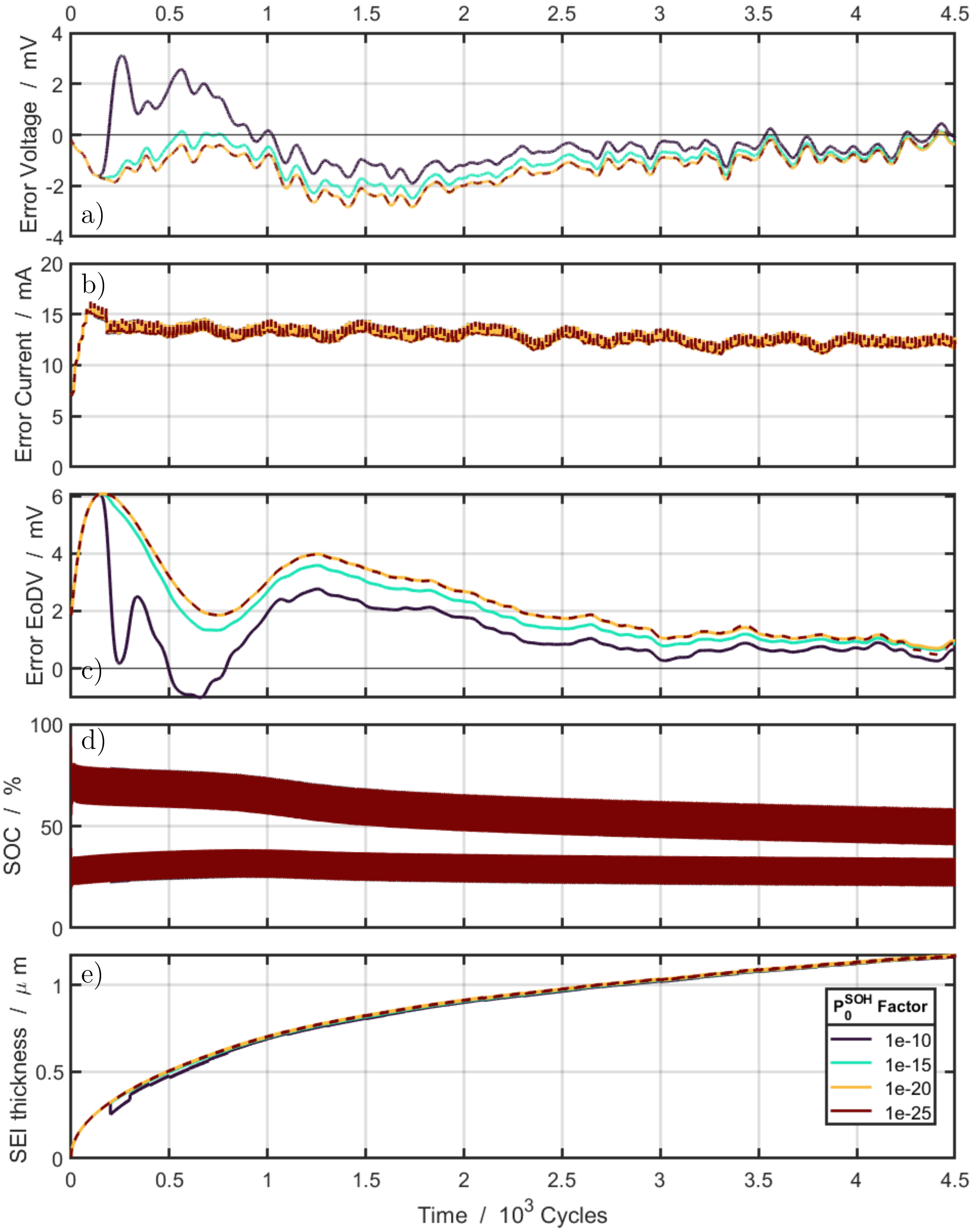

Figure C.5: Comparison of filtering behavior for different process covariance matrices P_0^{SOH} for synthetic data. a) Error of cell voltage. b) Error of cell current. c) Error of EoDV. d) Trend of SOC of anode and cathode. e) Trend of SEI thickness.

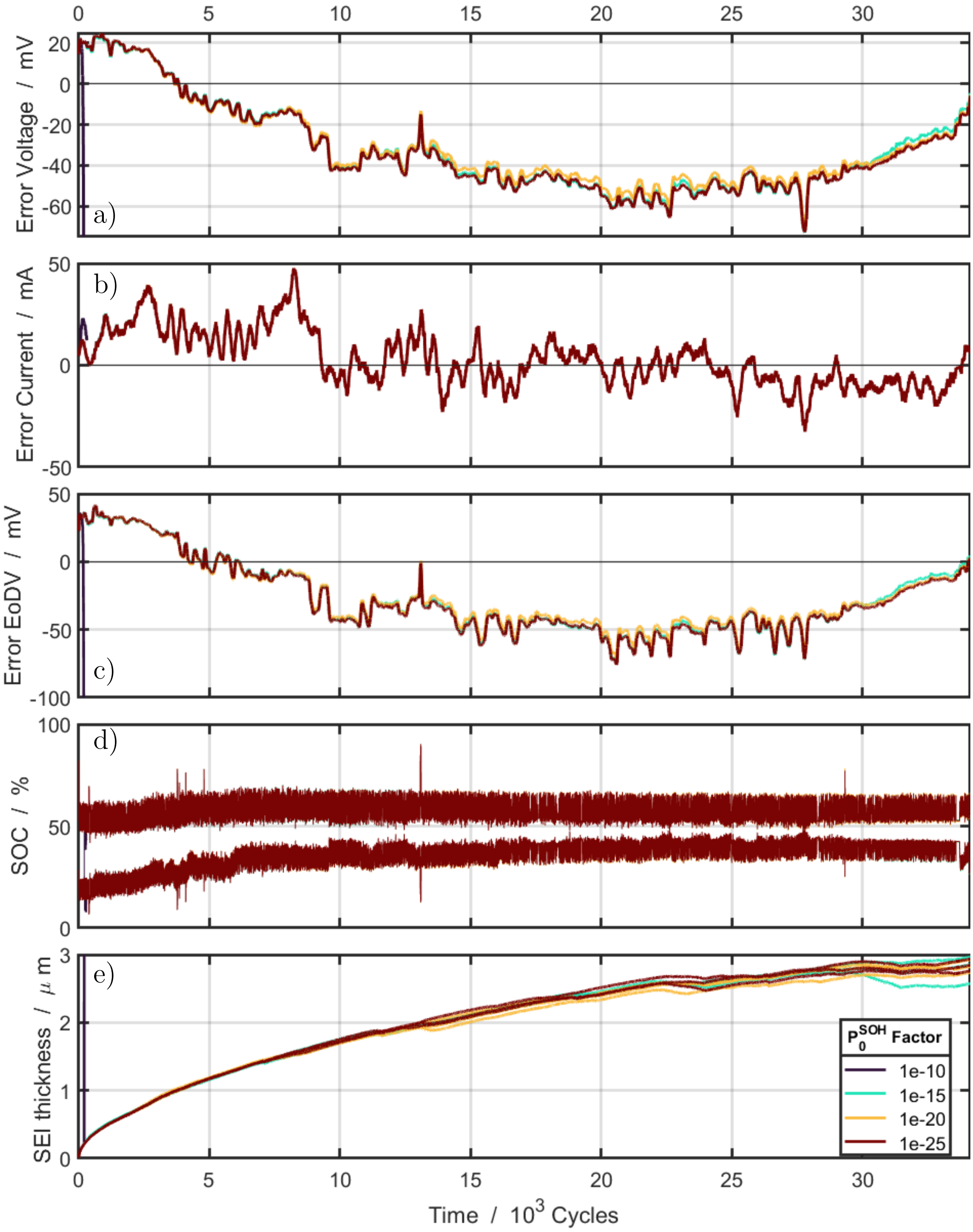

Figure C.6: Comparison of filtering behavior for different process covariance matrices P_0^{SOH} for inflight data. a) Error of cell voltage. b) Error of cell current. c) Error of EoDV. d) Trend of SOC of anode and cathode. e) Trend of SEI thickness.

Bibliography

[1] *Sonnenfinsternis und Mondfinsternis Weltweit.* `https://www.timeanddate.de/finsternis/alle?starty=2000`

[2] Aitio, Antti ; Howey, David A.: Predicting battery end of life from solar off-grid system field data using machine learning. In: *Joule* 5 (2021), Nr. 12, S. 3204–3220. `http://dx.doi.org/10.1016/j.joule.2021.11.006`. – DOI 10.1016/j.joule.2021.11.006. – ISSN 25424351

[3] Andre, Dave ; Appel, Christian ; Soczka-Guth, Thomas ; Sauer, Dirk U.: Advanced mathematical methods of SOC and SOH estimation for lithium-ion batteries. In: *Journal of Power Sources* 224 (2013), S. 20–27. `http://dx.doi.org/10.1016/j.jpowsour.2012.10.001`. – DOI 10.1016/j.jpowsour.2012.10.001. – ISBN 0378–7753

[4] Andrea, Davide: *Battery Management Systems for Large Lithium-Ion Battery Packs.* Norwood (MA) : Artech house, 2010. – ISBN 9781608071043

[5] Attia, Peter M. ; Das, Supratim ; Harris, Stephen J. ; Bazant, Martin Z. ; Chueh, William C.: Electrochemical kinetics of sei growth on Carbon Black: Part I. experiments. In: *Journal of the Electrochemical Society* 166 (2019), Nr. 4, S. E97–E106. `http://dx.doi.org/10.1149/2.0231904jes`. – DOI 10.1149/2.0231904jes. – ISSN 19457111

[6] Aung, Htet ; Soon, Jing J. ; Goh, Shu T. ; Lew, Jia M. ; Low, Kay S.: Battery Management System with State-of-Charge and Opportunistic State-of-Health for a Miniaturized Satellite. In: *IEEE Transactions on Aerospace and Electronic Systems* 56 (2019), Nr. 4, S. 2978–2989. `http://dx.doi.org/10.1109/TAES.2019.2958161`. – DOI 10.1109/TAES.2019.2958161. – ISSN 15579603

[7] Barde, Henri: 1989-2019: Three decades of power systems evolution through the prism of ESPC. In: *2019 European Space Power Conference (ESPC).* Juan-les-Pins, France : IEEE, 2019. – ISBN 9781728121260, S. 1–5

[8] Bearden, David A.: Small-satellite costs. In: *Crosslink* 2 (2001), Nr. 1, 32–44. `http://spacese.spacegrant.org/uploads/Costs/BeardenComplexityCrosslink.pdf`

[9] Becerra, V. M. ; Roberts, P. D. ; Griffiths, G. W.: Applying the extended Kalman filter to systems described by nonlinear differential-algebraic equations. In: *Control Engineering Practice* 9 (2001), Nr. 3, S. 267–281. `http://dx.doi.org/10.1016/S0967-0661(00)00110-6`. – DOI 10.1016/S0967–0661(00)00110–6. – ISSN 09670661

[10] Bertolini, Samuel ; Balbuena, Perla B.: Buildup of the solid electrolyte interphase on lithium-metal anodes: reactive molecular dynamics study. In: *The Journal of Physical Chemistry C* 122 (2018), Nr. 20, S. 10783–10791. `http://dx.doi.org/10.1021/acs.jpcc.8b03046`. – DOI 10.1021/acs.jpcc.8b03046

[11] Bi, Yalan ; Yin, Yilin ; Choe, Song Y.: Online state of health and aging parameter estimation using a physics-based life model with a particle filter. In: *Journal of Power Sources* 476 (2020), Nr. March, S. 228655. `http://dx.doi.org/10.1016/j.jpowsour.2020.228655`. – DOI 10.1016/j.jpowsour.2020.228655. – ISSN 03787753

[12] Birkl, Christoph R. ; Roberts, Matthew R. ; McTurk, Euan ; Bruce, Peter G. ; Howey, David A.: Degradation diagnostics for lithium ion cells. In: *Journal of Power Sources* 341 (2017), S. 373–386. `http://dx.doi.org/10.1016/j.jpowsour.2016.12.011`. – DOI 10.1016/j.jpowsour.2016.12.011. – ISSN 03787753

[13] Bizeray, Adrien M. ; Kim, Jin H. ; Duncan, Stephen R. ; Howey, David A.: Identifiability and Parameter Estimation of the Single Particle Lithium-Ion Battery Model. In: *IEEE Transactions on Control Systems Technology* 27 (2019), Nr. 5, S. 1862–1877. `http://dx.doi.org/10.1109/TCST.2018.2838097`. – DOI 10.1109/TCST.2018.2838097. – ISSN 1558–0865

[14] Bizeray, Adrien M. ; Zhao, S. ; Duncan, Stephen R. ; Howey, David A.: Lithium-ion battery thermal-electrochemical model-based state estimation using orthogonal collocation and a modified extended Kalman filter. In: *Journal of Power Sources* 296 (2015), S. 400–412. `http://dx.doi.org/10.1016/j.jpowsour.2015.07.019`. – DOI 10.1016/j.jpowsour.2015.07.019. – ISBN 0378–7753

[15] Bolay, Linda J. ; Schmitt, Tobias ; Hein, Simon ; Mendoza-Hernandez, Omar S. ; Hosono, Eiji ; Asakura, Daisuke ; Kinoshita, Koichi ; Matsuda, Hirofumi ; Umeda, Minoru ; Sone, Yoshitsugu ; Latz, Arnulf ; Horstmann, Birger: Microstructure-Resolved Degradation Simulation of Lithium-Ion Batteries in Space Applications. In: *Journal of Power Sources Advances* 14 (2022), S. 100083. `http://dx.doi.org/10.1016/j.powera.2022.100083`. – DOI 10.1016/j.powera.2022.100083. – ISSN 26662485

[16] Boniface, Maxime ; Quazuguel, Lucille ; Danet, Julien ; Guyomard, Dominique ; Moreau, Philippe ; Bayle-Guillemaud, Pascale: Nanoscale Chemical Evolution of Silicon Negative Electrodes Characterized by Low-Loss STEM-EELS. In: *Nano Letters* 16 (2016), Nr. 12, S. 7381–7388. `http://dx.doi.org/10.1021/acs.nanolett.6b02883`. – DOI 10.1021/acs.nanolett.6b02883. – ISSN 15306992

[17] Botte, Gerardine G. ; Subramanian, Venkat R. ; White, Ralph E.: Mathematical modeling of secondary lithium batteries. In: *Electrochimica Acta* 45 (2000), Nr. 15-16, S. 2595–2609. `http://dx.doi.org/10.1016/S0013-4686(00)00340-6`. – DOI 10.1016/S0013–4686(00)00340–6. – ISSN 00134686

[18] Brown, Shelley: *Diagnosis of the Lifetime Performance Degradation of Lithium-Ion Batteries (PhD thesis)*, KTH Royal Institute of Technology, Diss., 2008. – 142 S

[19] Brown, Shelley ; Ogawa, Keita ; Kumeuchi, Youichi ; Enomoto, Shinsuke ; Uno, Masatoshi ; Saito, Hirobumi ; Sone, Yoshitsugu ; Abraham, Daniel ; Lindbergh, Göran: Cycle life evaluation of 3 Ah LixMn2O4-based lithium-ion secondary cells for low-earth-orbit satellites. I. Full cell results. In: *Journal of Power Sources* 185 (2008), Nr. 2, S. 1444–1453. `http://dx.doi.org/10.1016/j.jpowsour.2008.07.070`. – DOI 10.1016/j.jpowsour.2008.07.070. – ISBN 0378–7753

[20] Brown, Shelley ; Ogawa, Keita ; Kumeuchi, Youichi ; Enomoto, Shinsuke ; Uno, Masatoshi ; Saito, Hirobumi ; Sone, Yoshitsugu ; Abraham, Daniel ; Lindbergh, Göran: Cycle life evaluation of 3 Ah LixMn2O4-based lithium-ion secondary cells for low-earth-orbit satellites. II. Harvested electrode examination. In: *Journal of Power Sources* 185 (2008), Nr. 2, S. 1454–1464. `http://dx.doi.org/10.1016/j.jpowsour.2008.07.071`. – DOI 10.1016/j.jpowsour.2008.07.071. – ISBN 0378–7753

[21] Campestrini, Christian ; Heil, Thomas ; Kosch, Stephan ; Jossen, Andreas: A comparative study and review of different Kalman filters by applying an enhanced validation method. In: *Journal of Energy Storage* 8 (2016), S. 142–159. `http://dx.doi.org/10.1016/j.est.2016.10.004`. – DOI 10.1016/j.est.2016.10.004. – ISSN 2352152X

[22] Chapel, Lorenzo ; Picot, Antoine ; Lacressonniere, Fabien ; Maussion, Pascal: Contribution to a review of lithium-ion batteries diagnostic methods for space applications. In: *Proceedings of the 2023 IEEE 14th International Symposium on Diagnostics for Electrical Machines, Power Electronics and Drives, SDEMPED 2023* (2023), Nr. 1998, S. 63–69. `http://dx.doi.org/10.1109/SDEMPED54949.2023.10271478`. – DOI 10.1109/SDEMPED54949.2023.10271478. ISBN 9798350320770

[23] Chen, Chang-Hui ; Brosa Planella, Ferran ; O'Regan, Kieran ; Gastol, Dominika ; Widanage, W. D. ; Kendrick, Emma: Development of Experimental Techniques for Parameterization of Multi-scale Lithium-ion Battery Models. In: *Journal of The Electrochemical Society* 167 (2020), Nr. 8, S. 080534. `http://dx.doi.org/10.1149/1945-7111/ab9050`. – DOI 10.1149/1945–7111/ab9050. – ISSN 0013–4651

[24] Chouchane, Mehdi ; Arcelus, Oier ; Franco, Alejandro A.: Heterogeneous Solid-Electrolyte Interphase in Graphite Electrodes Assessed by 4D-Resolved Computational Simulations. In: *Batteries & Supercaps* 4 (2021), Nr. 9, S. 1457–1463. `http://dx.doi.org/10.1002/batt.202100030`. – DOI 10.1002/batt.202100030

[25] Damiano, Alfonso ; Porru, Mario ; Salimbeni, Andrea ; Serpi, Alessandro ; Castiglia, Vincenzo ; Di Tommaso, Antonino O. ; Miceli, Rosario ; Schettino, Giuseppe: Batteries for Aerospace: A Brief Review. In: *2018 AEIT International Annual Conference*. Bari, Italy : IEEE, 2018. – ISBN 9788887237405, S. 1–6

[26] Das, Supratim ; Attia, Peter M. ; Chueh, William C. ; Bazant, Martin Z.: Electrochemical kinetics of sei growth on carbon black: Part II. Modeling. In: *Journal of the Electrochemical Society* 166 (2019), Nr. 4, S. E107–E118. `http://dx.doi.org/10.1149/2.0241904jes`. – DOI 10.1149/2.0241904jes. – ISSN 19457111

[27] Doyle, Marc ; Fuller, Thomas F. ; Newman, John: Modeling of Galvanostatic Charge and Discharge of the Lithium/Polymer/Insertion Cell.

In: *Journal of The Electrochemical Society* 140 (1993), Nr. 6, S. 1526–1533. `http://dx.doi.org/10.1149/1.2221597`. – DOI 10.1149/1.2221597. – ISBN 0013–4651

[28] DUDZINSKI, Leonard A. ; HAMLEY, John A. ; MCCALLUM, Peter W. ; SUTLIFF, Thomas J. ; ZAKRAJSEK, June F.: NASA's radioisotope power systems program status. In: *12th International Energy Conversion Engineering Conference*. Cleveland, OH, USA, 2014, S. 3462

[29] EHRL, Andreas ; LANDESFEIND, Johannes ; WALL, Wolfgang A. ; GASTEIGER, Hubert A.: Determination of Transport Parameters in Liquid Binary Lithium Ion Battery Electrolytes. In: *Journal of The Electrochemical Society* 164 (2017), Nr. 4, S. A826–A836. `http://dx.doi.org/10.1149/2.1131704jes`. – DOI 10.1149/2.1131704jes. – ISBN 0013–4651 1945–7111

[30] EKSTRÖM, Henrik ; LINDBERGH, Göran: A Model for Predicting Capacity Fade due to SEI Formation in a Commercial Graphite/LiFePO 4 Cell . In: *Journal of The Electrochemical Society* 162 (2015), Nr. 6, S. A1003–A1007. `http://dx.doi.org/10.1149/2.0641506jes`. – DOI 10.1149/2.0641506jes. – ISSN 0013–4651

[31] FORMAN, Joel C. ; MOURA, Scott J. ; STEIN, Jeffrey L. ; FATHY, Hosam K.: Genetic identification and fisher identifiability analysis of the Doyle-Fuller-Newman model from experimental cycling of a LiFePO 4 cell. In: *Journal of Power Sources* 210 (2012), S. 263–275. `http://dx.doi.org/10.1016/j.jpowsour.2012.03.009`. – DOI 10.1016/j.jpowsour.2012.03.009. – ISSN 03787753

[32] FULLER, Thomas F. ; DOYLE, Marc ; NEWMAN, John: Simulation and Optimization of the Dual Lithium Ion Insertion Cell. In: *Journal of The Electrochemical Society* 141 (1994), Nr. 1, S. 1. `http://dx.doi.org/10.1149/1.2054684`. – DOI 10.1149/1.2054684. – ISBN 0013–4651

[33] GROOT, Jens ; SWIERCZYNSKI, Maciej ; STAN, Ana I. ; KÆR, Søren K.: On the complex ageing characteristics of high-power LiFePO4/graphite battery cells cycled with high charge and discharge currents. In: *Journal of Power Sources* 286 (2015), S. 475–487. `http://dx.doi.org/10.1016/j.jpowsour.2015.04.001`. – DOI 10.1016/j.jpowsour.2015.04.001. – ISSN 03787753

[34] HALPERT, Gerald ; FRANK, Harvey ; SURAMPUDI, Subbarao: Batteries

and fuel cells in space. In: *The Electrochemical Society Interface* 8 (1999), Nr. 3, S. 25–30. – ISSN 1064–8208

[35] Hannan, M. A. ; Lipu, M. S. ; Hussain, A. ; Mohamed, A.: A review of lithium-ion battery state of charge estimation and management system in electric vehicle applications: Challenges and recommendations. In: *Renewable and Sustainable Energy Reviews* 78 (2017), Nr. August 2016, S. 834–854. `http://dx.doi.org/10.1016/j.rser.2017.05.001`. – DOI 10.1016/j.rser.2017.05.001. – ISBN 978–1–4799–5680–7

[36] Hein, Simon: *Modeling of lithium plating in lithium-ion-batteries*, Ulm University, Ph.D. thesis, 2017. `https://oparu.uni-ulm.de/xmlui/handle/123456789/7996`

[37] Hein, Simon ; Feinauer, Julian ; Westhoff, Daniel ; Manke, Ingo ; Schmidt, Volker ; Latz, Arnulf: Stochastic microstructure modeling and electrochemical simulation of lithium-ion cell anodes in 3D. In: *Journal of Power Sources* 336 (2016), S. 161–171. `http://dx.doi.org/10.1016/j.jpowsour.2016.10.057`. – DOI 10.1016/j.jpowsour.2016.10.057. – ISSN 03787753

[38] Hein, Simon ; Latz, Arnulf: Influence of local lithium metal deposition in 3D microstructures on local and global behavior of Lithium-ion batteries. In: *Electrochimica Acta* 201 (2016), S. 354–365. `http://dx.doi.org/10.1016/j.electacta.2016.01.220`. – DOI 10.1016/j.electacta.2016.01.220. – ISBN 00134686

[39] Heinrich, Marco ; Wolff, Nicolas ; Harting, Nina ; Laue, Vincent ; Röder, Fridolin ; Seitz, Steffen ; Krewer, Ulrike: Physico-Chemical Modeling of a Lithium-Ion Battery: An Ageing Study with Electrochemical Impedance Spectroscopy. In: *Batteries and Supercaps* 2 (2019), Nr. 6, S. 530–540. `http://dx.doi.org/10.1002/batt.201900011`. – DOI 10.1002/batt.201900011. – ISBN 5313915932

[40] Horstmann, Birger ; Single, Fabian ; Latz, Arnulf: Review on multiscale models of solid-electrolyte interphase formation. In: *Current Opinion in Electrochemistry* 13 (2019), S. 61–69. `http://dx.doi.org/10.1016/j.coelec.2018.10.013`. – DOI 10.1016/j.coelec.2018.10.013. – ISSN 24519111

[41] Hu, Chao ; Youn, Byeng D. ; Chung, Jaesik: A multiscale framework with extended Kalman filter for lithium-ion battery SOC and capacity estimation. In: *Applied Energy* 92 (2012), S. 694–704. `http://dx.doi.org/10.1016/`

j.apenergy.2011.08.002. – DOI 10.1016/j.apenergy.2011.08.002. – ISSN 03062619

[42] Huang, William ; Attia, Peter M. ; Wang, Hansen ; Renfrew, Sara E. ; Jin, Norman ; Das, Supratim ; Zhang, Zewen ; Boyle, David T. ; Li, Yuzhang ; Bazant, Martin Z. ; McCloskey, Bryan D. ; Chueh, William C. ; Cui, Yi: Evolution of the Solid-Electrolyte Interphase on Carbonaceous Anodes Visualized by Atomic-Resolution Cryogenic Electron Microscopy. In: *Nano Letters* 19 (2019), Nr. 8, S. 5140–5148. `http://dx.doi.org/10.1021/acs.nanolett.9b01515`. – DOI 10.1021/acs.nanolett.9b01515. – ISSN 15306992

[43] ITWM: *BEST - Battery and Electrochemistry Simulation Tool*. `http://itwm.fraunhofer.de/best`, 2020

[44] Jokar, Ali ; Rajabloo, Barzin ; Désilets, Martin ; Lacroix, Marcel: Review of simplified Pseudo-two-Dimensional models of lithium-ion batteries. In: *Journal of Power Sources* 327 (2016), S. 44–55. `http://dx.doi.org/10.1016/j.jpowsour.2016.07.036`. – DOI 10.1016/j.jpowsour.2016.07.036. – ISBN 0378–7753

[45] Jun, Myungsoo ; Smith, Kandler A. ; Wood, Eric ; Smart, Marshall C.: Battery capacity estimation of low-earth orbit satellite application. In: *International Journal of Prognostics and Health Management* 3 (2012), Nr. 2, S. 81–89. `http://dx.doi.org/10.36001/ijphm.2012.v3i2.1366`. – DOI 10.36001/ijphm.2012.v3i2.1366. – ISSN 21532648

[46] Keil, Jonas ; Paul, Neelima ; Baran, Volodymyr ; Keil, Peter ; Gilles, Ralph ; Jossen, Andreas: Linear and Nonlinear Aging of Lithium-Ion Cells Investigated by Electrochemical Analysis and In-Situ Neutron Diffraction. In: *Journal of The Electrochemical Society* 166 (2019), Nr. 16, S. A3908–A3917. `http://dx.doi.org/10.1149/2.1271915jes`. – DOI 10.1149/2.1271915jes

[47] Klee Barillas, Joaquín ; Li, Jiahao ; Günther, Clemens ; Danzer, Michael A.: A comparative study and validation of state estimation algorithms for Li-ion batteries in battery management systems. In: *Applied Energy* 155 (2015), S. 455–462. `http://dx.doi.org/10.1016/j.apenergy.2015.05.102`. – DOI 10.1016/j.apenergy.2015.05.102. – ISSN 03062619

[48] Kolzenberg, Lars von ; Latz, Arnulf ; Horstmann, Birger: Solid–Electrolyte Interphase During Battery Cycling: Theory of Growth

Regimes. In: *ChemSusChem* 13 (2020), Nr. 15, S. 3901–3910. `http://dx.doi.org/10.1002/cssc.202000867`. – DOI 10.1002/cssc.202000867. – ISSN 1864564X

[49] Latz, Arnulf ; Zausch, Jochen: Thermodynamic consistent transport theory of Li-ion batteries. In: *Journal of Power Sources* 196 (2011), Nr. 6, S. 3296–3302. `http://dx.doi.org/10.1016/j.jpowsour.2010.11.088`. – DOI 10.1016/j.jpowsour.2010.11.088. – ISBN 0378–7753

[50] Latz, Arnulf ; Zausch, Jochen: Multiscale modeling of lithium ion batteries: Thermal aspects. In: *Beilstein Journal of Nanotechnology* 6 (2015), Nr. 1, S. 987–1007. `http://dx.doi.org/10.3762/bjnano.6.102`. – DOI 10.3762/bjnano.6.102. – ISBN 2190–4286

[51] Li, Dongjiang ; Danilov, Dmitry ; Zhang, Zhongru ; Chen, Huixin ; Yang, Yong ; Notten, Peter H. L.: Modeling the SEI-Formation on Graphite Electrodes in LiFePO4 Batteries. In: *Journal of The Electrochemical Society* 162 (2015), Nr. 6, S. A858–A869. `http://dx.doi.org/10.1149/2.0161506jes`. – DOI 10.1149/2.0161506jes. – ISSN 0013–4651

[52] Li, Jiahao ; Klee Barillas, Joaquin ; Guenther, Clemens ; Danzer, Michael A.: A comparative study of state of charge estimation algorithms for LiFePO4 batteries used in electric vehicles. In: *Journal of Power Sources* 230 (2013), S. 244–250. `http://dx.doi.org/10.1016/j.jpowsour.2012.12.057`. – DOI 10.1016/j.jpowsour.2012.12.057. – ISSN 03787753

[53] Li, Weihan ; Cao, Decheng ; Jöst, Dominik ; Ringbeck, Florian ; Kuipers, Matthias ; Frie, Fabian ; Sauer, Dirk U.: Parameter sensitivity analysis of electrochemical model-based battery management systems for lithium-ion batteries. In: *Applied Energy* 269 (2020), S. 115104. `http://dx.doi.org/10.1016/j.apenergy.2020.115104`. – DOI 10.1016/j.apenergy.2020.115104. – ISSN 03062619

[54] Li, Weihan ; Chen, Jue ; Quade, Katharina ; Luder, Daniel ; Gong, Jingyu ; Sauer, Dirk U.: Battery degradation diagnosis with field data, impedance-based modeling and artificial intelligence. In: *Energy Storage Materials* 53 (2022), dec, S. 391–403. `http://dx.doi.org/10.1016/J.ENSM.2022.08.021`. – DOI 10.1016/J.ENSM.2022.08.021. – ISSN 2405–8297

[55] Li, Weihan ; Fan, Yue ; Ringbeck, Florian ; Jöst, Dominik ; Han, Xuebing ; Ouyang, Minggao ; Sauer, Dirk U.: Electrochemical

model-based state estimation for lithium-ion batteries with adaptive unscented Kalman filter. In: *Journal of Power Sources* 476 (2020), S. 228534. `http://dx.doi.org/10.1016/j.jpowsour.2020.228534`. – DOI 10.1016/j.jpowsour.2020.228534. – ISSN 03787753

[56] Li, Weihan ; Rentemeister, Monika ; Badeda, Julia ; Jöst, Dominik ; Schulte, Dominik ; Sauer, Dirk U.: Digital twin for battery systems: Cloud battery management system with online state-of-charge and state-of-health estimation. In: *Journal of Energy Storage* 30 (2020), S. 101557. `http://dx.doi.org/10.1016/j.est.2020.101557`. – DOI 10.1016/j.est.2020.101557. – ISSN 2352152X

[57] Li, Weihan ; Sengupta, Neil ; Dechent, Philipp ; Howey, David A. ; Annaswamy, Anuradha ; Sauer, Dirk U.: Online capacity estimation of lithium-ion batteries with deep long short-term memory networks. In: *Journal of Power Sources* 482 (2021), S. 228863. `http://dx.doi.org/10.1016/j.jpowsour.2020.228863`. – DOI 10.1016/j.jpowsour.2020.228863. – ISSN 03787753

[58] Lin, Yu X. ; Liu, Zhe ; Leung, Kevin ; Chen, Long Q. ; Lu, Peng ; Qi, Yue: Connecting the irreversible capacity loss in Li-ion batteries with the electronic insulating properties of solid electrolyte interphase (SEI) components. In: *Journal of Power Sources* 309 (2016), S. 221–230. `http://dx.doi.org/10.1016/j.jpowsour.2016.01.078`. – DOI 10.1016/j.jpowsour.2016.01.078. – ISSN 03787753

[59] Malet, Fabien ; Leconte, Vincent ; Borthomieu, Yannick ; Bauchais, Frédéric: Overview and in-Orbit Behaviour of the First Lithium-Ion Batteries Used Onboard Eutelsat 7a and Eutelsat Hot Bird 13B Geo Telecommunications Satellite. In: *10th European Space Power Conference* Bd. 719. Noordwijkerhout, The Netherlands, 2014, S. 80

[60] Math2Market GmbH (Hrsg.): *GeoDict 2019*. Deutschland: Math2Market GmbH. – `https://www.math2market.com/`

[61] The MathWorks, Inc. (Hrsg.): *MATLAB 2021a*. Natick, Massachusetts: The MathWorks, Inc.. – `https://www.mathworks.com/products/matlab.html`

[62] Mattesco, Patrick ; Thakur, Vijay ; Tricot, H.: Overview and preliminary in orbit behaviour of the first Lithium-ion batteries used onboard

Eutelsat W3A GEO telecommunications satellite mission. In: *7th European Space Power Conference* Bd. 589. Stresa, Italy, 2005. – ISSN 03796566, S. 4

[63] Mendoza-Hernandez, Omar S. ; Bolay, Linda J. ; Horstmann, Birger ; Latz, Arnulf ; Hosono, Eiji ; Asakura, Daisuke ; Matsuda, Hirofumi ; Itagaki, Masayuki ; Umeda, Minoru ; Sone, Yoshitsugu: Durability analysis of the REIMEI Satellite Li-Ion batteries after more than 14 years of operation in space. In: *Electrochemistry* 88 (2020), Nr. 4, S. 300–304. `http://dx.doi.org/10.5796/electrochemistry.20-00046`. – DOI 10.5796/electrochemistry.20–00046. – ISSN 21862451

[64] Mössle, Patrick ; Tietze, Tobias ; Danzer, Michael A.: Kalman Filter Tuning for State Estimation of Lithium-Ion Batteries by Multi-objective Optimization via Hyper Space Exploration. In: *Energy Technology* (2023), S. 2300796. `http://dx.doi.org/10.1002/ente.202300796`. – DOI 10.1002/ente.202300796. – ISSN 2194–4288

[65] Newman, John ; Thomas-Alyea, Karen E.: *Electrochemical Systems 3rd Edition*. John Wiley & Sons, Inc., Hoboken, NJ, USA, 2004. – ISBN 3175723993

[66] Ohser, Joachim ; Mücklich, Frank: *Statistical analysis of microstructures in materials science*. John Wiley & Sons, 2000. – 114–117 S.

[67] Ohser, Joachim ; Schladitz, Katja: *3D images of materials structures: processing and analysis*. John Wiley & Sons, 2009

[68] O'Kane, Simon E. J. ; Ai, Weilong ; Madabattula, Ganesh ; Alvarez, Diego A. ; Timms, Robert ; Sulzer, Valentin ; Edge, Jacqueline S. ; Wu, Billy ; Offer, Gregory J. ; Marinescu, Monica: Lithium-ion battery degradation: how to model it. In: *Phys. Chem. Chem. Phys.* 24 (2022), Nr. 13, S. 7909–7922. `http://dx.doi.org/10.1039/d2cp00417h`. – DOI 10.1039/d2cp00417h. – ISSN 1463–9076

[69] Peng, Jian ; Zhou, Zhongbao ; Wang, Jiongqi ; Wu, Di ; Guo, Yinman: Residual remaining useful life prediction method for lithium-ion batteries in satellite with incomplete healthy historical data. In: *IEEE Access* 7 (2019), S. 127788–127799. `http://dx.doi.org/10.1109/ACCESS.2019.2938060`. – DOI 10.1109/ACCESS.2019.2938060. – ISSN 21693536

[70] Pfrang, A. ; Kersys, A. ; Kriston, A. ; Sauer, Dirk U. ; Rahe, C. ; Käbitz, S. ; Figgemeier, E.: Long-term cycling induced jelly roll deformation in commercial 18650 cells. In: *Journal of Power Sources* 392 (2018), S.

168–175. `http://dx.doi.org/10.1016/j.jpowsour.2018.03.065`. – DOI 10.1016/j.jpowsour.2018.03.065. – ISSN 03787753

[71] Pinson, Matthew B. ; Bazant, Martin Z.: Theory of SEI formation in rechargeable batteries: Capacity fade, accelerated aging and lifetime prediction. In: *Journal of the Electrochemical Society* 160 (2013), Nr. 2, S. A243–A250. `http://dx.doi.org/10.1149/2.044302jes`. – DOI 10.1149/2.044302jes. – ISSN 00134651

[72] Plett, Gregory L.: Extended Kalman filtering for battery management systems of LiPB-based HEV battery packs - Part 1. Background. In: *Journal of Power Sources* 134 (2004), Nr. 2, S. 252–261. `http://dx.doi.org/10.1016/j.jpowsour.2004.02.031`. – DOI 10.1016/j.jpowsour.2004.02.031. – ISBN 0378–7753

[73] Plett, Gregory L.: Extended Kalman filtering for battery management systems of LiPB-based HEV battery packs - Part 2. Modeling and identification. In: *Journal of Power Sources* 134 (2004), Nr. 2, S. 262–276. `http://dx.doi.org/10.1016/j.jpowsour.2004.02.032`. – DOI 10.1016/j.jpowsour.2004.02.032. – ISBN 0378–7753

[74] Plett, Gregory L.: Extended Kalman filtering for battery management systems of LiPB-based HEV battery packs - Part 3. State and parameter estimation. In: *Journal of Power Sources* 134 (2004), Nr. 2, S. 277–292. `http://dx.doi.org/10.1016/j.jpowsour.2004.02.033`. – DOI 10.1016/j.jpowsour.2004.02.033. – ISBN 0378–7753

[75] Plett, Gregory L.: Sigma-point Kalman filtering for battery management systems of LiPB-based HEV battery packs. Part 1: Introduction and state estimation. In: *Journal of Power Sources* 161 (2006), Nr. 2, S. 1356–1368. `http://dx.doi.org/10.1016/j.jpowsour.2006.06.003`. – DOI 10.1016/j.jpowsour.2006.06.003. – ISBN 0378–7753

[76] Plett, Gregory L.: Sigma-point Kalman filtering for battery management systems of LiPB-based HEV battery packs. Part 2: Simultaneous state and parameter estimation. In: *Journal of Power Sources* 161 (2006), Nr. 2, S. 1369–1384. `http://dx.doi.org/10.1016/j.jpowsour.2006.06.004`. – DOI 10.1016/j.jpowsour.2006.06.004. – ISBN 0378–7753

[77] Ploehn, Harry J. ; Ramadass, Premanand ; White, Ralph E.: Solvent Diffusion Model for Aging of Lithium-Ion Battery Cells. In: *Journal of The*

Electrochemical Society 151 (2004), Nr. 3, S. A456–A462. `http://dx.doi.org/10.1149/1.1644601`. – DOI 10.1149/1.1644601. – ISSN 00134651

[78] Prifling, Benedikt ; Ridder, Alexander ; Hilger, André ; Osenberg, Markus ; Manke, Ingo ; Birke, Kai P. ; Schmidt, Volker: Analysis of structural and functional aging of electrodes in lithium-ion batteries during rapid charge and discharge rates using synchrotron tomography. In: *Journal of Power Sources* 443 (2019), S. 227259. `http://dx.doi.org/10.1016/j.jpowsour.2019.227259`. – DOI 10.1016/j.jpowsour.2019.227259. – ISSN 03787753

[79] Rahe, Christiane ; Kelly, Stephen T. ; Rad, Mansoureh N. ; Sauer, Dirk U. ; Mayer, Joachim ; Figgemeier, Egbert: Nanoscale X-ray imaging of ageing in automotive lithium ion battery cells. In: *Journal of Power Sources* 433 (2019), S. 126631. `http://dx.doi.org/10.1016/j.jpowsour.2019.05.039`. – DOI 10.1016/j.jpowsour.2019.05.039. – ISSN 03787753

[80] Rahimian, Saeed K. ; Rayman, Sean ; White, Ralph E.: State of charge and loss of active material estimation of a lithium ion cell under low earth orbit condition using Kalman filtering approaches. In: *Journal of the Electrochemical Society* 159 (2012), Nr. 6, S. A860–A872. `http://dx.doi.org/10.1149/2.098206jes`. – DOI 10.1149/2.098206jes. – ISSN 00134651

[81] Rahman, Ashiqur ; Anwar, Sohel ; Izadian, Afshin: Electrochemical model parameter identification of a lithium-ion battery using particle swarm optimization method. In: *Journal of Power Sources* 307 (2016), S. 86–97. `http://dx.doi.org/10.1016/j.jpowsour.2015.12.083`. – DOI 10.1016/j.jpowsour.2015.12.083. – ISSN 0378–7753

[82] Regis, Rommel G. ; Shoemaker, Christine A.: A Stochastic Radial Basis Function Method for the Global Optimization of Expensive Functions. In: *INFORMS Journal on Computing* 19 (2007), Nr. 4, S. 497–509. `http://dx.doi.org/10.1287/ijoc.1060.0182`. – DOI 10.1287/ijoc.1060.0182

[83] Reniers, Jorn M. ; Mulder, Grietus ; Howey, David A.: Review and Performance Comparison of Mechanical-Chemical Degradation Models for Lithium-Ion Batteries. In: *Journal of The Electrochemical Society* 166 (2019), Nr. 14, S. A3189–A3200. `http://dx.doi.org/10.1149/2.0281914jes`. – DOI 10.1149/2.0281914jes. – ISSN 0013–4651

[84] Röder, Fridolin ; Braatz, Richard D. ; Krewer, Ulrike: Multi-Scale

Modeling of Solid Electrolyte Interface Formation in Lithium-Ion Batteries. Version: jan 2016. `http://dx.doi.org/10.1016/B978-0-444-63428-3.50031-X`. In: *Computer Aided Chemical Engineering* Bd. 38. Elsevier, jan 2016. – DOI 10.1016/B978–0–444–63428–3.50031–X. – ISBN 9780444634283, S. 157–162

[85] Röder, Fridolin ; Braatz, Richard D. ; Krewer, Ulrike: Multi-scale simulation of heterogeneous surface film growth mechanisms in lithium-ion batteries. In: *Journal of the Electrochemical Society* 164 (2017), Nr. 11, S. E3335–E3344. `http://dx.doi.org/10.1149/2.0241711jes`. – DOI 10.1149/2.0241711jes. – ISSN 19457111

[86] Saito, H. ; Masumoto, Y. ; Mizuno, T. ; Miura, A. ; Hashimoto, M. ; Ogawa, H. ; Tachikawa, S. ; Oshima, T. ; Choki, A. ; Fukuda, H. ; Hirahara, M. ; Okano, S.: Index: Piggy-back satelite for aurora observation and technology demonstration. In: *Acta Astronautica* 48 (2001), Nr. 5-12, S. 723–735. `http://dx.doi.org/10.1016/S0094-5765(01)00079-0`. – DOI 10.1016/S0094–5765(01)00079–0. – ISSN 00945765

[87] Saito, Hirobumi ; Hirahara, Masafumi ; Mizuno, Takahide ; Fukuda, Seisuke ; Fukushima, Yousuke ; Asamura, Kazushi ; Nagamatsu, Hiroyuki ; Tanaka, Koji ; Sone, Yoshitsugu ; Okuizumi, Nobukatsu ; Mita, Makoto ; Uno, Masatoshi ; Yanagawa, Yoshimitsu ; Takahara, Takuya ; Kaneda, Ryosuke ; Honma, Takashi ; Sakanoi, Takeshi ; Miura, Akira ; Ikenaga, Toshinori ; Ogawa, Keita ; Masumoto, Yasunari: Small satellite REIMEI for auroral observations. In: *Acta Astronautica* 69 (2011), Nr. 7-8, S. 499–513. `http://dx.doi.org/10.1016/j.actaastro.2011.05.007`. – DOI 10.1016/j.actaastro.2011.05.007. – ISSN 00945765

[88] Schmalstieg, Johannes ; Käbitz, Stefan ; Ecker, Madeleine ; Sauer, Dirk U.: A holistic aging model for Li(NiMnCo)O2 based 18650 lithium-ion batteries. In: *Journal of Power Sources* 257 (2014), S. 325–334. `http://dx.doi.org/10.1016/j.jpowsour.2014.02.012`. – DOI 10.1016/j.jpowsour.2014.02.012. – ISSN 03787753

[89] Schmitt, Tobias: *Degradation Models and Simulation Tools for Lithium and Zinc Batteries (PhD thesis)*, Universität Ulm, Diss., 2020. `10.18725/OPARU-29529`

[90] Severson, Kristen A. ; Attia, Peter M. ; Jin, Norman ; Perkins, Nicholas ; Jiang, Benben ; Yang, Zi ; Chen, Michael H. ; Aykol, Muratahan ; Herring, Patrick K. ; Fraggedakis, Dimitrios ; Bazant, Mar-

tin Z. ; Harris, Stephen J. ; Chueh, William C. ; Braatz, Richard D.: Data-driven prediction of battery cycle life before capacity degradation. In: *Nature Energy* 4 (2019), Nr. 5, S. 383–391. `http://dx.doi.org/10.1038/s41560-019-0356-8`. – DOI 10.1038/s41560–019–0356–8. – ISBN 4156001903

[91] Shi, Siqi ; Lu, Peng ; Liu, Zhongyi ; Qi, Yue ; Hector, Louis G. ; Li, Hong ; Harris, Stephen J.: Direct calculation of Li-ion transport in the solid electrolyte interphase. In: *Journal of the American Chemical Society* 134 (2012), Nr. 37, S. 15476–15487. `http://dx.doi.org/10.1021/ja305366r`. – DOI 10.1021/ja305366r. – ISSN 00027863

[92] Shrivakshan, G T. ; Chandrasekar, C: A Comparison of various Edge Detection Techniques used in Image Processing. In: *International Journal of Computer Science Issues (IJCSI)* 9 (2012), Nr. 5, S. 269–276. – ISSN 1694–0814; 1694–0784

[93] Simon, Dan: *Optimal state estimation: Kalman, H infinity, and nonlinear approaches*. John Wiley & Sons, 2006

[94] Single, Fabian ; Latz, Arnulf ; Horstmann, Birger: Identifying the Mechanism of Continued Growth of the Solid-Electrolyte Interphase. In: *ChemSusChem* 11 (2018), Nr. 12, S. 1950–1955. `http://dx.doi.org/10.1002/cssc.201800077`. – DOI 10.1002/cssc.201800077. – ISSN 1864564X

[95] Smiley, Adam ; Plett, Gregory L.: An adaptive physics-based reduced-order model of an aged lithium-ion cell, selected using an interacting multiple-model Kalman filter. In: *Journal of Energy Storage* 19 (2018), oct, S. 120–134. `http://dx.doi.org/10.1016/J.EST.2018.07.004`. – DOI 10.1016/J.EST.2018.07.004. – ISSN 2352–152X

[96] Sone, Yoshitsugu ; Ogawa, Keita ; Takeda, Yasuo ; Asamura, Kazushi ; Yamazaki, Atsushi ; Nagamatsu, Hiroyuki ; Fukushima, Yosuke ; Saito, Hirobumi: Charge and Discharge Performance of the Lithium-ion Secondary Battery in Space. In: *Tran. JSASS Aerospace Tech. Japan* 12 (2014), Nr. ists29, S. Pf_27–Pf_32. `http://dx.doi.org/10.2322/tastj.12.Pf_27`. – DOI 10.2322/tastj.12.Pf_27. – ISSN 1884–0485

[97] Sone, Yoshitsugu ; Watanabe, H. ; Tanaka, K. ; Mendoza-Hernandez, Omar S. ; Fukuda, S. ; Itagaki, M. ; Ogawa, K. ; Asamura, K. ; Yamazaki, A. ; Nagamatsu, H. ; Fukushima, Y. ; Saito, H.: Internal Impedance of the Lithium-Ion Secondary Cells Used for

Reimei Satellite after the Eleven Years Operation in Space. In: *E3S Web of Conferences* Bd. 16. Polanica-Zdrój, Poland : EDP Sciences, 2017. – ISSN 22671242, 07005

[98] SONE, Yoshitsugu ; WATANABE, Hiromi ; TANAKA, Kohei ; FUKUDA, Seisuke ; OGAWA, Keita ; ASAMURA, Kazushi ; YAMAZAKI, Atsushi ; NAGAMATSU, Hiroyuki ; FUKUSHIMA, Yosuke ; SAITO, Hirofumi: Long Term Operability of Li-ion Battery under Micro-gravity Condition Demonstrated by the Satellite "REIMEI". In: *Electrochemistry* 84 (2016), Nr. 1, S. 12–16. `http://dx.doi.org/10.5796/electrochemistry.84.12`. – DOI 10.5796/electrochemistry.84.12

[99] SONG, Yuchen ; LIU, Datong ; HOU, Yandong ; YU, Jinxiang ; PENG, Yu: Satellite lithium-ion battery remaining useful life estimation with an iterative updated RVM fused with the KF algorithm. In: *Chinese Journal of Aeronautics* 31 (2018), Nr. 1, S. 31–40. `http://dx.doi.org/10.1016/j.cja.2017.11.010`. – DOI 10.1016/j.cja.2017.11.010. – ISSN 10009361

[100] SOTO, Fernando A. ; MA, Yuguang ; MARTINEZ DE LA HOZ, Julibeth M. ; SEMINARIO, Jorge M. ; BALBUENA, Perla B.: Formation and Growth Mechanisms of Solid-Electrolyte Interphase Layers in Rechargeable Batteries. In: *Chemistry of Materials* 27 (2015), Nr. 23, S. 7990–8000. `http://dx.doi.org/10.1021/acs.chemmater.5b03358`. – DOI 10.1021/acs.chemmater.5b03358. – ISSN 15205002

[101] STETZEL, Kirk D. ; ALDRICH, Lukas L. ; TRIMBOLI, M. S. ; PLETT, Gregory L.: Electrochemical state and internal variables estimation using a reduced-order physics-based model of a lithium-ion cell and an extended Kalman filter. In: *Journal of Power Sources* 278 (2015), Nr. 2015, S. 490–505. `http://dx.doi.org/10.1016/j.jpowsour.2014.11.135`. – DOI 10.1016/j.jpowsour.2014.11.135. – ISBN 9781510811461

[102] STURM, J ; ENNIFAR, H ; ERHARD, S.V. ; RHEINFELD, A ; KOSCH, S ; JOSSEN, Andreas: State estimation of lithium-ion cells using a physicochemical model based extended Kalman filter. In: *Applied Energy* 223 (2018), Nr. April, S. 103–123. `http://dx.doi.org/10.1016/j.apenergy.2018.04.011`. – DOI 10.1016/j.apenergy.2018.04.011. – ISSN 03062619

[103] SULZER, Valentin ; MOHTAT, Peyman ; AITIO, Antti ; LEE, Suhak ; YEH, Yen T. ; STEINBACHER, Frank ; KHAN, Muhammad U. ; LEE, Jang W. ; SIEGEL, Jason B. ; STEFANOPOULOU, Anna G. ; HOWEY, David A.: The challenge and opportunity of battery lifetime prediction from field data.

In: *Joule* 5 (2021), Nr. 8, S. 1934–1955. `http://dx.doi.org/10.1016/j.joule.2021.06.005`. – DOI 10.1016/j.joule.2021.06.005. – ISSN 25424351

[104] Tahmasbi, A. A. ; Kadyk, T. ; Eikerling, M. H.: Statistical Physics-Based Model of Solid Electrolyte Interphase Growth in Lithium Ion Batteries. In: *Journal of The Electrochemical Society* 164 (2017), Nr. 6, S. A1307–A1313. `http://dx.doi.org/10.1149/2.1581706jes`. – DOI 10.1149/2.1581706jes. – ISBN 0013–4651

[105] Uno, Masatoshi ; Ogawa, Keita ; Takeda, Yasuo ; Sone, Yoshitsugu ; Tanaka, Koji ; Mita, Makoto ; Saito, Hirobumi: Development and on-orbit operation of lithium-ion pouch battery for small scientific satellite "REIMEI". In: *Journal of Power Sources* 196 (2011), Nr. 20, S. 8755–8763. `http://dx.doi.org/10.1016/j.jpowsour.2011.06.051`. – DOI 10.1016/j.jpowsour.2011.06.051. – ISBN 03787753

[106] Walker, Eric ; Rayman, Sean ; White, Ralph E.: Comparison of a particle filter and other state estimation methods for prognostics of lithium-ion batteries. In: *Journal of Power Sources* 287 (2015), S. 1–12. `http://dx.doi.org/10.1016/j.jpowsour.2015.04.020`. – DOI 10.1016/j.jpowsour.2015.04.020. – ISSN 03787753

[107] Wang, Aiping ; Kadam, Sanket ; Li, Hong ; Shi, Siqi ; Qi, Yue: Review on modeling of the anode solid electrolyte interphase (SEI) for lithium-ion batteries. In: *npj Computational Materials* 4 (2018), Nr. 1, S. 1–26. `http://dx.doi.org/10.1038/s41524-018-0064-0`. – DOI 10.1038/s41524–018–0064–0. – ISSN 20573960

[108] Wang, Xianming ; Yamada, Chisa ; Naito, Hitoshi ; Kuwajima, Saburo: Simulated low-earth-orbit cycle-life testing of commercial laminated lithium-ion cells in a vacuum. In: *Journal of Power Sources* 140 (2005), Nr. 1, S. 129–138. `http://dx.doi.org/10.1016/j.jpowsour.2004.08.021`. – DOI 10.1016/j.jpowsour.2004.08.021. – ISSN 03787753

[109] Wang, Yilun ; Shoemaker, Christine A.: A General Stochastic Algorithmic Framework for Minimizing Expensive Black Box Objective Functions Based on Surrogate Models and Sensitivity Analysis. In: *arXiv preprint arXiv:1410.6271* (2014)

[110] Wassiliadis, Nikolaos ; Adermann, Jörn ; Frericks, Alexander ; Pak, Mikhail ; Reiter, Christoph ; Lohmann, Boris ; Lienkamp, Markus: Revisiting the dual extended Kalman filter for battery state-of-charge and

state-of-health estimation: A use-case life cycle analysis. In: *Journal of Energy Storage* 19 (2018), Nr. March, S. 73–87. `http://dx.doi.org/10.1016/j.est.2018.07.006`. – DOI 10.1016/j.est.2018.07.006. – ISSN 2352152X

[111] Wei, Zhongbao ; Zhao, Jiyun ; Ji, Dongxu ; Tseng, King J.: A multi-timescale estimator for battery state of charge and capacity dual estimation based on an online identified model. In: *Applied Energy* 204 (2017), S. 1264–1274. `http://dx.doi.org/10.1016/j.apenergy.2017.02.016`. – DOI 10.1016/j.apenergy.2017.02.016. – ISSN 03062619

[112] Zhang, Dengfeng ; Li, Weichen ; Han, Xiaodong ; Lu, Baochun ; Zhang, Quanling ; Bo, Cuimei: Evolving Elman neural networks based state-of-health estimation for satellite lithium-ion batteries. In: *Journal of Energy Storage* 59 (2023), Nr. November 2022, S. 106571. `http://dx.doi.org/10.1016/j.est.2022.106571`. – DOI 10.1016/j.est.2022.106571. – ISBN 1342646193

[113] Zhang, Yunwei ; Tang, Qiaochu ; Zhang, Yao ; Wang, Jiabin ; Stimming, Ulrich ; Lee, Alpha A.: Identifying degradation patterns of lithium ion batteries from impedance spectroscopy using machine learning. In: *Nature Communications* 11 (2020), Nr. 1, S. 6–11. `http://dx.doi.org/10.1038/s41467-020-15235-7`. – DOI 10.1038/s41467–020–15235–7. – ISBN 4146702015235

[114] Zou, Changfu ; Manzie, Chris ; Nešić, Dragan ; Kallapur, Abhijit G.: Multi-time-scale observer design for state-of-charge and state-of-health of a lithium-ion battery. In: *Journal of Power Sources* 335 (2016), S. 121–130. `http://dx.doi.org/10.1016/j.jpowsour.2016.10.040`. – DOI 10.1016/j.jpowsour.2016.10.040. – ISSN 03787753

[115] Zou, Yuan ; Hu, Xiaosong ; Ma, Hongmin ; Li, Shengbo E.: Combined State of Charge and State of Health estimation over lithium-ion battery cell cycle lifespan for electric vehicles. In: *Journal of Power Sources* 273 (2015), S. 793–803. `http://dx.doi.org/10.1016/j.jpowsour.2014.09.146`. – DOI 10.1016/j.jpowsour.2014.09.146. – ISBN 0378–7753

Teile dieser Dissertation wurden bereits in folgendem Fachartikel veröffentlicht:

Bolay, Linda J.; Schmitt, Tobias; Hein, Simon; Mendoza-Hernandez, Omar S.; Hosono, Eiji; Asakura, Daisuke; Kinoshita, Koichi; Matsuda, Hirofumi; Umeda, Minoru; Sone, Yoshitsugu; Latz, Arnulf; Horstmann, Birger: *Microstructure-Resolved Degradation Simulation of Lithium-Ion Batteries in Space Applications.* In: Journal of Power Sources Advances 14 (2022), S. 100083.

Name: Linda Juliane Bolay

Erklärung

Ich erkläre, dass ich die Arbeit selbständig verfasst und keine anderen als die angegebenen Quellen und Hilfsmittel verwendet habe.

Ulm, den ....

Linda Juliane Bolay